Characterization and minimization of the half-integer stop band with space charge in hadron synchrotrons

Charakterisierung und Minimierung der quadrupolaren Resonanz bei halbzahligen Arbeitspunkten mit Raumladung in Hadronensynchrotrons
Zur Erlangung des Grades eines Doktors der Naturwissenschaften (Dr. rer. nat.) genehmigte Dissertation von Dmitrii Rabusov aus Blagoweschtschensk
Tag der Einreichung: 19.09.2022, Tag der Prüfung: 5.12.2022
Darmstadt — D 17

1. Gutachten: Prof. Dr. rer. nat. Oliver Boine-Frankenheim
2. Gutachten: Prof. Dr. Shaukat Khan

TECHNISCHE UNIVERSITÄT DARMSTADT

Fachbereich Elektrotechnik
und Informationstechnik
Institut für Teilchenbeschleunigung
und Elektromagnetische Felder

Characterization and minimization of the half-integer stop band with space charge in hadron synchrotrons
Charakterisierung und Minimierung der quadrupolaren Resonanz bei halbzahligen Arbeitspunkten mit Raumladung in Hadronensynchrotrons

Genehmigte Dissertation von Dmitrii Rabusov aus Blagoweschtschensk

1. Gutachten: Prof. Dr. rer. nat. Oliver Boine-Frankenheim
2. Gutachten: Prof. Dr. Shaukat Khan

Tag der Einreichung: 19.09.2022
Tag der Prüfung: 5.12.2022

Darmstadt — D 17

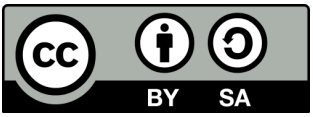

Erklärung zur Dissertation gemäß der Promotionsordnung der TU Darmstadt

§ 8 Abs. 1 lit. c PromO
Ich versichere hiermit, dass die elektronische Version meiner Dissertation mit der schriftlichen Version übereinstimmt.

§ 8 Abs. 1 lit. d PromO
Ich versichere hiermit, dass zu einem vorherigen Zeitpunkt noch keine Promotion versucht wurde.

§ 9 Abs. 1 PromO
Ich versichere hiermit, dass die vorliegende Dissertation selbstständig und nur unter Verwendung der angegebenen Quellen verfasst wurde.

§ 9 Abs. 2 PromO
Die Arbeit hat bisher noch nicht zu Prüfungszwecken gedient.

Darmstadt, den 1.09.2022

(Dmitrii Rabusov)

Abstract

This work characterizes the half-integer stop band for various beam distributions in hadron synchrotrons using simulation models with self-consistent space charge and experimental data. Synchrotrons for hadron beams are an important tool in fundamental research (particle and nuclear physics) and applied sciences (medical technology, materials science, industry). However, they are subject to undesirable effects, which degrade the quality of the beam. In any hadron synchrotron, the half-integer resonance is among the strongest effects that limit the maximum achievable beam intensity. The heavy-ion superconducting synchrotron SIS100, currently under construction at GSI, together with the already operating SIS18 synchrotron at GSI, should provide intense beams for future FAIR experiments. Using SIS100 as an example, this work develops a quantitative framework for characterizing the half-integer stop band for realistic, Gaussian-like distributed bunched beams in simulations. The developed framework is tested in a dedicated experiment in SIS18. In any synchrotron, gradient errors in quadrupole magnets induce the half-integer resonance. Due to the half-integer resonance, the beam intensity is limited, which is often referred to as the space-charge limit. To minimize the half-integer stop band for a bunched beam, and hence increase the maximum achievable intensity, lattice corrections are applied. Including space charge in the optimization procedure yields results equivalent to a conventional lattice correction. We validate in long-term simulations, that conventional correction tools are sufficient for increasing the gradient-error-induced space-charge limit of synchrotrons. This study identifies the tune areas affected by the half-integer resonance for varying space-charge strengths. The role of synchrotron motion in providing continuous emittance growth across the bunch is investigated. A key insight of this analysis is that, for bunched beams, a relatively small gradient error can result in a large half-integer stop-band width. The maximum achievable bunch intensity is thus reduced significantly. This contrasts with the findings in existing studies in literature based on more simplified beam distributions, where the space-charge limit does not depend on the strength of gradient errors. The reason for the discrepancy is identified in the increasing stop-band width for Gaussian distributions when space charge becomes stronger, which appears on time scales relevant for synchrotrons.

Zusammenfassung

In dieser Arbeit wird die transversale quadrupolare Resonanz bei halbzahligen Arbeitspunkten für verschiedene Strahlverteilungen in Hadron-Synchrotrons anhand von Simulationsmodellen mit selbstkonsistenter Raumladung und experimentellen Daten charakterisiert. Synchrotrone spielen in der Forschung (Teilchenphysik, Kernphysik) und den Anwendungen (Medizintechnik, Materialwissenschaft, Industrie) eine wichtige Rolle. Bei ihrem Betrieb treten jedoch unerwünschte Effekte auf, welche die Strahlqualität beeinträchtigen. Die quadrupolare Resonanz gehört zu den stärksten (kollektiven) Effekten, welche die maximal erreichbare Strahlintensität in Hadronensynchrotrons begrenzen. Das aus supraleitenden Magneten bestehende Schwerionensynchrotron SIS100, das derzeit an der GSI entsteht, soll zusammen mit dem bereits an der GSI in Betrieb befindlichen Synchrotron SIS18 intensive Ionenstrahlen für zukünftige FAIR Experimente bereitstellen. In dieser Arbeit wird am Beispiel des SIS100 ein Modell zur quantitativen Charakterisierung des quadrupolaren Stoppbandes für realistische Ionenbunche entwickelt. Das entwickelte Modell wurde in einem dedizierten Experiment im SIS18 getestet. Um das halbzahlige Stoppband für einen gebunchten Strahl zu minimieren und somit die maximal erreichbare Intensität zu erhöhen, werden Korrekturmagnete verwendet. Das in dieser Arbeit entwickelte Optimierungsverfahren bezieht die Raumladung ein für die Bestimmung der Stärken der Korrekturmagnete. Die Ergebnisse weichen nicht wesentlich von denen konventioneller Tools ab. Aus dieser Erkenntnis folgt, dass konventionelle Korrekturverfahren ausreichen, um die durch Gradientenfehler verursachte Raumladungsgrenze in Synchrotronen zu erhöhen. In dieser Arbeit werden Tunebereiche für Raumladungsfelder verschiedener Stärken identifiziert, die von der durch Gradientenfehler angeregten quadrupolare Resonanz betroffen sind. Die Rolle der Synchrotronbewegung bei dem beobachteten kontinuierlichen Anstieg der Emittanz über den Bunch hinweg wird untersucht. Eine wichtige Erkenntnis dieser Analyse ist, dass ein relativ kleiner Gradientenfehler zu einer großen Breite des quadrupolaren Stoppbandes führen kann. Die maximal erreichbare Strahlintensität, oft als Raumladungsgrenze bezeichnet, wird dadurch erheblich reduziert. Dies steht im Gegensatz zu den Ergebnissen vorheriger Studien in der Literatur, in denen vereinfachte Strahlverteilungen verwendet wurden. Als Grund für diese Diskrepanz wurde die für stärker werdende Raumladung zunehmende Stoppbandbreite identifiziert, wie sie auf für Synchrotrone relevanten Zeitskalen auftritt.

Contents

1 Introduction

Charged particles guided by electromagnetic fields play a significant role in various phenomena in nature. In science, charged particles are utilized in many experiments aimed at improving our understanding of the universe. Some experiments require specific conditions, like the energy or species of charged particles. For example, there is a demand for high energies to explore a subatomic structure, since the resolution increases with the energy. For such applications, a particle accelerator is a principal option. Particularly, a synchrotron [1–3], which is a type of circular accelerator, serves as a reliable source of charged particles with the desired energy and the number of particles (intensity). A number discoveries awarded by Nobel Prize, for example, Refs. [4–8], would not have been possible without synchrotrons. Currently, the most well-known synchrotron is the Large Hadron Collider (LHC) [9] at the European Organization for Nuclear Research (CERN) for the discovery of the Higgs boson [10, 11]. However, synchrotrons are used not only for fundamental research, but also in industry applications [12] related to material science, nuclear medicine, and catalysis. This work elaborates the cases of SIS18 [13, 14] and SIS100 [15] synchrotrons at FAIR which are intended to investigate various fundamental and applied research programs, for example, the nature of matter and antimatter using ion collisions.

1.1 Synchrotrons

As illustrated in Fig. 1.1, a synchrotron consists of several components that serve specific purposes. First, particles in a synchrotron (accumulated in beams) are guided by the magnetic field of dipole magnets in a fixed closed-loop path which is referred to as a closed orbit. The guide field B_0 together with the synchrotron radius R determines the energy of each particle. An example of a pair of dipole magnets is shown in Fig. 1.2 (red-colored, located in the middle). Next, quadrupole magnets (yellow magnets on the left and on the right side of the picture) confine particles in the transverse plane (perpendicular to the direction of motion) due to the so-called “strong-focusing”.

The concept of strong focusing was patented by Christofilos [17]. Then, it was analytically described by Blewett [18], and independently by Courant, Livingston, and Snyder [19]. The first synchrotron with strong focusing, Proton Synchrotron

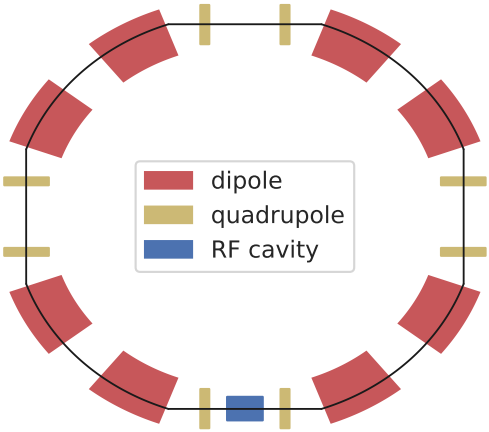

Figure 1.1: A sketch of a synchrotron. Dipole magnets (red) guide particles, quadrupole magnets (yellow) maintain the transverse focusing, RF cavities (blue) accelerate particles.

Figure 1.2: Magnets of the SIS18 synchrotron, dipole (red color, middle) and quadrupole (yellow color) magnets. The picture is adapted from [16].

(PS) [20, 21], was built in 1959 at CERN. A year later, the Alternating Gradient Synchrotron (AGS) [22] was built and then commissioned at Brookhaven National Laboratory (BNL).

The main principle of strong focusing resembles a problem in linear optics. The quadrupole magnets are powered in such a way that each of them acts like either a focusing (F) or a defocusing (D) lens. Figure 1.3 illustrates this concept on a pair of quadrupole magnets grouped in a so-called FODO cell or a quadrupole doublet. First, a diverging beam passes through a focusing magnet (blue color) which performs a kick proportionally to particle offset. Therefore, the trajectories in the beam converge. Next, a defocusing magnet (red color) pushes the particles in the opposite direction. If this cell is repeated, particles oscillate around the equilibrium ($x = 0$ in this example), and as a result, the beam is confined throughout the passage.

In synchrotrons, the transverse focusing is mainly performed using quadrupole magnets in different arrangements, for example, doublets or triplets located between bending dipole magnets. The number of oscillations per one turn is the betatron tune $Q_{x,y}$, horizontal and vertical correspondingly.

Radio Frequency (RF) cavities are used in a synchrotron to accelerate the particles. Additionally, RF cavities modify the longitudinal beam profile by performing

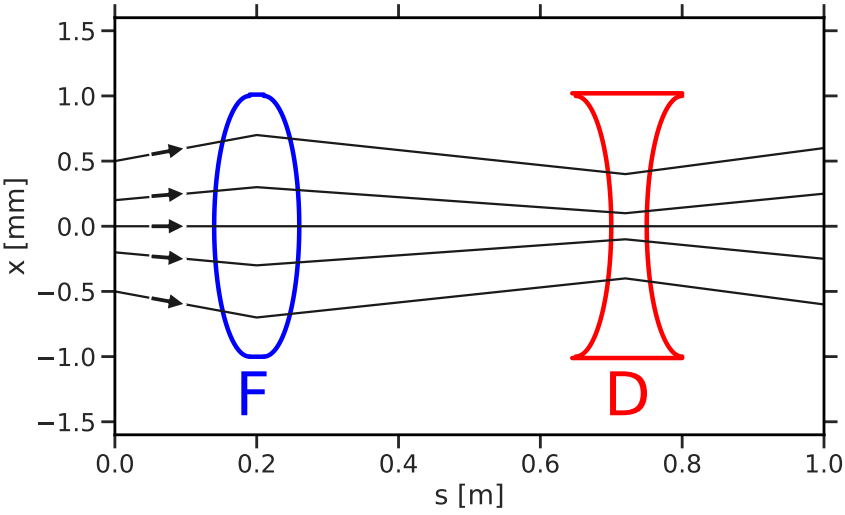

Figure 1.3: Passage of particles through a FODO cell, which consists of a focusing quadrupole (blue, F) and a defocusing quadrupole (red, D).

bunching (bunched beams) and cause longitudinal oscillations of particles. Continuous beams (without RF) are referred to as coasting.

Since charged particles travel in a synchrotron by tortuous cyclic trajectories, they emit radiation. The amount of this radiation rapidly scales with γ_r, the ratio of the total particle energy to the rest mass (in electronvolts). Therefore, this effect is extremely relevant for the design of machines operating with light particles like electrons but negligible for the majority of hadron machines. As a result, all synchrotrons are classified as either lepton or hadron machines.

A vital component for experiments is that the required amount of statistical data (for example, a number of collisions) can be collected during a reasonable time period. In general, this refers to the requirements for beam intensity and beam emittances[1]. Although synchrotrons are reliable machines, there are undesired effects causing beam quality degradation. Such effects incorporate, for example, betatron resonances [23–25] (particles are forbidden to oscillate on certain frequencies), beam instabilities [26–28] (exponential growth of beam moments), space charge [29, 30] (particles with the same charge repel), and vacuum deterioration [31] (scattering on the residual gas). As a result, the lifetime of the beam can rapidly decrease. In order to improve the performance of a synchrotron, the effects listed above should be studied and avoided. For example, betatron resonances and space-charge effects are expected to be significant in the SIS100 hadron synchrotron [32] at the Facility for Antiproton and Ion Research (FAIR) [33], which is currently under construction at the GSI Helmholtz Center for Heavy Ion Research.

1.2 FAIR and GSI

GSI (Darmstadt, Germany) is an accelerator facility for fundamental and applied research purposes. Fundamental research at GSI includes nuclear and particle physics, such as the synthesis of new heavy elements of the periodic system and the elements with extreme numbers of protons and neutrons. Furthermore, nuclear research incorporates studies of the so-called quark-gluon plasma. All described above help scientists to explore insights on our universe, star explosions, and the origin of chemical elements in stars. Applied research is represented at GSI by atomic physics, plasma physics, biophysics, medical science, and materials research. Such activities include the study of the atomic shell of heavy ions, the creation of hot and dense plasma, tumor therapy, dosimetry, and irradiation of cells and materials.

The FAIR complex is designed to investigate the structure of matter and antimatter, as well as the evolution of the universe. The four pillars of the FAIR scientific

[1] Emittance is the volume in phase space occupied by a particle beam.

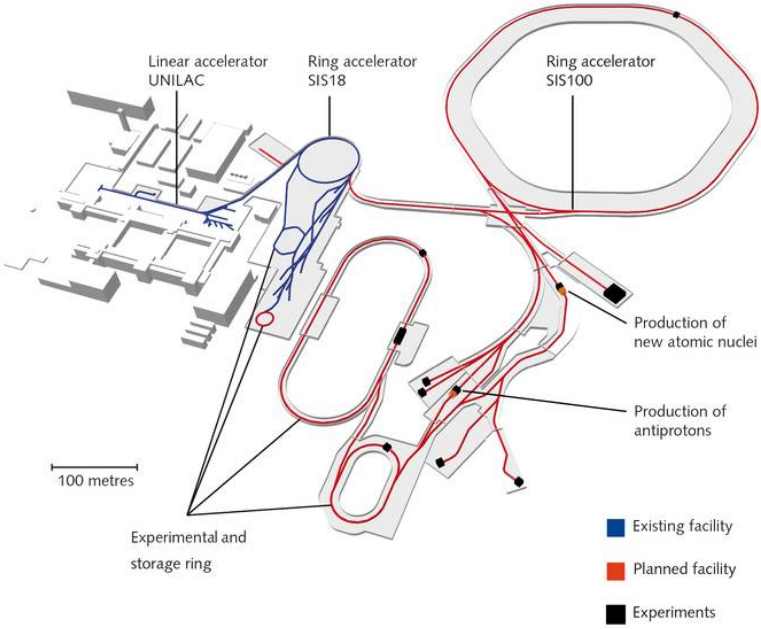

Figure 1.4: Schematic layout of the existing GSI (blue) and the planned FAIR complex (red) [34].

program are Nuclear Structure Astrophysics and Reactions (NUSTAR) [35], Compressed Baryonic Matter (CBM) [36, 37], Anti-Proton ANnihilation at DArmstadt (PANDA) [38], and Atomic, Plasma Physics and Application (APPA) [39, 40].

Figure 1.4 shows the design of how the particles are produced, accelerated, and transported toward the experimental area. First, the UNIversal Linear Accelerator [41, 42] (UNILAC, the leftmost blue straight line) creates an ion beam with the required charge-to-mass ratio (the ion type spans from protons to uranium). Next, the beam is transferred to SIS18 [13, 14] (the blue ring on top) where it is accumulated and accelerated. SIS18 is a synchrotron with a circumference of 216.72 m and the maximum field of dipole magnets 1.8 T. To reach the required energies at FAIR experiments [43], the ion beam is accelerated further in SIS100 [15] which is the major booster ring of the FAIR complex with a circumference of 1083.6 m.

1.3 Motivation and goals for this work

As mentioned above, quadrupole magnets cause transverse oscillations of particles. Imperfections in the magnets of a synchrotron drive betatron resonances. Particle oscillations at certain resonant frequencies, therefore, have higher amplitudes over time. The vicinity of resonant frequencies should be identified and avoided during the operation of a synchrotron because betatron resonances result in beam quality degradation, such as an emittance growth of a beam and consequent particle losses. The vicinity of frequencies affected by the resonance is called the stop-band width. With increasing resonance order, betatron resonances become weaker.

At the intensities required by the FAIR operation, the space-charge force plays a significant role in beam dynamics in the SIS100 synchrotron [32]. Due to space charge, particles can cross different resonances and consequently contribute to emittance growth. However, effects such as space charge which appear from the beam itself are not the same as external forces, and they should be treated with a separate terminology to provide accurate predictions. For example, the dipolar resonance (Q in an integer number n) corresponds to the lowest possible order. If it appears, the beam offset (the center of charge) becomes unstable. However, the motion of the center of charge is not affected by direct space charge. The quadrupolar resonance, when $2Q = n$ (the half-integer resonance), on the contrary, depends on space charge because internal forces increase with decreasing transverse beam sizes and vice versa.

The lowest order (hence, the strongest) resonance affected by space charge is the half-integer (quadrupolar) resonance. Field errors in quadrupole magnets (gradient errors) are the major source of the half-integer resonance. The first analytical studies on the half-integer resonance were carried out by Courant and Snyder [44]. They performed the treatment based on single particle dynamics in the perturbed lattice by a gradient error. Though the stop-band width is defined using this approach, it is done excluding collective effects.

At the early stage of the design of high-intensity synchrotrons, space charge was realized to be a notable issue, addressing quadrupolar resonances [45]. It was demonstrated analytically in Refs. [46, 47] that space-charge effects cannot put the beam onto the integer resonance, whereas the beam width oscillates on a frequency shifted by space charge. Then, the phenomenon of the space-charge limit due to the half-integer resonance for round isotropic coasting beams [48] was investigated. Next, Sacherer [49, 50] derived envelope equations to study the half-integer resonance for any particle distribution of a coasting beam with ellipsoidal symmetry. The analytical works mentioned above are summarized in the overview Ref. [51].

Also, space-charge effects and their influence on betatron resonances were studied in experiments [52–56].

More recent works like Ref. [57–60] use computer simulations together with analytical models. For example, the latter one uses the transverse Gaussian electric field of a coasting beam for stop-band computations of the octupolar resonance. Also, several systematic investigations like Refs. [61, 62] of a beam core model have been undertaken. The latter one has specifically targeted the exact lattice structure and the effects caused by the energy spread of particles in a beam. The findings of Ref. [63] have confirmed in 2D particle-in-cell (PIC) simulations that the half-integer resonance occurs on the coherently shifted tune, and Ref. [64] elaborates on the envelope dynamics under space charge conditions and the stop-band correction.

A large and growing body of literature has investigated the case of space charge in 3D distributions since all synchrotrons operate with bunched beams. For example, bunched beams have been used [60] in simulations with the frozen space-charge model (particles interact only with the average electric field of a beam, not between each other), and also in 3D PIC tracking with slow synchrotron motion [63] but only for structure resonances (no gradient error included). Recently, it has been shown [65] how to numerically compute stop bands of the envelope instabilities for bunched beams. The interplay between the incoherent and coherent effects in bunched beams has been described [66] albeit with a focus on structure resonances (no gradient error included). We shall indicate here that a comprehensive study of the quadrupole resonance with nonlinear space charge for realistic, i.e. 3D Gaussian-like distributed bunched beams, is lacking. The general case is challenging to tackle with analytical models, and this work addresses this subject in self-consistent macro particle tracking simulations.

This study builds on SIS18 and SIS100 synchrotrons as relevant example cases of machines with gradient errors and $\gamma_r \gtrsim 1$ where space charge plays a significant role. Moreover, SIS100 features a gradient error by its design. The half-integer resonance is among the most important factors determining machine settings for high-intensity operation.

1.4 Overview of the dissertation

This dissertation is organized as follows. Chapter 2 introduces basic concepts of beam dynamics with a focus on the half-integer resonance at zero intensity. In Chapter 3, the most relevant analytical expressions for the quadrupolar resonance in combination with space charge are reviewed. The approach of the half-integer stop-band characterization in particle tracking simulations is shown in Chapter 4.

The main focus of the study is on simulations for bunched beams for varying space charge and gradient-error strength. Coasting beam simulations are used to relate to previous results in the literature. Next, Sec. 4.5 confirms that the findings of Sec. 4.4 hold for time scales as relevant for the synchrotron operation. Additionally, the influence of synchrotron tune on the total emittance growth inside the stop band is discussed. Then, Sec. 4.6 extrapolates the previous findings to predict the space-charge limit in presence of gradient errors. Next, Chapter. 5 introduces the lattice correction to minimize the stop-band width without space charge and proceeds to validate with 3D PIC space-charge simulations that the correction also applies to bunched beams with space charge over long time scales. Finally, Chapter 6 demonstrates the experimental results obtained in SIS18. The last chapter summarizes the major findings of this thesis.

2 Single-particle dynamics in a synchrotron with gradient errors

This chapter describes the basic concepts and terminology of beam dynamics which apply to a synchrotron operating at energy E with corresponding relativistic factors β_r and γ_r as a prerequisite for the following chapters. A detailed discussion of particle dynamics in accelerators can be found in textbooks like Refs. [25, 67–70].

In general, the motion of a particle with the charge $q = Z\,e$ and the velocity $\vec{v}$ is governed by the Lorentz force

$$\vec{F} = \frac{\mathrm{d}\vec{p}}{\mathrm{d}t} = q\left(\vec{E} + \vec{v} \times \vec{B}\right), \tag{2.1}$$

where e is the elementary charge. Then, in the constant magnetic field B_0, charged particles with the momentum p rotate with the radius R

$$Z\,e\,B_0\,R = p \tag{2.2}$$

where $\vec{p} \perp \vec{B}_0$. Therefore the momentum, or likewise the energy, per charge is equivalent to the magnetic rigidity $B_0 R$.

2.1 Transverse motion

This section describes the transverse trajectories of particles in a synchrotron under the influence of electromagnetic fields.

2.1.1 Equations of motion

Let us consider that the reference (design) orbit corresponding to the ideal particle trajectory in a synchrotron is a closed planar curve. A simplified example case of a circular reference orbit is shown in Fig. 2.1, whereas in the real machine it is made up of arcs and straight sections. Dipole sector magnets (placed in arcs) create a guide magnetic field B_0 which causes the bending of particle trajectories. The coordinate system $(x,\ y,\ z)$ follows the reference particle, where y and z are parallel

to the direction of the guide field and the direction of travel respectively. Therefore, the guide field is $(B_x, B_y, B_z) = (0, B_0, 0)$, and the spatial position of a test particle is represented by (x, y, z) horizontal, vertical, and longitudinal displacements in this coordinate system. The right side of the relativistic equation of motion in the horizontal plane,

$$\gamma_r\, m\, \frac{\mathrm{d}^2 x}{\mathrm{d}t^2} = \gamma_r\, m\, \frac{v_z^2}{R+x} - Z\, e\, B_y\, v_z\,, \tag{2.3}$$

corresponds to the centrifugal and Lorentz forces. It is convenient to use equations of trajectories instead of equations of motion. The path s along the reference orbit thus replaces the independent variable time t with the dependence $s = \beta_r\, c\, t$, where β_r is a ratio of the particle velocity to the speed of light c. As a result, the vector $(\mathrm{d}x/\mathrm{d}s,\, \mathrm{d}y/\mathrm{d}s,\, \Delta p/p)$ is used instead of the corresponding velocity vector $\frac{\mathrm{d}}{\mathrm{d}t}(x, y, z)$ to define the "mechanical state" of the system. Also, throughout the whole work the notations $x' = \mathrm{d}x/\mathrm{d}s$ and $y' = \mathrm{d}y/\mathrm{d}s$ are used, $\Delta p/p$ corresponds to the deviation of momentum. The transverse phase space is (x, x', y, y'), the longitudinal phase space is $(z, \Delta p/p)$. Taking $x/R \ll 1$ into account we can develop Eq. (2.3),

$$x'' = \frac{1}{R} - \frac{x}{R^2} - \frac{Z\, e}{p}\,(B_y + \frac{\partial B_y}{\partial x}\, x)\,, \tag{2.4}$$

to the first order. The last term arises due to the gradient of the magnetic field which can be introduced by quadrupole magnets. In synchrotrons, quadrupoles are located and powered in a specific way to perform so-called "strong focusing" or "alternating-gradient" [19]. As a result, the magnetic focusing forces confine the particles to the vicinity of their reference orbit which becomes the equilibrium orbit. Using the conditions $\nabla \times \vec{B} = 0$ (for quadrupole magnets) and Eq. (2.2), the equations of trajectories become

$$\begin{cases} x'' + k_x(s)\, x = 0 \\ y'' + k_y(s)\, y = 0\,, \end{cases} \tag{2.5}$$

corresponding to Hill's equations [44] in both horizontal and vertical planes, where the focusing functions are

$$\begin{cases} k_x(s) = \frac{1}{R^2} + \frac{Z\, e}{p}\, \frac{\partial B_y}{\partial x} \\ k_y(s) = -\frac{Z\, e}{p}\, \frac{\partial B_y}{\partial x}\,. \end{cases} \tag{2.6}$$

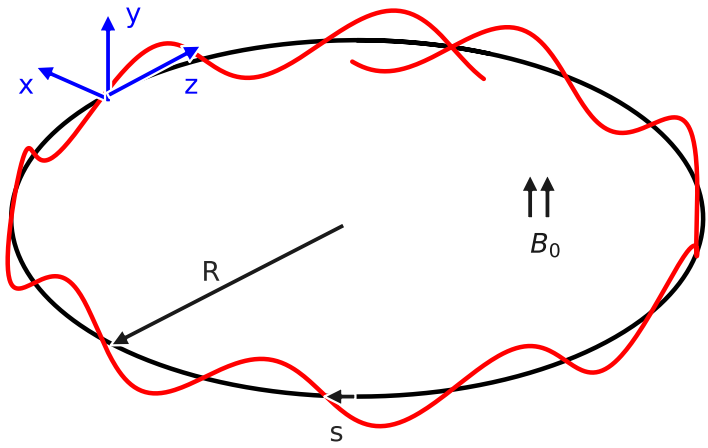

Figure 2.1: Coordinate system (x, y, z) for the horizontal, vertical, and longitudinal planes, respectively. The trajectory of a test particle (red) oscillates around the equilibrium orbit (black circle).

Note, that both focusing functions satisfy the condition $k_{x,y}(s) = k_{x,y}(s + C)$, namely, they are periodic over the circumference C. Equation (2.5) results in pseudo-harmonic oscillations,

$$\begin{cases} x(s) = \sqrt{2J_x\,\beta_x(s)}\cos(2\pi\,\mu_x(s) + \phi_{x,0}) \\ y(s) = \sqrt{2J_y\,\beta_y(s)}\cos(2\pi\,\mu_y(s) + \phi_{y,0}), \end{cases} \tag{2.7}$$

known as betatron motion, where $\beta_{x,y}(s)$ is the beta-function, $\mu_{x,y}(s)$ is the betatron phase advance. Arbitrary constants $J_{x,y}$ and ϕ_0 can be defined by the initial coordinates of a particle in the horizontal and vertical phase planes. In general, beta-functions and phase advances are different in horizontal and vertical planes.

The red solid line in Fig. 2.1 represents a trajectory corresponding to the betatron oscillations around the equilibrium orbit. The number of such oscillations per one turn is the betatron bare tune Q. This value together with the beta-function and the phase advance defines the design optics of a synchrotron. The pair of values (Q_x, Q_y) is also referred to as the working point of a synchrotron.

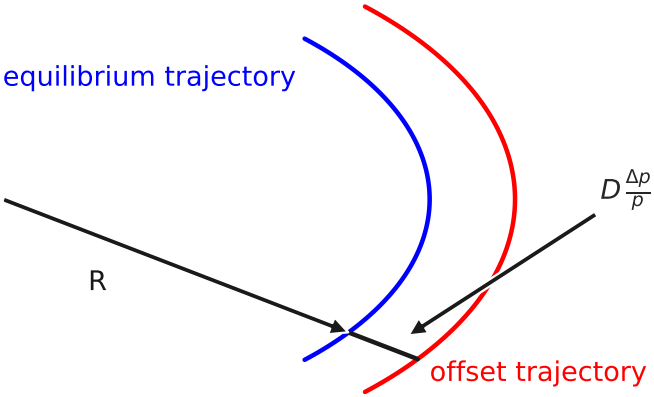

Figure 2.2: Equilibrium (blue) and offset (red) particle trajectories.

2.1.2 Off-momentum particles and dispersion

Let us consider an off-momentum particle with $\Delta p/p$.

As shown in Fig. 2.2, the trajectory of this particle deviates from the equilibrium one by the value $x_p = D(s)\,\frac{\Delta p}{p}$, where D(s) is the dispersion function which satisfies the condition

$$\frac{\mathrm{d}^2 D(s)}{\mathrm{d}s^2} + k_x(s)\,D(s) = \frac{1}{R}\,. \tag{2.8}$$

In the majority of synchrotrons, the guide field B_0 is strictly vertical, the equilibrium orbit stays constant in the (y, s) plane. As a result, the dispersion can deviate from zero only inside bending magnets in the horizontal plane. The total path length of the off-momentum particle

$$\frac{\Delta C}{C} = \frac{\Delta p/p}{C} \oint \frac{D(s)}{R}\,ds = \alpha_c\,\Delta p/p \tag{2.9}$$

differs from the circumference C of the equilibrium trajectory, where α_c is called the momentum compaction factor. Next, the slippage factor η

$$\frac{\Delta\omega}{\omega} = -\left(\alpha_c - \frac{1}{\gamma_r^2}\right)\Delta p/p = -\eta\,\Delta p/p \tag{2.10}$$

determines the shift of an angular revolution frequency ω. Additionally to the dispersion, the off-momentum particle has the deviation of bare tunes,

$$\frac{\Delta Q}{Q} = \xi \, \Delta p/p \,, \tag{2.11}$$

where ξ is the normalized chromaticity (see e.g. Ref. [67]) defined by

$$\xi = \frac{1}{4\pi Q} \oint \beta(s)\, k(s)\, ds \,, \tag{2.12}$$

it is different in horizontal and vertical planes.

2.1.3 One-turn matrix and stability

Let us consider only the vertical plane here for simplicity. The functions $\alpha(s)$, $\beta(s)$, $\gamma(s)$ are the *Twiss parameters* defines as

$$\begin{cases} \alpha = -\frac{1}{2}\frac{d\beta}{ds} \\ \beta = w^2 \\ \gamma = \frac{1+\alpha^2}{\beta} \,. \end{cases} \tag{2.13}$$

Using the normal solution of Eq. (2.5), $f(s) = w(s)\, e^{i\, 2\pi\, \mu(s)}$, we can obtain the nonlinear equation,

$$w(s)'' + k(s)\, w(s) - \frac{1}{w(s)^3} = 0 \,, \tag{2.14}$$

known as the envelope equation for a single particle.

The meaning of the Twiss parameters can be explained using the phase space of the betatron oscillation in Fig. 2.3.

The particle trajectory in vertical phase space at an arbitrary location in the synchrotron corresponds to the ellipse (shown in black) with area $\pi\, 2J$

$$\gamma\, y^2 + 2\,\alpha\, y\, y' + \beta\, y'^2 = 2J \,, \tag{2.15}$$

which is defined by the Courant-Snyder quadratic form. For a single particle, the quantity J is a canonical coordinate "action" which is at the same time the Courant-Snyder invariant. In the case of a beam distribution, the RMS value of $2J$ over the distribution corresponds to the RMS emittance ϵ. This quantity corresponds to the area in the phase space occupied by the beam.

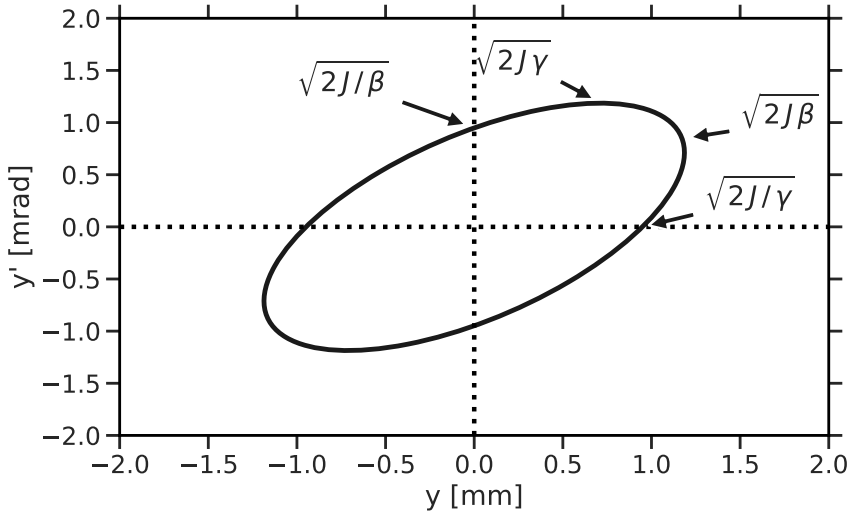

Figure 2.3: Phase-space trajectory of the betatron oscillation.

The coordinates of a particle in the vertical phase space after one turn can be obtained using

$$\begin{pmatrix} y \\ y' \end{pmatrix} = M \cdot \begin{pmatrix} y \\ y' \end{pmatrix}_0 , \tag{2.16}$$

where M is the one-turn matrix. It is parameterized via Twiss functions as

$$M = I \cos 2\pi\mu + S \sin 2\pi\mu , \tag{2.17}$$

where I is the identity matrix, and the zero-trace matrix S is defined by

$$S = \begin{pmatrix} \alpha & \beta \\ -\gamma & -\alpha \end{pmatrix} . \tag{2.18}$$

Therefore, the one-turn matrix is parameterized as

$$M = \begin{pmatrix} \cos 2\pi\mu + \alpha \sin 2\pi\mu & \beta \sin 2\pi\mu \\ -\gamma \sin 2\pi\mu & \cos 2\pi\mu - \alpha \sin 2\pi\mu \end{pmatrix} . \tag{2.19}$$

The characteristic equation

$$\det(M - \lambda I) = 0 \tag{2.20}$$

serves to find the eigenvalues λ,

$$\lambda_{1,2} = \frac{1}{2}\,\mathrm{Tr}[M] \pm i\sqrt{1-\left(\frac{1}{2}\,\mathrm{Tr}[M]\right)^2}\,, \tag{2.21}$$

where i is the imaginary unit, $\mathrm{Tr}[M]$ is the trace of the matrix M. Consequently,

$$\lambda_{1,2} = \cos 2\pi\mu \pm i\,\sin 2\pi\mu \tag{2.22}$$

sets the stability condition $|\lambda| = 1$ on elements of the matrix M, namely,

$$-2 \le \mathrm{Tr}[M] \le 2\,. \tag{2.23}$$

If $\lambda > 1$, the system becomes unstable. To compute lattice functions and parameters numerically, the one-turn matrix can be obtained via

$$M = T(s_0|s_1)\cdot T(s_1|s_2)\cdot \ldots \cdot T(s_N|s_0) \tag{2.24}$$

multiplication of transport matrices of each of N elements in the lattice. For example, a simple drift from s_0 to s_1 is

$$T(s_0|s_1) = \begin{pmatrix} 1 & s_1 - s_0 \\ 0 & 1 \end{pmatrix}, \tag{2.25}$$

whereas a quadrupole corresponds to

$$T(s_1|s_2) = \begin{pmatrix} 1 & (s_2-s_1)/2 \\ 0 & 1 \end{pmatrix} \cdot \begin{pmatrix} 1 & 0 \\ k\,(s_2-s_1) & 1 \end{pmatrix} \cdot \begin{pmatrix} 1 & (s_2-s_1)/2 \\ 0 & 1 \end{pmatrix}, \tag{2.26}$$

where k is the gradient of the magnetic field in the quadrupole magnet.

2.2 Longitudinal motion

So far this work has focused on the dynamics in the transverse plane. The following section discusses the longitudinal motion.

A single radiofrequency (RF) cavity creates the electric voltage

$$V_{\mathrm{RF}}(t) = V\,\sin(\phi + \phi_s) \tag{2.27}$$

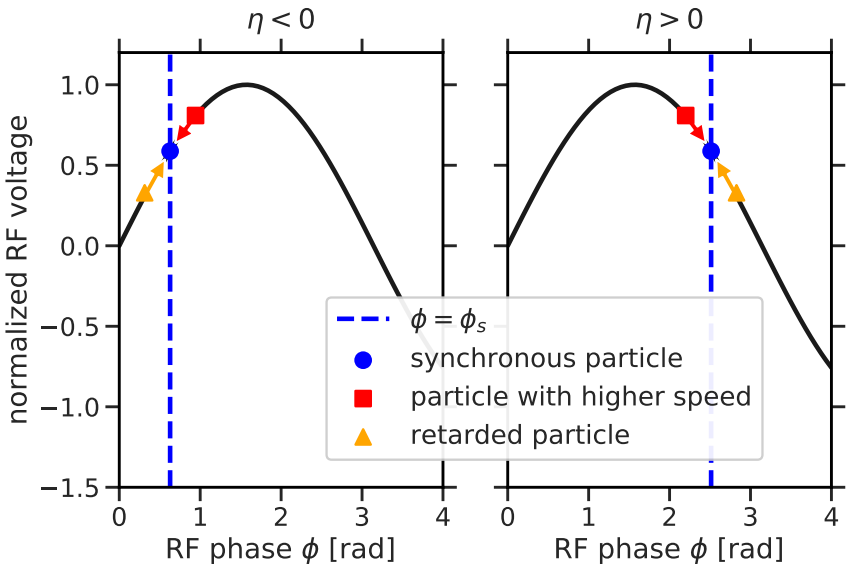

Figure 2.4: RF voltage applied on particles for negative (left) and positive (right) values of the slip factor. The blue dot is the synchronous particle, whereas red squares and orange triangles correspond to particles which are ahead or lagging behind the synchronous one.

for a particle at a phase ϕ where V is the amplitude of the RF voltage, and ϕ_s is a phase factor. Therefore, a synchronous particle ($\phi = \phi_s$) gains[1] or loses energy $q\,V\sin(\phi_s)$. Additionally, RF cavities provide focusing in the longitudinal plane which is shown in Fig. 2.4.

The basic idea of the longitudinal focusing is that the particles, which are ahead of the synchronous one (red squares), gain less energy each turn, whereas the particles, which are lagging behind (orange triangles), increase their energy faster. If $\eta < 0$ (on the left), red squares arrive to the RF cavity earlier each turn, thus, they receive less RF voltage. At the same point, orange triangles arrive later and gain more energy consequently. On the other hand, if $\eta > 0$ (on the right), particles with higher velocities arrive to the RF cavity later each turn, when retarded particles can overtake the synchronous one.

[1] Ramping (energy boost) is performed *synchronously* with the increase of the guide field B_0.

The RF frequency ω_{RF} is equal to the revolution frequency $\omega_0 = \frac{\beta_r c}{2\pi R}$ times the (integer) harmonic number h. The longitudinal offset z (introduced in Fig. 2.1) relates to the RF phase ϕ, $z = -R\phi/h$. With the external electric potential from the RF, the equations of motion (see e.g. Ref. [67]) are

$$\begin{cases} \frac{\mathrm{d}\phi}{\mathrm{d}t} = h\,\omega_0\,\eta\,\frac{\Delta p}{p} \\ \frac{\mathrm{d}(\Delta p/p)}{\mathrm{d}t} = \frac{1}{2\pi}\,\frac{\omega_0\,q\,V}{\beta_r^2\,E}\,(\sin\phi - \sin\phi_s) \end{cases} \tag{2.28}$$

where $q = Z\,e$ is the ion charge, E is the beam energy. Longitudinal motion is connected with transverse via the slip factor η. Particles with a relatively small z or energy offset then have oscillatory trajectories,

$$z(t) = z_0\,\cos(\omega_0\,Q_s\,t + \phi_0) \tag{2.29}$$

where z_0 and ϕ_0 are the initial conditions. The synchrotron tune Q_s,

$$Q_s = \sqrt{-\frac{\eta\,h\,Z\,e\,V\,\cos\phi_s}{2\pi\,\beta_r^2\,E}} \tag{2.30}$$

is usually much smaller than the betatron tune $Q_s \ll Q$. A single particle in a synchrotron oscillates in both transverse and longitudinal planes, however longitudinal synchrotron oscillations are slower than transverse betatron oscillations.

Equations (2.28) correspond to a Hamiltonian [67],

$$H = \frac{1}{2}\,h\,\eta\,\omega_0\left(\frac{\Delta p}{p}\right)^2 + \frac{\omega_0\,q\,V}{2\pi\,\beta_r^2\,E}\left[\cos\phi - \cos\phi_s + (\phi - \phi_s)\,\sin\phi_s\right]. \tag{2.31}$$

The nonlinear landscape of H on longitudinal phase space is used to separate closed trajectories from unbound ones. As an example, Fig. 2.5 depicts particles (blue dots) in longitudinal phase space of SIS100.

Colors correspond to the levels of Hamiltonian, the black closed curve represents the separatrix ($H = 0$). The area inside this closed curve is the RF bucket. If particles leave the RF bucket, they eventually drift towards the vacuum chamber. As a result, the RF creates the structure with varying charge density along z of beams in synchrotrons. Such beams are known as *bunched beams*. The number of RF buckets h (the RF harmonic number) determines the maximum number of bunches in the beam. For some applications, synchrotrons operate without RF. In this case, the charge density is uniform along the longitudinal offset for $-C/2 \le z \le C/2$. Beams distributed longitudinally in this way are often referred to as “coasting” or “continuous” beams.

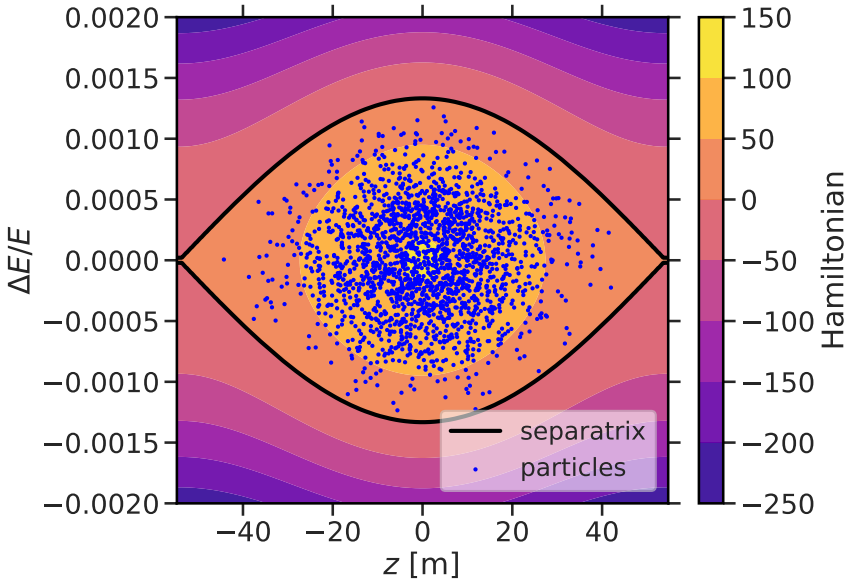

Figure 2.5: The longitudinal phase space of SIS100: levels of the Hamiltonian (color), separatrix (solid black line), and particles in the bunched beam (blue dots).

2.3 Gradient errors and the half-integer resonance

If the betatron (bare) tune Q is an integer number n divided by two, the phase advance per one turn $2\pi\mu$ corresponds to πn. Thus, a single particle reaches the same point in phase space after one revolution (if n is even) or two turns (if n is odd) in an ideal machine. Figure 2.6 illustrates the trajectory of such a particle in the vertical phase space at $s = 0$ location in the synchrotron for $n = 1$ example. A single additional quadrupole magnet (also placed at $s = 0$) acts as an imperfection.

The initial coordinates (y_0, y_0') of the particle are represented by the black dot. The particle then rotates clockwise, the trajectory is represented by black solid and dashed lines for odd and even revolutions respectively. The displacement y changes sign in after each turn because $2\pi\mu = \pi$. Therefore, the error kick by the additional quadrupole (which is proportional to the displacement y, shown with red arrows), accumulates in time. Eventually, the increasing amplitude of betatron oscillations exceeds the aperture of the vacuum chamber. After that, the particle is considered

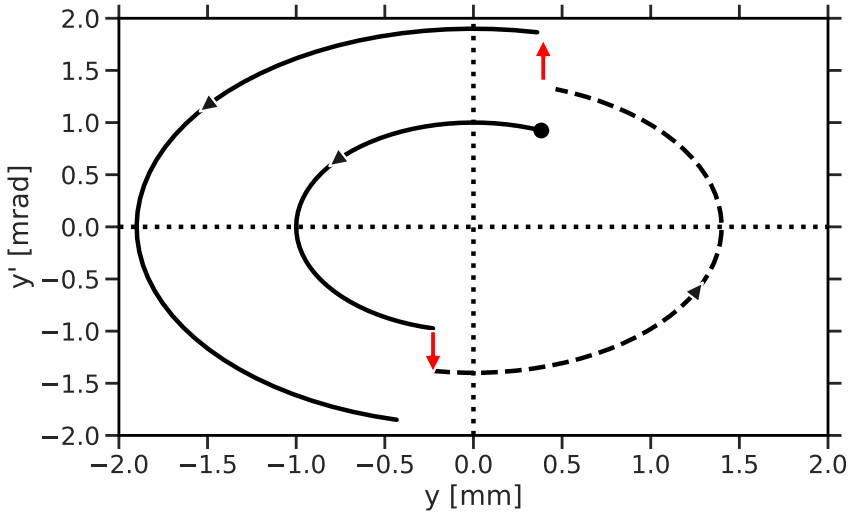

Figure 2.6: Particle trajectory resulting from an additional quadrupole kick $\Delta y' = -y/f$ on the half-integer resonance, f is the focal length of the additional (error) quadrupole (red arrows).

"lost". In the case of $n = 2$, the situation is similar. The only difference is that the particle receives the same kick each turn. As a result, for any integer number n, the distribution of particles cannot be conserved in the synchrotron if $Q = n/2$.

Let us now consider the case of multitudinous error kicks distributed in the machine. The function $\Delta k(s)$ describes a deviation from the betatron focusing. Though this deviation can be caused by the incorrect values of the integral focusing strength in quadrupoles (gradient errors) and by the displacement of sextupoles, octupoles, etc (feed-down effect), this work considers only the impact of gradient errors. In this case, the single-particle equation,

$$w''(s) + k(s)\,w - \frac{1}{w(s)^3} = -\Delta k(s)\,w\,. \tag{2.32}$$

We consider here small-amplitude deviation of the function w, namely, $w = w_0 + \Delta w$, where w_0 satisfies Eq. (2.14). The perturbation function $\Delta k(s)\,w$ is periodic

of the path length s and can be expanded in a Fourier series. Using the normalized coordinate $\phi = \int \frac{ds}{Q\beta}$, this equation becomes

$$\frac{\mathrm{d}^2(\Delta w/w)}{d\phi^2} + 4Q^2\,(\Delta w/w) = 2Q \sum_{p=0}^{\infty} F_p \,\exp\left(i\,p\,\phi\right), \tag{2.33}$$

where

$$F_n = \frac{1}{2\pi} \oint \beta(s)\,\Delta k(s)\,\exp\left(-i\,n\,\frac{2\pi\,\mu(s)}{Q}\right) \mathrm{d}s\,, \tag{2.34}$$

The solution becomes

$$\Delta w/w = -\frac{Q}{2} \sum_{p=0}^{p=\infty} \frac{F_p\,\cos\left(p\,\phi\right)}{Q^2 - (p/2)^2} \tag{2.35}$$

The harmonic $p = n$ has the strongest contribution, when $Q \simeq n/2$. Since $|\Delta w/w|_{\max} \simeq 1$ at $Q \simeq n/2 + F_n/2$, the absolute value of the integral F_n is the stop-band width at zero intensity for the half-integer $Q \simeq n/2$ resonance. As a result, the strength of $\Delta k(s)$ can be quantified using stop-band integrals, as first introduced by Courant and Snyder [44]. Another consequence of gradient errors in a synchrotron is reflected in the shift of bare tunes $\Delta Q = -\frac{1}{2} F_0$ (see e.g. Ref. [25]). In this work, we use the SIS100 lattice as an example of a synchrotron featuring a gradient error.

A survey of the quadrupole magnets in the SIS100 lattice is shown in Fig. 2.7. In our study case, the initial gradient error is given by a doublet of radiation-hard normal-conducting quadrupole magnets (red squares). These "warm" quadrupoles replace two superconducting "cold" magnets (blue circles) and thus supply weaker focusing strength. While the integral focusing strength is restored by an increased length of the warm magnets, this setup by design breaks the symmetry of the lattice. The detailed lattice model is described in Ref. [32]. We control the gradient error using two quadrupole corrector magnets (orange triangles) located close to the warm quadrupole doublet.

Three basic scenarios of gradient-error strength are considered in our study: (1.) *weak* gradient error with correctors powered near their optimal values (the optimization is discussed in a greater detail in Sec. 5), (2.) *intermediate* gradient error due to corrector current reduced to 75%, and (3) *strong* gradient error with corrector current at 50%. Corresponding values of F_{37} ($n = 37$), the gradient-error strength, are listed in Table 2.1. Details on how these values are obtained are given in Sec. 4.2.

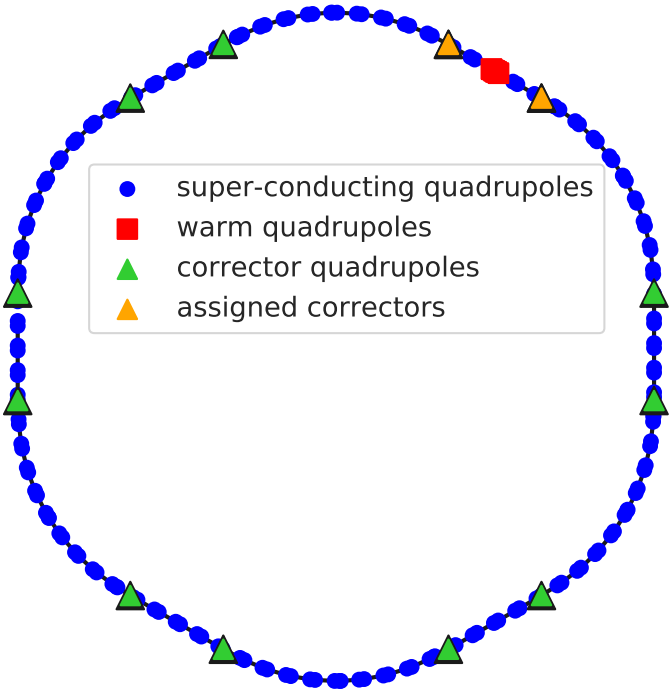

Figure 2.7: Survey of SIS100 gradient-error setup.

Gradient errors modify the transverse dynamics of the beam. A useful observable are the RMS beam envelopes, defined as the statistical beam moments $\sigma_x = \sqrt{\langle x^2 \rangle - \langle x \rangle^2}$ and $\sigma_y = \sqrt{\langle y^2 \rangle - \langle y \rangle^2}$ where the averaging $\langle \cdot \rangle$ is performed over a beam distribution. In the case of absent gradient errors and space charge, they have their design values expressed as

$$\begin{cases} \sigma_x(s) = \sqrt{\epsilon_x \beta_x(s) + D(s)^2 \sigma^2_{(\Delta p/p)}} \\ \sigma_y(s) = \sqrt{\epsilon_y \beta_y(s)} \end{cases} \tag{2.36}$$

with the horizontal dispersion function D(s), where $\sigma_{(\Delta p/p)}$ is the RMS momentum spread. Usually, the vertical dispersion in synchrotrons like SIS100 is negligible.

Table 2.1: Reference values of F_{37} for three gradient-error scenarios

	weak	intermediate	strong
F_{37}	$0.6 \cdot 10^{-3}$	$2.6 \cdot 10^{-3}$	$4.3 \cdot 10^{-3}$

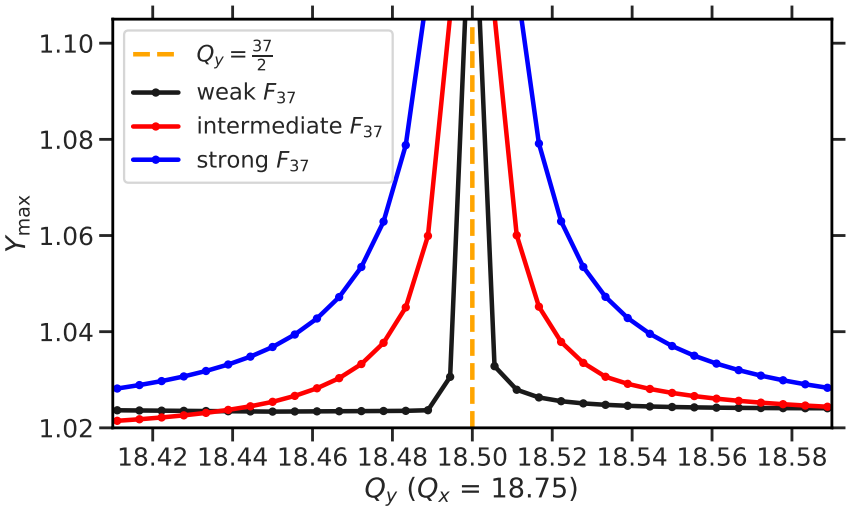

Figure 2.8: Response of vertical envelopes to the bare vertical tune for different gradient-error examples which are used in the work. Weak, intermediate, and strong gradient-error scenarios (see text for details) are shown in black, red, and blue.

Therefore, we exclude it from our study. SIS100 is planned to operate above $Q_y = 18.5$, hence, $n = 37$ in our case for the vertical half-integer resonance. Also, we choose the vertical plane for probing the $\frac{37}{2}$ half-integer resonance at $Q_x = 18.75$ to isolate the gradient-error resonance from other influences, for example, possible dispersion-related effects [71].

Figure 2.8 illustrates the impact of these three gradient-error scenarios with plots of the response curves $Y_{\max} = \mathrm{Max}[\sigma_y / \sqrt{\epsilon_y \beta_y}]$ in terms of matched envelopes vs the vertical bare tune Q_y. Max[·] indicates the maximum along the path length s. The horizontal bare tune remains fixed at $Q_x = 18.75$.

The orange dashed line shows the location of the half-integer bare tune. Lines with black, red, and blue colors depict different response curves corresponding to

the increasing value of the gradient-error strength. The vertical RMS envelope increases around the resonance condition at the bare tune of $Q_y = 18.5$, and the stop band becomes wider for stronger gradient errors. This is the usual behavior which is observed close to the quadrupolar resonance at negligible intensities.

3 Space charge and envelope dynamics

This chapter describes how the half-integer resonance (introduced above as a single-particle effect) modifies when particles start interacting with each other with the main focus on space charge. A detailed discussion on space-charge dynamics in accelerators can be found in Refs. [30, 49]. The analytical concepts described below apply to coasting beams and are used here to quantify space charge strength.

3.1 Why space charge is important

Let us consider a simplified case of a uniformly charged coasting beam with a circular cross-section shown in Fig. 3.1. The line charge density is λ, the radius is r_0.

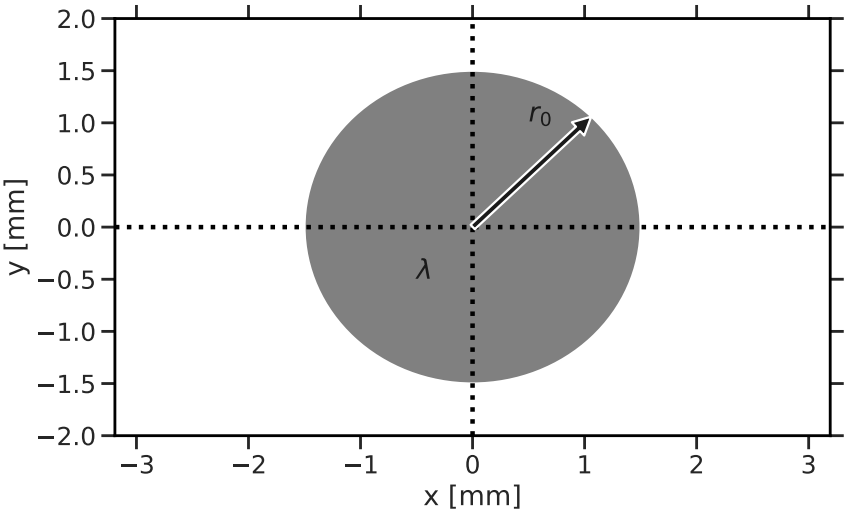

Figure 3.1: Uniformly charged round beam.

The electric potential of such a beam acts on a test (charged) particle like the electric potential of a charged cylinder. Using Gauss law, the electric field $\tilde{E}(r)$ results in

$$\begin{cases} \tilde{E}(r) = \frac{\lambda}{2\epsilon_0} r, & r \leq r_0 \\ \tilde{E}(r) = \frac{\lambda}{2\epsilon_0} \frac{r_0^2}{r}, & r \geq r_0 \,. \end{cases} \tag{3.1}$$

The vacuum permittivity is indicated as ϵ_0. The electric field is linear with respect to an arbitrary offset r inside the cylinder, then it drops as $\propto 1/r$ for any $r > r_0$. The blue line in Fig. 3.2 shows the projection of the electric field along the y-axis.

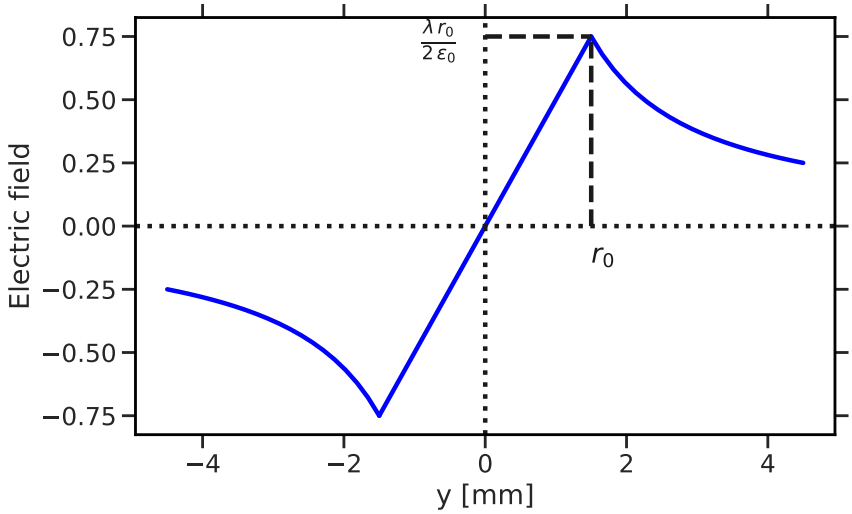

Figure 3.2: Electric field of a uniformly charged round beam.

Any particle inside the beam ($r \leq r_0$) receives a kick proportional to its offset. This kick pushes the particle away from the equilibrium orbit. As a result, it effectively acts like a defocusing force known as a direct space charge. This chapter later demonstrates how space charge scales down with increasing γ_r. Therefore, this effect is of relevance for hadron synchrotrons with relatively low energy.

3.2 RMS envelope equations

Let us consider a distribution of particles,

$$f = f(x, x', y, y'), \tag{3.2}$$

in a coasting beam with the negligible momentum spread. Particles obey the single-particle equations

$$\begin{cases} u' = p_u/p \\ (p_u/p)' = F(x,s)\,, \end{cases} \tag{3.3}$$

where u is either x or y, and $F(x,s)$ includes both the external force and the self-force (space charge in our case), namely, $F = F_{\text{ext}} + F_{\text{self}}$. Averaging equations over the distribution $f(x, x', y, y')$ results in

$$\begin{cases} \langle u\rangle' = \langle p_u/p\rangle \\ \langle p_u/p\rangle' = \langle F_{\text{ext}}\rangle\,, \end{cases} \tag{3.4}$$

using the function of the transverse focusing by quadrupole magnets $k(s)$ from Eq. (2.5) we obtain

$$\langle u\rangle'' + k(s)\,\langle u\rangle = 0\,. \tag{3.5}$$

Therefore, the center of charge depends only on the linear external force $F_{\text{ext}} = k(s)u$. Next, let us turn to the second moments of the distribution $f(x, x', y, y')$,

$$\begin{cases} \langle u^2\rangle' = 2\,\langle u\,u'\rangle = 2\,\langle u\,\frac{p_u}{p}\rangle \\ \langle u\,\frac{p_u}{p}\rangle' = \langle u'\,\frac{p_u}{p}\rangle + \langle u\left(\frac{p_u}{p}\right)'\rangle = \langle\left(\frac{p_u}{p}\right)^2\rangle - k(s)\,\langle u^2\rangle + \langle u\,F_{\text{self}}\rangle \\ \langle\left(\frac{p_u}{p}\right)^2\rangle' = 2\,\langle\frac{p_u}{p}\left(\frac{p_u}{p}\right)'\rangle = -2\,k(s)\,\langle u\,\frac{p_u}{p}\rangle + 2\,\langle\frac{p_u}{p}\,F_{\text{self}}\rangle\,, \end{cases} \tag{3.6}$$

where $\langle\frac{p_u}{p}\,F_{\text{self}}\rangle$ and $\langle u\,F_{\text{self}}\rangle$ depend only on the second moments if linear self-forces are considered. Since the area in the phase space (u, u'),

$$\sqrt{\langle u^2\rangle\langle (u')^2\rangle - \langle u\,u'\rangle^2} = \epsilon_u\,, \tag{3.7}$$

is the RMS emittance which is constant. In the case of uniformly charged coasting beams (known as Kapchinsky-Vladimirsky KV [45]) with the elliptical cross-section, the uniform charge density is defined by $\lambda = qN/(\pi\sigma_x\sigma_y)$, where the ellipse is:

$$\frac{x^2}{\sigma_x^2} + \frac{y^2}{\sigma_y^2} = 1\,. \tag{3.8}$$

Then, the electric field in the laboratory frame inside the beam is [72]:

$$\tilde{E}_x = \frac{\lambda}{\pi\epsilon_0}\,\frac{x}{\sigma_x\,(\sigma_x\,+\sigma_y)}\,,\ \tilde{E}_y = \frac{\lambda}{\pi\epsilon_0}\,\frac{y}{\sigma_y\,(\sigma_x\,+\sigma_y)}\,, \tag{3.9}$$

and the magnetic field is:

$$B_x = -\frac{\beta_r}{c} E_y \, , B_x = \frac{\beta_r}{c} E_x \, , \tag{3.10}$$

where $\sigma_u = \sqrt{\langle u^2 \rangle}$ is the RMS beam size (assuming here $\langle u \rangle = 0$ and $\langle u' \rangle = 0$). Using the Lorentz force Eq. (2.1), the resulting F_{self} inside the beam in both horizontal and vertical planes is:

$$\begin{cases} F_x = \frac{q\,\lambda}{\pi \epsilon_0 \beta_r^2 \gamma_r^2 p} \frac{x}{\sigma_x (\sigma_x + \sigma_y)} \\ F_y = \frac{q\,\lambda}{\pi \epsilon_0 \beta_r^2 \gamma_r^2 p} \frac{y}{\sigma_y (\sigma_x + \sigma_y)} \, . \end{cases} \tag{3.11}$$

Finally, we can combine the second beam moments from Eq. (3.6) in the pair of envelope equations,

$$\begin{cases} \sigma_x'' + \tilde{k}_x(s)\,\sigma_x - \epsilon_x^2/\sigma_x^3 - \frac{K_{\text{sc}}}{2(\sigma_x + \sigma_y)} = 0 \\ \sigma_y'' + \tilde{k}_y(s)\,\sigma_y - \epsilon_y^2/\sigma_y^3 - \frac{K_{\text{sc}}}{2(\sigma_x + \sigma_y)} = 0 \end{cases} \tag{3.12}$$

on σ_x and σ_y, $\sigma_u'' = \mathrm{d}^2\sigma_u/\mathrm{d}s^2$ (both horizontal and vertical), where the external focusing $\tilde{k}(s) = k(s) + \Delta k(s)$ includes the term $\Delta k(s)$ which is a gradient error. The space-charge *perveance* defined as

$$K_{\text{sc}} = \frac{Z\,e\,I}{2\,\pi\,\epsilon_0\,m_0\,(\gamma_r\,\beta_r\,c)^3} \tag{3.13}$$

appears in both equations in the last term which corresponds to space charge contribution. The beam peak current is $I = \lambda\,\beta_r\,c$, $q = Z\,e$ is the ion charge, and m_0 is the rest mass of the ions. This pair of equations (originally derived for KV distributions) describes the behavior of RMS transverse beam sizes for the wide range of transverse distributions with ellipsoidal symmetry [49].

3.2.1 Analytical approach

In this work, while studying the case of SIS100, the horizontal bare tune remains fixed at $Q_x = 18.75$. The quadrupolar stop band at lower $Q_y < Q_x = 18.75$ bare tunes is defined by the equation on the vertical envelope σ_y because the motion is only loosely coupled between vertical and horizontal planes. Therefore, the system can be reduced to one equation. To further simplify the system, we use the smooth focusing approximation via constant $k(s)$ and $\beta(s)$ with the independent variable

$\phi = 2\,\pi\,\mu(s)/Q$. Then, the gradient error is represented by $2Q\sum F_p\cos(p\,\phi)$. The first term is:

$$\frac{\mathrm{d}^2\sigma_y}{\mathrm{d}s^2} = \frac{1}{R^2}\frac{\mathrm{d}^2\sigma_y}{\mathrm{d}\phi^2} \tag{3.14}$$

where R is the effective ring radius. Next, the space-charge term

$$\frac{K_{\mathrm{sc}}}{2(\sigma_x+\sigma_y)} \simeq \frac{K_{\mathrm{sc}}}{2(\langle\sigma_x\rangle+\langle\sigma_y\rangle)}\frac{\sigma_y}{\langle\sigma_y\rangle}\frac{2Q_y}{2Q_y} = 2Q_y\,\Delta Q^y_{\mathrm{KV}}\,\sigma_y \tag{3.15}$$

with averaging $\langle\cdot\rangle$ over the path s, where the space-charge perveance is combined in the KV tune shift ΔQ_{KV},

$$\Delta Q^y_{\mathrm{KV}} = -\frac{K_{\mathrm{sc}}R^2}{4\,\langle\sigma_y\rangle\,(\langle\sigma_x\rangle+\langle\sigma_y\rangle)Q_y}\,, \tag{3.16}$$

originally derived in Ref. [45]. The KV tune shift grows linearly with increasing peak current and vanishes at high energies because of relativistic Lorenz factors β_r and γ_r in the denominator of the space-charge perveance.

The equation on the vertical beam size is combined as:

$$\sigma_y'' + (Q_y^2 - 2Q_y\,\Delta Q^y_{\mathrm{KV}})\sigma_y - \frac{R^2\,\epsilon_y^2}{\sigma_y^3} = 2Q_y\sum_p F_p\cos(p\,\phi)\,\sigma_y\,, \tag{3.17}$$

where $\sigma_y'' = \mathrm{d}^2\sigma_y/\mathrm{d}\phi^2$. Within a tune distance of $\simeq \frac{1}{4}\Delta Q^y_{\mathrm{KV}}$ to $Q_y = Q_x = 18.75$ [51], the 1D approximation of envelope equations breaks. This is sufficiently far away from the half-integer resonance, and we can neglect this effect in our study. Equation (3.17) (while substituting $\sigma_y = w\sqrt{\epsilon}$) at zero space charge and the gradient-error strength ($\Delta Q^y_{\mathrm{KV}} = 0$ and $F_p = 0$) recovers Eq. (2.14).

Let us examine small-amplitude solutions of Eq. (3.17) $\frac{\sigma_y}{\sqrt{\epsilon\,\beta}} = 1+\delta$, where $\sqrt{\epsilon\,\beta}$ correspond to the vertical beam size without space charge and gradient errors. For $\delta \ll 1$ and $\Delta Q^y_{\mathrm{KV}}/Q \ll 1$, the equation becomes

$$\delta'' + 4(Q_y^2 - C\,Q_y\,\Delta Q^y_{\mathrm{KV}})\,\delta = 2Q_y\sum_p F_p\cos(p\,\phi)\,, \tag{3.18}$$

where transverse beam geometry determines the constant C [51]. In the SIS100 example the beam has $2b = a$, hence $C = 2/3$. The resulting equation corresponds to driven undamped oscillations,

$$\delta(\phi) = \frac{Q_y}{2}\cdot\sum_p \frac{F_p\cos(p\,\phi)}{Q_y^2 - Q_y\,C\,\Delta Q_{\mathrm{KV}} - (\frac{p}{2})^2}\,. \tag{3.19}$$

Table 3.1: Reference parameters of the nominal uranium bunch distribution for SIS100 used in simulations

Parameter	Value
Particle	$^{238}U^{28+}$
Ring circumference	1083.6 m
2D transverse distribution	Gaussian (3.5σ truncated)
Peak current	1.45 A
Energy	200 MeV/u
$\Delta Q^{y}_{\mathrm{KV}}$	0.15

This work elaborates on the half-integer resonance. As shown above, $Q \simeq n/2$. Therefore, the term where $p = n$ has the strongest contribution. However, the linear resonance condition is shifted from the exact half-integer value by space charge [49]. Now, the envelope mode is in resonance at

$$2Q - \Delta Q_{\mathrm{env}} = n\,, \tag{3.20}$$

where the envelope tune shift amounts to

$$\Delta Q_{\mathrm{env}} = 2\,C \cdot \Delta Q_{\mathrm{KV}}\,. \tag{3.21}$$

For example, the resonance condition is met at $Q_y = 18.5$ at zero intensity, whereas for nominal parameters, the space charge shifted condition is met at a bare tune of $Q_y = 18.6$. Nominal parameters for SIS100 $^{238}U^{28+}$ heavy-ion beam at injection energy are listed in Table 3.1[1]. Often the maximum tune shift due to space charge in a Gaussian distribution, $\Delta Q_{\mathrm{Gauss}}$, is indicated as space charge strength: for fixed RMS emittances, it amounts to twice the KV tune shift, $\Delta Q_{\mathrm{Gauss}} = 2 \cdot \Delta Q_{\mathrm{KV}}$.

Throughout this work, to study the trends at varying space charge strength, the beam intensity is varied between zero and the nominal value corresponding to the envelope tune shift between $0 \leq \Delta Q_{\mathrm{env}} \leq 0.2$. To maintain the same space charge strength for both coasting and bunched beams, the line charge density is scaled to obtain the same peak current.

[1] The values of $\Delta Q^{y}_{\mathrm{KV}}$ and ΔQ_{env} correspond to transverse geometric RMS emittances $\epsilon_x = 8.75\,\mathrm{mm\,mrad}$, $\epsilon_y = 3.75\,\mathrm{mm\,mrad}$, and an RMS momentum spread $\sigma_{(\Delta p/p)} = 0.45 \cdot 10^{-3}$ with an RMS bunch length of $\sigma_z = 13.2\,\mathrm{m}$.

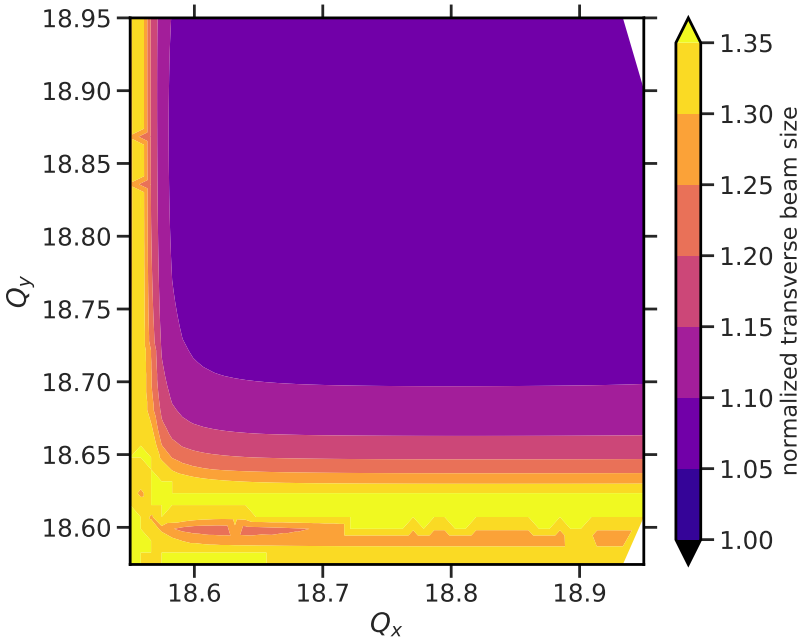

Figure 3.3: Numerical computations of RMS envelope equations for the nominal beam parameters of SIS100. Levels of the transverse beam size (normalized by the unperturbed one) are indicated by different colors.

3.2.2 Numerical solution of 2D RMS envelope equations

Let us now turn to a numerical example of a quadrupolar stop band with space charge. RMS envelope equations [49] determine the location of the quadrupolar resonance depending on space charge for coasting beams distributed with transverse ellipsoidal symmetry.

In the work, the matched solutions and envelope modes are numerically computed via a envelope solver code, implemented by Prof. Dr. Oliver Boine-Frankenheim in Python [73] and used in several peer-reviewed publications like Refs. [74–76]. This code uses the matrix approach described in Eq. (2.24), where transport matrices are computed via MAD-X. Then, space-charge nodes are inserted after each element as

$$M = T(s_0|s_1) \cdot T_{\mathrm{sc}}(1) \cdot T(s_2|s_1) \cdot \ldots \cdot T(s_N|s_0) \cdot T_{\mathrm{sc}}(N), \tag{3.22}$$

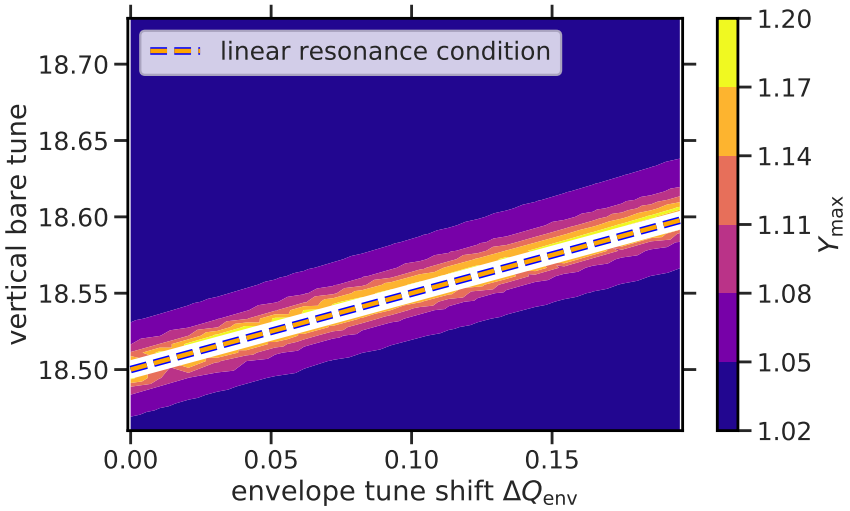

Figure 3.4: Solution of RMS envelope equations for the strong gradient-error scenario, the normalized vertical envelope is shown with color levels, the dashed orange line represents the linear resonance condition (see text for details).

with

$$T_{\mathrm{sc}}(k) = \begin{pmatrix} 1 & 0 \\ 1/f_{\mathrm{sc}}(k) & 1 \end{pmatrix}, \tag{3.23}$$

where

$$1/f_{\mathrm{sc}}(k) = -\frac{K_{\mathrm{sc}}\, C}{2\,\sigma_{x,y}\left(\sigma_x + \sigma_y\right)}\,(s_k - s_{k-1}) \tag{3.24}$$

K_{sc} is the space-charge perveance defined in Eq. (3.13). Therefore, this implementation accounts lattice imperfections in magnets (provided via MAD-X), and corresponding linear space-charge force. In the numerical computation, the iterative scheme and the shooting method are employed to find the matched solution.

As mentioned above (see Sec. 2.3), SIS100 features a gradient error. Figure 3.3 shows the change of the normalized transverse beam size $\mathrm{Max}\left[\frac{\sigma_x+\sigma_y}{\sigma_{x,0}+\sigma_{y,0}}\right]$ with respect to the bare tunes of the machine, where $\sigma_{x,0} = \sqrt{\epsilon_x\,\beta_x + D^2\,\sigma^2_{\Delta p/p}}$ and $\sigma_{y,0} = \sqrt{\epsilon_y\,\beta_y}$ respectively, and $\mathrm{Max}[\cdot]$ is taken over the path s. Thick yellow lines

indicate the locations of the half-integer stop bands (horizontal and vertical). Inside the vertical stop band the change of colors below $Q_y = 18.6$ is associated with nonlinearities of the envelope equations.

Next. Fig. 3.4 illustrates the numerical solution of these equations for KV beams in terms of matched envelopes $Y_{\max} = \mathrm{Max}[\sigma_y/\sqrt{\epsilon_y \beta_y}]$, Max$[\cdot]$ is taken over the path s.

The dark blue area depicts the resonance-free areas, whereas the area with the strong deviation of the vertical envelope is shown with yellow. Note that the blue response curve in Fig. 2.8 is the projection of the color plot in Fig. 3.4 at zero space charge. The lines of the same color above and below the linear resonance condition (orange dashed line) are parallel. This indicates that the stop-band width of the half-integer resonance for KV coasting beams is independent of space charge.

4 Stop band characterization by tracking

The following chapter describes in detail how the width of the half-integer resonance changes with varying space charge and a gradient error. The core results of the chapter are published in Ref. [77] by the author.

There is a particular interest regarding the extension of the resonance from the linear resonance condition toward the stop-band edges for realistic Gaussian-like distributed bunched beams. As shown in Sec. 3.2, the linear resonance condition in Eq. (3.20) is valid for coasting KV beams. It is generalized in Ref. [49] for a wide range of transverse beam distributions of coasting beams. The RMS 3D envelope equations derived in Ref. [50] can be applied to the case of bunched beams. In this work, the case of bunched beams is addressed using macro-particle simulations. Similar simulations are utilized to study the half-integer stop band for KV beams in Ref. [62] and waterbag beams in Ref. [30] for coasting beam conditions. Throughout this work, while comparing coating and bunched beams we employ equal peak current conditions to obtain the same maximum strength of space charge in both cases.

4.1 Simulation model

A single-particle trajectory can be found by solving the Lorentz force equation with any degree of accuracy. However, in the case of an intense bunch of particles interacting with each other, finding exact solutions to the equations of motion is not practical. Indeed, the number of particles in a beam is typically $\geq 10^{10}$. Moreover, in the presence of space charge, the mathematical analysis becomes considerably more complex. Consequently, tracking codes are crucial for studying beam dynamics and designing synchrotrons with collective effects. In this work, the GSI computer cluster Virgo [78] is used to perform extensive simulations.

4.1.1 Particle tracking

The numerical simulation setup consists of macro-particle tracking through the accelerator lattice. The beam is represented by macro particles. Each macro particle

carries the charge of a set of particles. A set of macro particles is generated by sampling a bivariate Gaussian distribution for the phase space of each transverse plane, matched to linear optics. This means, that transverse beam sizes of the distribution correspond to $\sigma_x = \sqrt{\epsilon_x \beta_x + D^2 \sigma^2_{\Delta p/p}}$ and $\sigma_y = \sqrt{\epsilon_y \beta_y}$ defined in Sec. 2.1. The bunched beam is generated with a longitudinal bivariate Gaussian distribution, whereas the coasting beam is initialized with zero momentum spread.

The library SixTrackLib [79] is utilized for symplectic single-particle tracking through the lattice with gradient errors. Alternatively, this part of simulations can be done, for example, in MAD-X [80], ELEGANT [81], and SAD [82]. Single-particle tracking is implemented as follows. As discussed above, the coordinates of a particle are represented by a 6D vector which is modified by a lattice element via

$$\begin{pmatrix} x \\ x' \\ y \\ y' \\ z \\ \Delta p/p \end{pmatrix}_2 = T(s_1|s_2) \cdot \begin{pmatrix} x \\ x' \\ y \\ y' \\ z \\ \Delta p/p \end{pmatrix}_1 , \tag{4.1}$$

where $T(s_1|s_2)$ is a 6×6 matrix.

Next, the direct space-charge interaction is modeled by lumped kicks which are applied in short steps along the lattice as additional elements (space-charge nodes). In a real machine, space-charge forces follow the beam throughout the passage. Therefore, the number of space-charge nodes should be comparable to the number of elements in the lattice to mimic the actual smoothly-distributed force. Space charge is computed using the slice-by-slice or 2.5D particle-in-cell (PIC) solver with PyHEADTAIL tracking code [83]. In general, PIC algorithms resolve space charge self-consistently [84], namely, the space-charge potential depends on the actual distribution of particles (and the change of this distribution) throughout the simulation. Thus, PIC codes are suitable for modeling the coherent motion of a beam (dynamics of transverse beam sizes in particular). As an alternative to PyHEADTAIL, such codes as PyORBIT [85] and TraceWin [86] can be used for PIC simulations in synchrotrons. Since PIC solvers in PyHEADTAIL can work on GPU, and the combination of SixTrackLib with PyHEADTAIL tracking is implemented on Virgo to provide the results for SIS100 beam loss studies [32], these codes are used throughout the work.

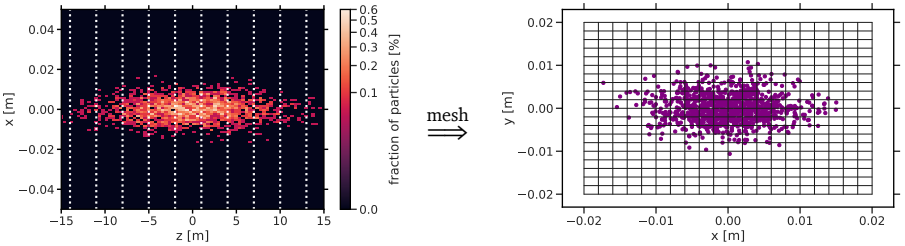

Figure 4.1: 2.5D PIC space-charge principle: Longitudinal slicing of the beam (white dashed vertical lines on the left). For each longitudinal slice, the transverse charge density is interpolated on the grid (black solid lines on the right).

Statistical beam moments (see e.g. Ref. [67]) are used to analyze the results of particle tracking,

$$\begin{cases} \sigma_y^2 = \langle y^2 \rangle - \langle y \rangle^2 \\ \sigma_{y'}^2 = \langle y'^2 \rangle - \langle y' \rangle^2 \\ \sigma_{yy'} = \langle (y - \langle y \rangle)(y' - \langle y' \rangle) \rangle \\ \epsilon = \sqrt{\sigma_y^2 \sigma_{y'}^2 - \sigma_{yy'}^2} \end{cases} \tag{4.2}$$

where $\langle \cdot \rangle$ is the averaging over a distribution, the displacement y and the angle $y' = \mathrm{d}y/\mathrm{d}s$ are the coordinates of particles in the vertical phase space. The same procedure in the horizontal plane can be done while replacing y with x.

4.1.2 Particle-in-Cell model

The following part of the chapter describes how the numerical implementation of PIC codes is used to compute space-charge forces.

First, the Lorentz boost is done from the laboratory frame to the rest frame via

$$(x, y, z)_{\mathrm{rest}} = (x, y, \gamma_r z)_{\mathrm{lab}} \,. \tag{4.3}$$

The momentum spread in synchrotrons is small, $\sigma_{\Delta p/p} \ll 1$. Therefore, the relative particle motion is negligible during the integration step, and the problem is electrostatic. Figure 4.1 demonstrates how macro particles are located in cells for numerical integration. First, the beam is split into longitudinal regions (slices), shown with dashed white lines on the left panel. Next, for each slice, a grid in the

transverse plane is initialized (black lines on the right) assuming that the charge density is constant along Δz of a slice. It is important that slices and the grid cover all macro particles in longitudinal and transverse planes respectively. With the resulting mesh charge density ρ, the 2D Poisson equation on the electric potential ϕ,

$$\nabla^2 \phi = -\frac{\rho}{\epsilon_0}, \tag{4.4}$$

is solved for each slice separately, where ∇ is the nabla operator. The solution of the 2D Poisson equation can be written as

$$\phi(x, y) = \frac{1}{4\pi\,\epsilon_0} \int G(x - x_1, y - y_1)\,\rho(x, y)\,dx_1\,dy_1, \tag{4.5}$$

where the Green's function G is defined

$$G(x - x_1, y - y_1) = -\frac{1}{2} \ln\left((x - x_1)^2 + (y - y_1)^2\right) \tag{4.6}$$

for the case of transverse open boundary conditions [87]. To speed up the numerical computations of the electric potential the Fourier transform is used. Using the convolution theorem,

$$\mathscr{F}[\phi] = \mathscr{F}[G] \cdot \mathscr{F}[\rho], \tag{4.7}$$

the electric potential is simply $\phi = \mathscr{F}^{-1}[\mathscr{F}[G] \cdot \mathscr{F}[\rho]]$, where $\mathscr{F}$ is implemented using the Fastest Fourier Transform in the West (FFTW) software library. Next, the electric field in the laboratory frame corresponds to

$$\begin{pmatrix} \tilde{E}_x \\ \tilde{E}_y \end{pmatrix} = -\gamma_r \begin{pmatrix} \frac{\partial \phi}{\partial x} \\ \frac{\partial \phi}{\partial y} \end{pmatrix} \tag{4.8}$$

Taking into account the magnetic field arising after the Lorentz boost, the resulting Lorentz force acts on particles via

$$\begin{pmatrix} \Delta x' \\ \Delta y' \end{pmatrix} = \frac{1}{p} \begin{pmatrix} \Delta p_x \\ \Delta p_y \end{pmatrix} = \frac{q\,\Delta s}{\gamma_r\,\beta_r\,c\,p} \begin{pmatrix} \tilde{E}_x \\ \tilde{E}_y \end{pmatrix}, \tag{4.9}$$

where Δs is the integration step. To study incoherent dynamics of single particles from the beam halo crossing the beam core, simplified models (so-called frozen space charge) can be used. These models integrate the Poisson equation only once at the beginning of the simulation (or use the analytical approximation [88]), and particles receive the same space-charge kicks each turn. In this work, it is crucial to take into account the coherent motion of particles [51] to characterize the half-integer stop band accurately. Therefore, we use a self-consistent 2.5D PIC model.

4.1.3 Model limitations and convergence studies

Although PIC is known to provide accurate computations of space charge, this model should be set in a proper way to account for its limitations. First, the grid size in horizontal and vertical directions should be initialized regarding the ratio of transverse beam sizes to keep the same resolution. In the case of SIS100, a square grid can be used because $\sigma_x/\sigma_y \simeq 1.5$. Next, the amount of macro particles should be sufficient enough to have $\gtrsim 1$ particles on average per cell. It is also important to keep the number of space-charge nodes large, so a particle receives enough space-charge kicks per one betatron oscillation. The Poisson solver described above has open boundary conditions. In synchrotrons, the grounded vacuum chamber determines physical boundaries. Though in the case of SIS100 $a_y/\sigma_y \simeq 7.5$, where a_y is the vertical aperture, the distortion of the electric potential due to the walls might affect only halo particles. In this work, we focus on the coherent motion of beam-core particles. Therefore, this effect can be neglected.

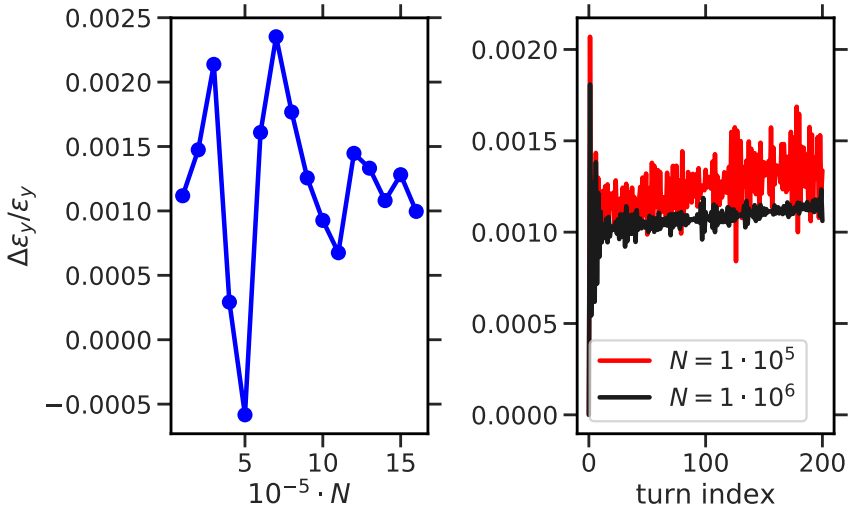

Figure 4.2: The change of the vertical emittance over 200 turns for a bunched beam as a function of the number of macro particles (left, blue curve). Red and black curves (right) are examples of vertical emittance growth for $1 \cdot 10^5$ and $1 \cdot 10^6$ macro particles respectively.

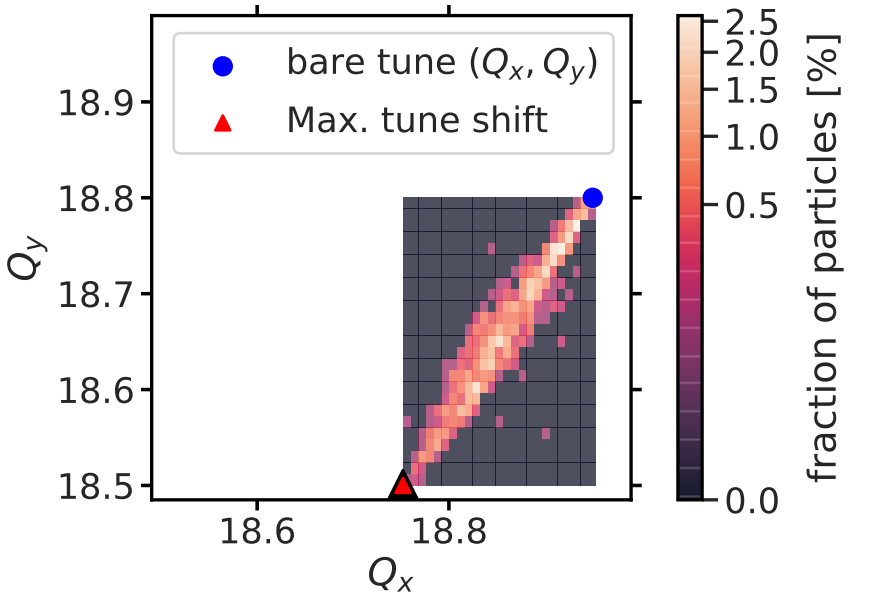

Figure 4.3: Spread of tunes of individual particles in SIS100 at nominal beam parameters for a Gaussian-like distributed bunched beam (see text for details).

In this work, each PIC space-charge node solves the transverse Poisson equation for 64 longitudinal slices along the bunch with 128×128 grid. We use $2 \cdot 10^6$ macro particles with 10^3 space-charge nodes located in the SIS100 lattice. All numerical settings in the simulation model are validated with convergence studies. For example, Fig. 4.2 demonstrates the results of the convergence studies for the number of macro particles for a bunched beam.

With the increasing number of macro particles, the uncertainty of simulation results decreases, and results converge to the same value of transverse emittance growth. Red and black curves (on the right) show the change of the horizontal emittance for 200 turns for two values of the number of macro particles, namely $N = 1 \cdot 10^5$ and $N = 1 \cdot 10^6$. Though both curves have similar behavior, the signal-to-noise ratio for the latter one (black) is smaller.

To verify the simulation model, we compare the results of particle tracking with analytical models. For example, Fig. 4.3 shows the spread of particle tunes (also referred to as the tune spread) in a bunched beam with a Gaussian distribution as one

of the consequences of space charge for the case of nominal beam parameters (see Table 3.1). The blue dot is the working point, which corresponds to the location of Q_x and Q_y without space charge. The frequencies of particle oscillations (color) are computed using the Numerical Analysis of Fundamental Frequencies (NAFF) [89]. As mentioned in Sec. 3.2, the maximum tune shift in a Gaussian-like distributed beam ΔQ_{Gauss} is twice the KV tune shift for RMS emittances, $\Delta Q_{\text{Gauss}} = 0.3$ (nominal beam). In simulation results, we can measure the distance between the blue dot and the red triangle, the minimum of particle frequencies $\text{Min}[Q_y^{\text{part}}]$, where $[\cdot]$ is taken over distribution. Results in Fig. 4.3, $Q_y - \text{Min}[\text{Q}_\text{y}^{\text{part}}] \simeq 0.3$ confirm that the simulation model is accurate.

4.1.4 Computer experiment setup for simulations without chromatic detuning

As described in Sec. 2.1, the momentum spread of a beam results in the chromatic tune spread,

$$\Delta Q(\xi) \simeq Q\,\xi\,\sigma_{\Delta p/p}\,, \tag{4.10}$$

which contributes to the total tune spread of the beam. To separate the contributions by space charge and chromatic detuning the latter can be removed in a computer experiment. To do so, the longitudinal emittance is reduced by a factor of $a_{\epsilon_z} = 10^{-2}$. Alternatively, $\xi_x = \xi_y = 0$ can be achieved by a chromaticity correction via sextupole magnets. However, this approach introduces additional nonlinear fields that excite betatron resonances. Therefore, to accurately characterize the half-integer resonance, the first scheme is used in the computer experiment.

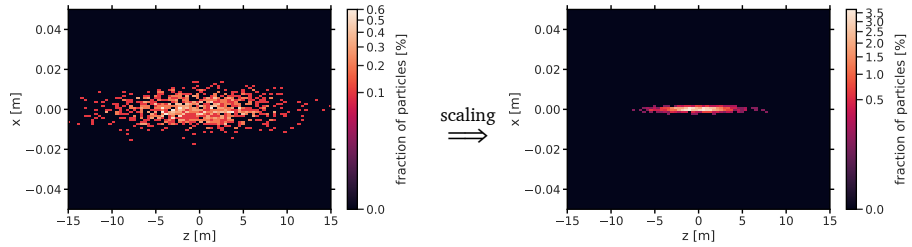

Figure 4.4: Example of a computer experiment setup for chromatic-detuning suppression. Factors $a_{\epsilon_z} = 0.2$ and $a_{\epsilon_{xy}} = 0.02$ are applied to demonstrate the principle.

Another consequence of the reduction of ϵ_z is that transverse and longitudinal sizes turn to be of the same order. Therefore, both transverse emittances are decreased by a factor $a_{\epsilon_{xy}} = 10^{-3}$ to avoid this and the bunch lengthening due to slippage effects and subsequent longitudinal drifting.

Finally, the ratio $I/\sqrt{\epsilon_x \epsilon_y}$ is maintained via multiplying the peak current by $a_{\epsilon_z} a_{\epsilon_{xy}}$ for the space-charge tune shift to remain constant. In this work, several simulations feature the computer-experiment setup described above to suppress the influence of chromatic effects on beam dynamics. We specify in the text when this setup is used, otherwise, simulations are performed at nominal beam parameters.

4.2 Computations of the stop-band width at negligible intensities

The following briefly describes the approach how the half-integer stop-band widths from Table 2.1 are numerically computed.

In the vicinity of the half-integer (inside the stop band), the system becomes unstable. As a result, particle trajectories exponentially diverge in time, and the Twiss parameters become complex. To demonstrate this, we use Methodical Accelerator Design (MAD-X) code [80]. First, the upper and lower edges of the half-integer stop band at negligible intensities are determined by the bare tunes where the numerical computation of beta-functions in MAD-X ceases to converge. Second, MAD-X provides particle tracking for any configuration of the lattice, hence it is possible to observe the unstable motion of particles.

Figure 4.5 depicts the results of particle tracking simulations in MAD-X for the conditions close to the half-integer resonance.

Table 4.1: Quadrupole corrector setup

parameter	corr. #1	corr. #2
beta-function $\beta_y(s)$ [m]	17.8	5.8
phase advance $\mu_y(s)$ [2π]	12.44	13.41
weak $K_1 \cdot L$ [1/m]	-0.004	0.004
intermediate $K_1 \cdot L$ [1/m]	-0.003	0.003
strong $K_1 \cdot L$ [1/m]	-0.002	0.002

The left panel illustrates the beam size growth over time for two values of Q_y, the red curve corresponds to the bare tune inside the stop band (resulting $\Delta\sigma/\sigma$ is exponential), and the black one is outside. For all working points inside the obtained stop bands, trajectories of single particles are found to be unstable which

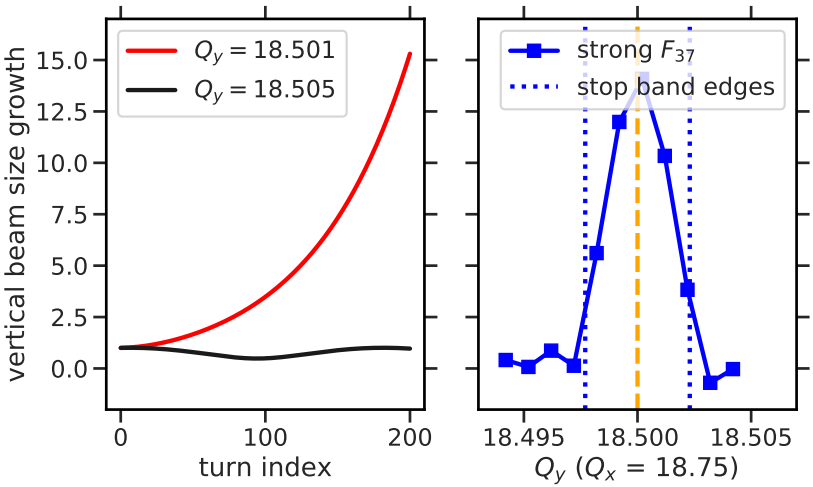

Figure 4.5: The example of how to get the half-integer stop-band width at zero intensity. Unstable (red) vs stable (black) conditions shown on the left, resulting vertical beam size growth $\Delta\sigma_y/\sigma_y$ agains the bare vertical tune (right), the half-integer bare tune $Q_y = 37/2$ is indicated via the orange dashed line.

causes the exponential growth of the vertical beam size in time. On the right, blue squares correspond to the values of the vertical beam size growth after 200 turns, the orange dashed line (like in 2.8) shows the location of the half-integer bare tune. The lower and upper stop-band edges obtained in MAD-X are represented by blue dotted lines.

Based on the gradient-error-free SIS100 lattice, Table 4.1 lists the corresponding beta-functions, phase advances, and integral focusing strengths of the two quadrupole correctors adjacent to the warm quadrupoles for the weak, intermediate, and strong gradient-error scenario, respectively.

4.3 How to determine the stop-band width with space charge

First, we demonstrate how the resonant behavior can be observed in terms of the emittance growth. For illustrative purposes we use the case of the strong gradient error and space charge at nominal SIS100 beam parameters, i.e. the resonance con-

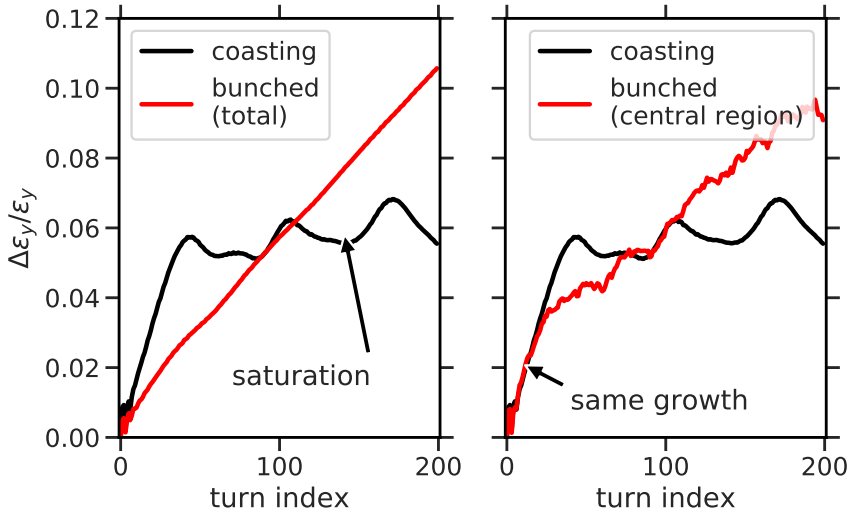

Figure 4.6: The comparison of a coasting beam with a bunched beam in terms of the vertical emittance growth for the strong gradient-error scenario. The working point is located slightly above the linear resonance condition.

dition is met at $Q_y = 18.6$. The bare tunes are set to $Q_x = 18.75$ and $Q_y = 18.62$, slightly above the vertical quadrupolar linear resonance condition. Figure 4.6 displays typical responses to the half-integer resonance. The black curve is identical in both panels and indicates the vertical emittance growth for coasting beam conditions.

The emittance fluctuates over the first $n \simeq 5$ turns before it proceeds to steadily increase linearly until $n \simeq 50$ turns. After that, the emittance reaches a saturation level. The red line on the left side of Fig. 4.6 representing bunched beams shows us exactly the same behavior during the first $n \simeq 5$ turns. Afterward, the emittance increases at a lower rate than for the coasting beam. The red line on the right panel represents the central region of the bunched beam $|z| \ll \sigma_z$. Now the slope of the emittance growth $\frac{1}{\epsilon}\frac{\mathrm{d}\epsilon}{\mathrm{d}n}$ is the same as for the coasting beam in $\simeq 30$ turns. We shall indicate here that the horizontal emittance under the same conditions stays practically constant (gaining less than 0.1% in 2000 turns). This confirms the horizontal and vertical planes are loosely coupled due to space charge.

The dynamics during the first five turns can be explained by the following. The initial transverse distribution is linearly matched to the local optics functions. The

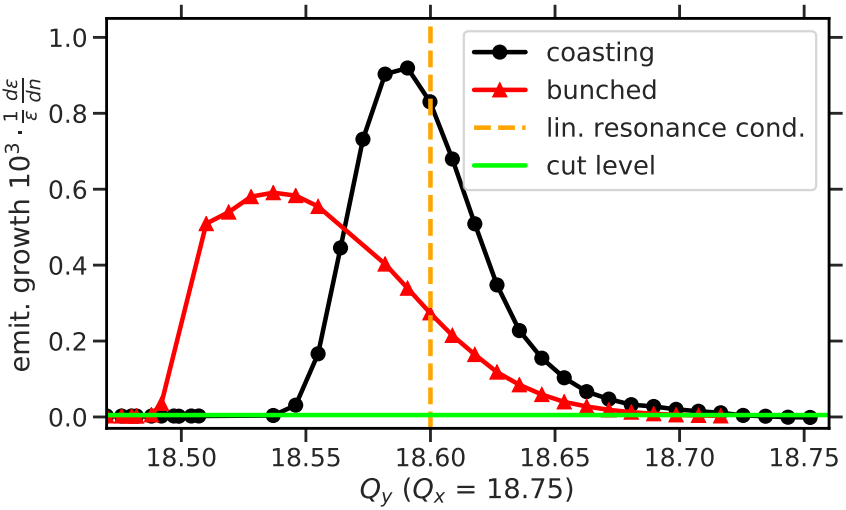

Figure 4.7: Example for the strong gradient-error scenario how to get the stop-band width using the threshold level (lime solid line) from the vertical emittance growth rate for coasting (black dots) and bunched (red triangles) beams.

space-charge potential distorts the phase space and this leads to the mismatch of the generated distribution, which turns to a rapidly decaying initial fluctuation in emittances. Next, the effect of emittance growth saturation appears in the case of coasting beams because of the decreasing space-charge force as the beam size increases. This phenomenon has first been observed by Sacherer in Ref. [49] and is described in greater detail in Ref. [63].

Let us closely inspect in Fig. 4.7 the linear emittance growth regime between the initial mismatch and emittance saturation depending on the bare tune.

With the black dots, we represent the response curve for the coasting beam, whereas the red triangles show the corresponding curve for bunched beams. Both curves sharply rise and have their peaks between $18.47 < Q_y < 18.7$. Outside of this region, the slope of emittance growth remains around a zero level marked by a solid lime green line. Although below the linear resonance condition $Q_y < 18.6$ depicted by the orange dashed line bunched beams have a wider range of tunes affected by the half-integer resonance compared to the coasting beams, above the orange dashed line coasting beams react to the same gradient error in a stronger way. This difference is caused by varying longitudinal charge density in bunched beams.

Let us consider the bare tunes above the orange dashed line. In the case of coasting beams, all longitudinal regions equally interact with the resonance, whereas in bunched beams only a fraction of particles (located in the bunch center) is involved in the emittance growth. That is why the shape of response curves significantly depends on the longitudinal beam distribution.

The height of the solid lime green line determines the lower and upper edges of the stop band. Any working point with emittance growth above this threshold is considered as affected by the resonance. Here and throughout this work we use a threshold level of $\frac{1}{\epsilon}\frac{\mathrm{d}\epsilon}{\mathrm{d}n} = 5 \cdot 10^{-6}$. This amounts to an overall emittance growth of 0.5% during 10^3 turns. For comparison, the injection plateau of SIS100 lasts around one second (or $1.6 \cdot 10^5$ turns), during which the beam emittance would grow by 80% according to this threshold. This may result in non-acceptable particle losses for typical apertures in synchrotrons[1]. Hence, it is important first to identify the location and the width of the stop band, and then to compensate it. Another beneficial aspect of the developed technique of stop-band characterization is that it excludes the effect of the initial distribution mismatch. Though the mismatch can increase with space charge, it does not have any resonant nature. This means that any other technique which compares only final emittances has a systematic error in its design and always provides exaggerated results. Furthermore, the saturation effects are excluded when using the slope of the linear emittance growth. Hence, it is possible to adequately compare the simulation results of bunched and coasting beams.

4.4 Results of short-term simulations

As shown in Chapter 3, the RMS envelope equations determine the quadrupolar resonance condition. This work investigates the extension of the resonance towards the stop-band edges. It is known (for example in Ref. [49] and [47], and demonstrated above in Sec. 3.2) that the stop-band edges shift with space charge in parallel to the linear resonance condition in the case of coasting KV beams. The key results of this section show how, for a transversely Gaussian distributed coasting or bunched beam, the dependence of the stop-band width on space charge significantly differs from the KV case. Figure 4.8 displays the simulation results for 200 turns with Gaussian-like transversely distributed coasting beams, based on the strong gradient-error scenario.

The yellow color represents the area with rapid emittance growth, whereas negligible emittance growth areas are shown in dark blue. Though the peak follows the linear resonance condition, the areas with the same emittance growth above and

[1] The elliptical vacuum chamber of SIS100 has 60 mm × 34 mm dimensions.

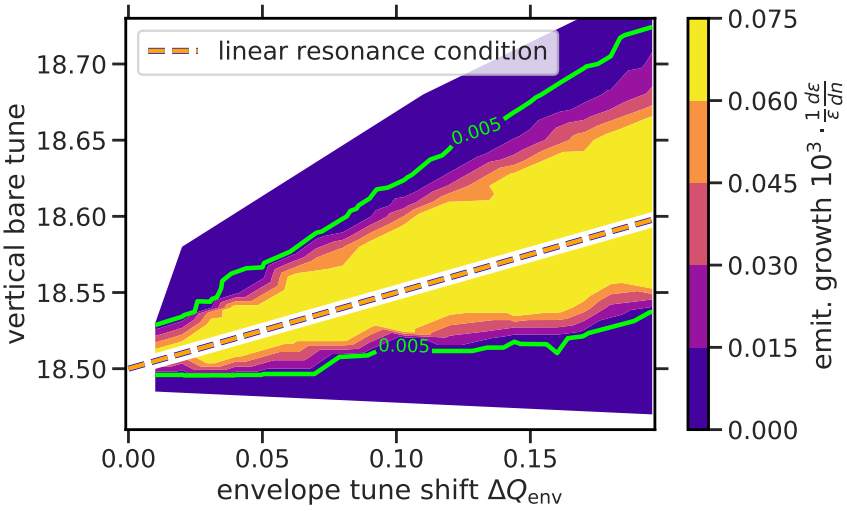

Figure 4.8: Vertical emittance growth rate (color) vs. space charge and the vertical bare tune for coasting beams, the strong gradient-error scenario is used (see text for details).

below the linear resonance condition are not parallel and become wider. In order to investigate how the stop-band width changes with the gradient-error strength and space charge, we use the technique of stop-band width characterization described above.

Figure 4.9 presents the coasting beams results. This plot shows the range of bare tunes affected by the resonance between lower and upper edges. As indicated by the blue squares, the strong gradient error leads to larger stop-band values. Note, that both blue squares on the very right are the lower and upper edges in Fig. 4.7 for the coasting beam example. The area between the red triangles (corresponding to the intermediate gradient-error case) is smaller than for the strong gradient-error case. The smallest stop-band width corresponds to the weak gradient-error example depicted with the black dots. Figure 4.7 quantitatively indicates how the half-integer resonance modifies with space charge. The edges of the stop band widen up with increasing space charge and are not parallel to the linear resonance condition for the whole range of intensities. This is observed for all probed gradient-error strengths. The half-integer stop-band width characterization technique fails when there is no space charge. The system becomes isolated, therefore transverse emittances are conserved. When determining the quadrupolar stop band for zero

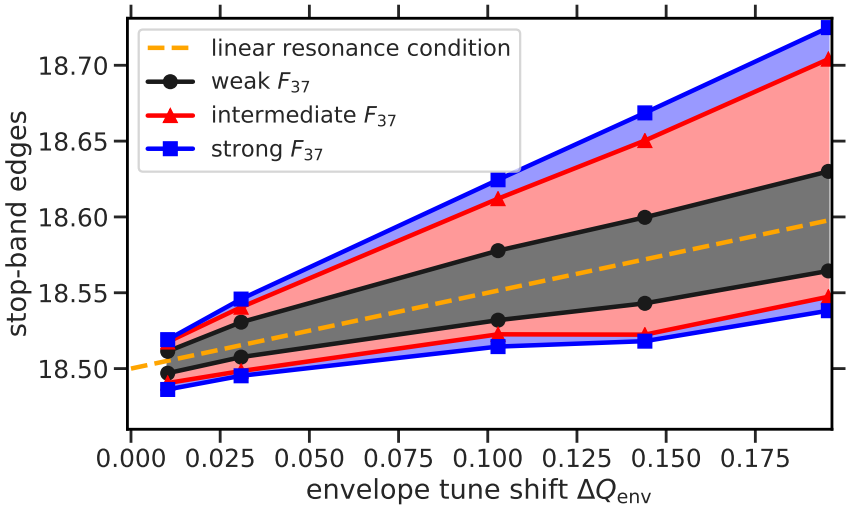

Figure 4.9: Stop-band width for a coasting beam with varying gradient error and space charge. The upper and lower edges of the stop band are indicated by black dots, red triangles, and blue squares for weak, intermediate, and strong greadient-error strengths (see text for details).

intensity, a single-particle approach can be used. In this scenario, the betatron motion of individual particles becomes unstable inside the stop band (demonstrated in Sec. 4.2).

Of more relevance for applications to synchrotrons is the situation for bunched beams. Employing the same stop-band characterization approach, Fig. 4.10 depicts the simulation results. Again, like for coasting beams in Fig. 4.9, the bunched beam stop bands (and the upper edge in particular) widen with increasing space charge for all three gradient-error scenarios. Black dots which are the weak gradient-error example constrain the smallest area. Red triangles and blue squares represent the intermediate and strong gradient-error cases, respectively. In comparison with coasting beams, the lower edge remains the almost same with increasing space charge. Any deviation in the lower edge is negligible compared with the upper edge change. Additionally, there is no significant correlation between the lower edge and the gradient-error strength. Finally, the area occupied by the half-integer resonance expands due to the linear increase of the upper edge. The resonance-free area for coasting beams between 18.5 and the lower edge vanishes for bunched beams. This entails that, in the case of bunched beams, the stop-band width can be

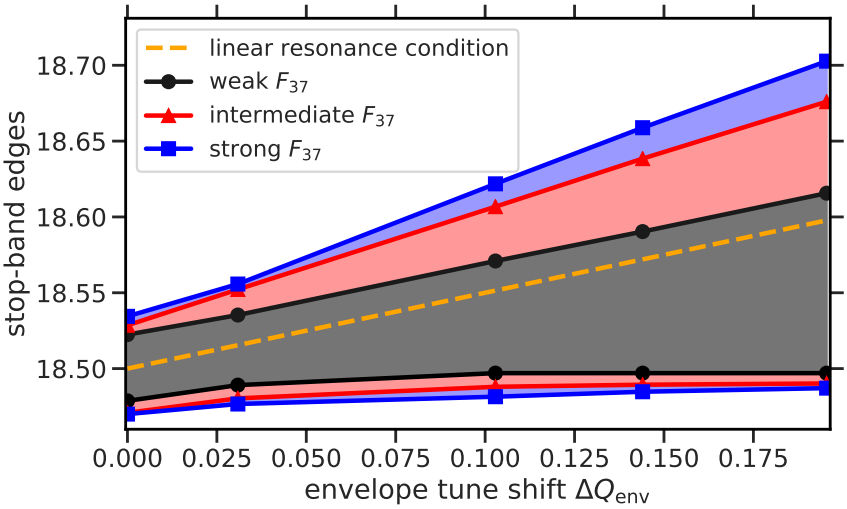

Figure 4.10: Stop-band width for a bunched beam with varying gradient error and space charge. The edges of the stop band are indicated by black dots, red triangles, and blue squares for increasing greadient-error strength (see text for details).

reduced only by moving the upper edge down. In the weak space-charge area where $\Delta Q_{\mathrm{env}} < 0.03$, the detuning from natural chromaticity ($\xi_x = \xi_y = -1.2$) plays a significant role. As a consequence, the stop-band width at zero space charge is increased compared to values in Table 2.1. Space charge dominates in the area with $\Delta Q_{\mathrm{env}} > 0.03$, and the effect of the chromatic detuning becomes negligible.

Figure 4.11 demonstrates how the width of the half-integer resonance shrinks in the region of $\Delta Q_{\mathrm{env}} < 0.03$ after chromatic detuning is suppressed (on the left) using the computer-experiment setup described in 4.1. The right panel demonstrates the same stop-band edges as in Fig. 4.10 for comparison. Practically, in the case of negligible space charge and absent chromatic detuning, the scheme of the half-integer resonance breaks (as in the case of coasting beams in Fig. 4.9) because transverse emittances are conserved in this case. Therefore, to accurately study the impact of chromaticity on the stop-band width a single-particle approach should be used.

Overall, this section has described the methods used in the characterization of the half-integer resonance. The setup of simulations and the stop-band width characterization technique have been described. The technique is designed to adequately

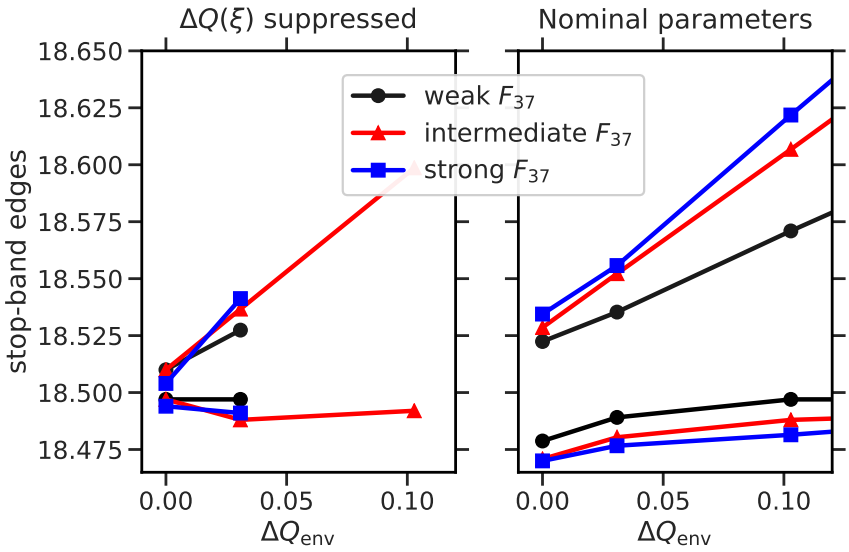

Figure 4.11: Stop-band edges for a bunched beam for increasing space charge (in terms of the envelope tune shift ΔQ_{env}) with varying gradient error (black dots, red triangles, and blue squares — weak, intermediate, and strong respectively). Chromatic detuning of particles $\Delta Q(\xi)$ is suppressed (on the left, see text for details) vs. nominal beam parameters (on the right).

compare simulation results of coasting and bunched beams. Eventually, this technique has been applied to SIS100 yielding ranges of bare tunes affected by the half-integer resonance for various strengths of space charge and gradient error. We have presented how the stop band expands with increasing gradient error and space charge. And together these results provide important insights for such challenges as a space-charge limit in a synchrotron and the lattice optimization which follow in Sec. 4.6 and in Chapter 5 respectively.

4.5 Long-term simulations

The aim of this section is to demonstrate how the synchrotron motion (described in Sec. 2.2) affects the response to the half-integer resonance. Since for the majority of synchrotrons, Q_s lies between 0.01 and 0.001, and $Q_s/Q \ll 1$, we consider up to

2000 turns in this analysis. This corresponds to ≃ 10 synchrotron periods for the nominal SIS100 parameters compared to ≃ one synchrotron period in the short-term simulations above.

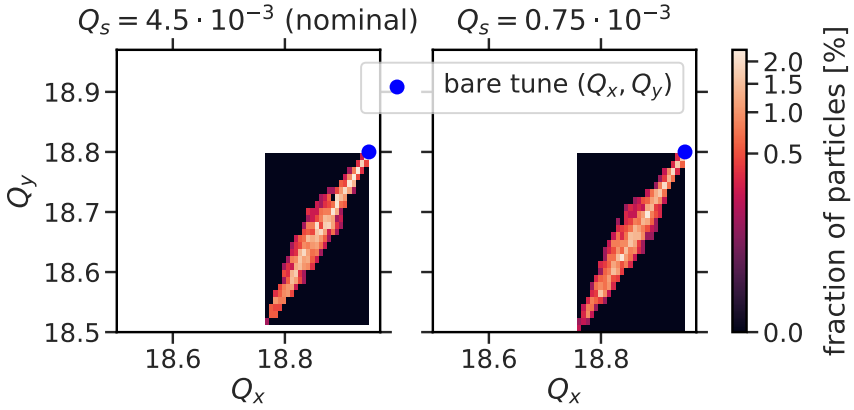

Figure 4.12: Incoherent spread of tunes due to space charge of a Gaussian-like distributed bunched beam before (left) and after (right) the change of the synchrotron tune Q_s (see text for details).

A convenient way to change the synchrotron tune is to vary the RF voltage V (see Eq. (2.30)). In order to keep the space-charge conditions constant while varying the RF voltage V in our computer experiment, bunch length and peak current are fixed. To match the varying RF bucket height, the longitudinal phase space distribution thus varies in RMS momentum spread as

$$\sigma_{\Delta p/p} = \sqrt{\frac{V}{V_0}} \cdot \sigma_{(\Delta p/p),0} \,. \tag{4.11}$$

To remove the effect of chromatic detuning in our computer experiment, the beams are initialized with reduced transverse and longitudinal emittances. To avoid bunch lengthening due to slippage effects and subsequent longitudinal drifting, the transverse emittances are scaled-down along with the longitudinal emittance while maintaining the ratio $I/(\epsilon_x \cdot \epsilon_y)$ for the space-charge tune shift to remain constant. As a result, the space-charge tune shift remains constant for varying Q_s values. For details, see Sec. 4.1.

Figure 4.12 demonstrates that after we decrease the RF voltage to reduce the synchrotron tune Q_s, the total tune-spread of particles remains constant due to the

computer-experiment setup (with the suppression of chromatic detuning). Therefore, when different values of Q_s are probed, space-charge conditions are equivalent.

4.5.1 Long-term dynamics above the resonance

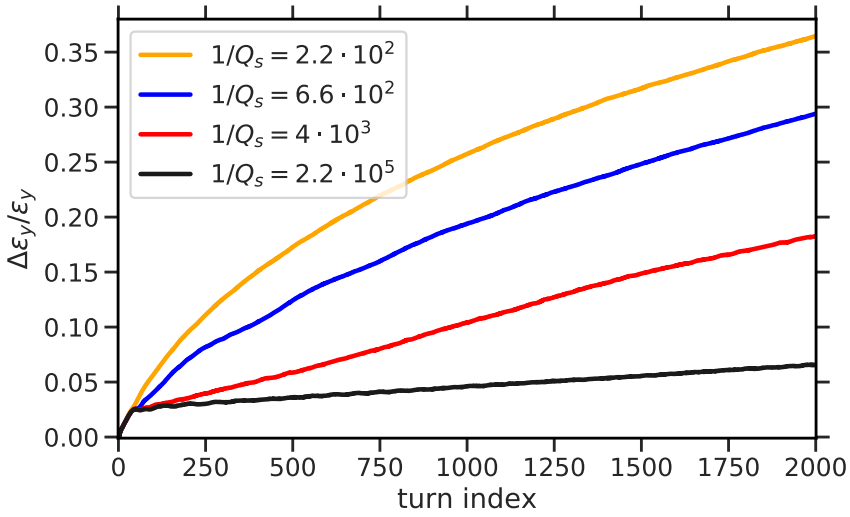

Figure 4.13: Vertical emittance growth of a Gaussian-like distributed bunched beam for various values of Q_s corresponding to the strong gradient-error scenario. The working point $Q_y = 18.62$ is set above the linear resonance condition.

The example working point $Q_y = 18.62$ (same as in Fig. 4.6) serves to investigate the impact of Q_s. Given the strong gradient-error scenario, there is significant emittance growth at this bare tune slightly above the linear resonance condition. Figure 4.13 illustrates the simulation results for various Q_s values.

The black line corresponds to relatively slow longitudinal motion with negligible Q_s. During the first 50 turns, the emittance increases linearly. After this, the speed of the linear growth significantly decreases. The red, blue, and orange lines correspond to increasing values of Q_s. Though the initial linear growth is the same for all of them, the total emittance growth for a given turn at later times, for instance, 10^3, increases with increasing synchrotron tune Q_s. It is interesting to note that, when

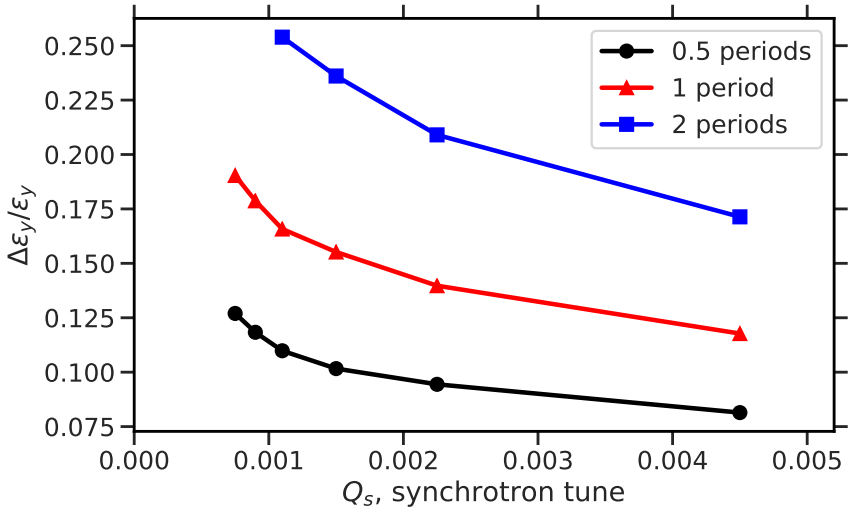

Figure 4.14: Vertical emittance growth of a bunched beam after a few synchrotron periods. The strong gradient error is used, $Q_y = 18.62$.

relating to a given time in terms of synchrotron periods, the emittance growth per synchrotron period *decreases* with increasing Q_s.

Fig. 4.14 demonstrates the results for the different numbers of synchrotron periods with different colors. All curves decrease with the increasing synchrotron tune. This can be easily explained, that for the smaller Q_s the period lasts longer. Therefore, the beam accumulates more of emittance growth. The key message is that the total emittance growth per a synchrotron period is not the same for different values of Q_s.

Another observation from Fig. 4.13 indicates that the fastest growth rate corresponds to the initial short-term regime. After this, the trend is always slower than linear. The total emittance increase (via the quadrupolar resonance mechanism) during the injection plateau at the stop-band edges is, therefore, less than the linearly extrapolated 80% (quoted in Sec. 4.3). Taken together, these results suggest that the developed scheme of the half-integer stop-band characterization in Sec. 4.3 is valid also on long-term time scales: The tunes which are classified as resonance-affected remain inside the stop band, and the total resonantly gained emittance growth is always limited by the threshold.

As indicated previously, in Fig. 4.6 in Sec. 4.3, the emittance growth in bunched beams continues to increase while coasting beams saturate. Figure 4.15 displays

how saturation is lost in bunched beams. In simulation model (see Sec. 4.1 for details), a beam is split on longitudinal slices to provide accurate computations of space charge using PIC.

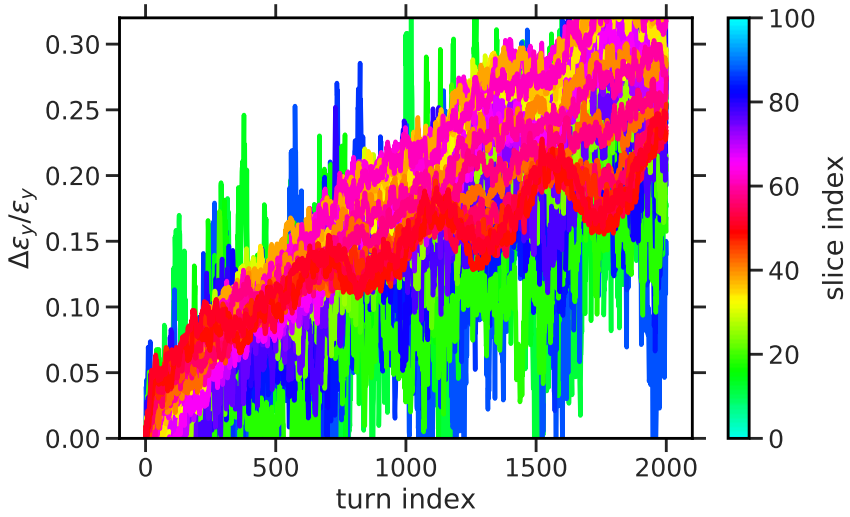

Figure 4.15: Vertical emittance growth corresponding to separate longitudinal slices (color) in a bunched beam. The working point is $Q_y = 18.62$ with the strong gradient-error scenario.

Colors in Fig. 4.15 show how different beam slices contribute to total vertical emittance growth: Shades of red in the beam-center region, blue toward the beam ends. Note, that the number of macro particles per slice corresponds to the normal distribution, consequently head and tail slices have fewer amount of particles which negatively affects the amplitude-ti-noise ratio. First, only red curves show steady linear growth. Then, their slope decreases, whereas magenta and orange curves appear.

Next, we demonstrate it on a shorter time scale in Fig. 4.16 and only for slices grouped in the bunch-center region (left) and the σ_z region (right). The curves show the simulated emittance growth at various synchrotron tunes, where the black color refers to $Q_s = 4.5 \times 10^{-5}$, red to $Q_s = 0.7 \times 10^{-3}$ and blue to $Q_s = 1.1 \times 10^{-3}$. The left panel corresponds to the bunch center region, whereas the right panel depicts the region towards the bunch ends, at a longitudinal position of $z = \sigma_z$. During the first 50 turns, the emittance in the σ_z region remains relatively constant,

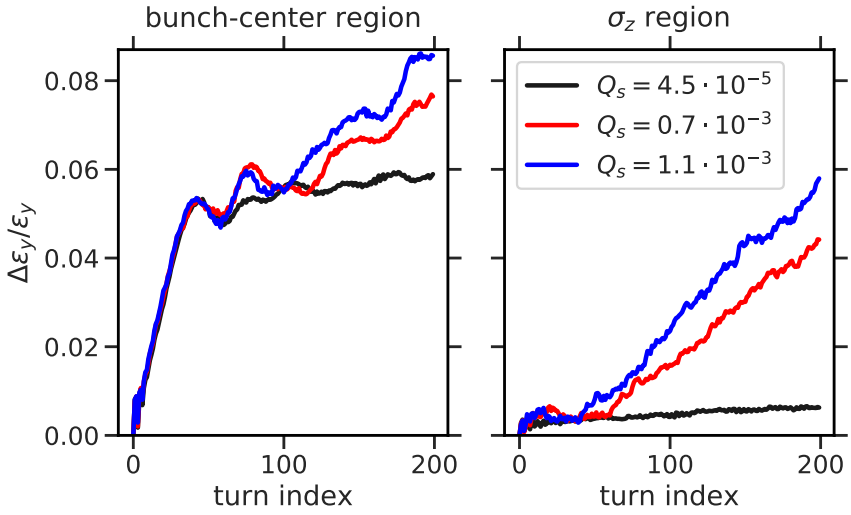

Figure 4.16: Vertical emittance growth corresponding to separate longitudinal areas in the bunched beam for varying values of synchrotron tune. The working point is $Q_y = 18.62$ with the strong gradient-error scenario

whereas the bunch center resonantly reacts to the gradient error. After about 50 turns, a steady linear rise indicates emittance growth in the σ_z region.

The effect of synchrotron motion can be explained as follows: While particles with large amplitudes due to resonance interaction in the bunch center are transported towards the bunch ends, new particles from the bunch ends move towards the bunch center where they continue to interact with the resonance. This overall picture demonstrates the mechanism of interplay between the bunched beam and the half-integer resonance.

4.5.2 Long-term dynamics and the upper edge

It is important to investigate what happens with the residual emittance growth at the upper edge. The computer experiment setup developed above is used. Figure 4.17 shows how the half-integer resonance develops in different longitudinal bunch areas at the bare tune $Q_y = 18.7$ for the strong gradient-error scenario.

Black curves on both panels represent the case of frozen longitudinal motion (longitudinal coordinates (z, dE) of all particles of the distribution remain fixed

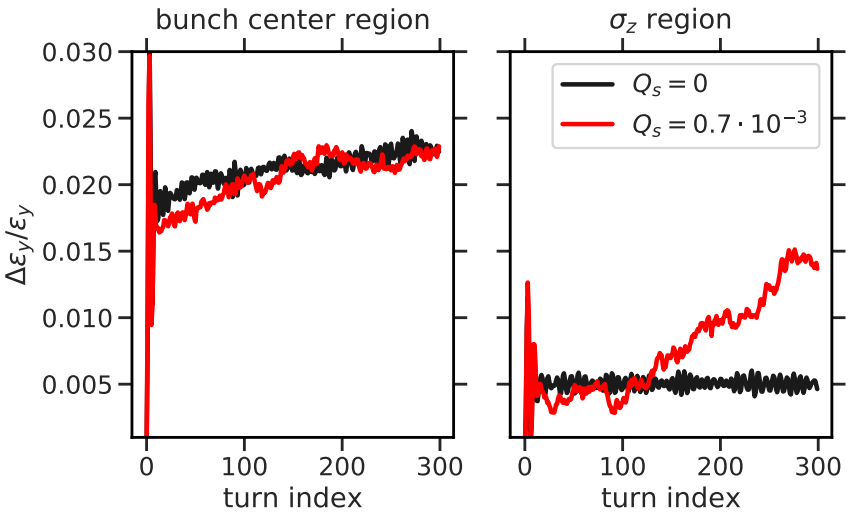

Figure 4.17: Vertical emittance growth corresponding to separate longitudinal areas in the bunched beam for varying values of Q_s. The working point corresponds to the upper edge at $Q_y = 18.7$ for the strong F_{37}.

throughout the simulation), whereas reds curves show the emittance growth in the bunch center and the σ_z region for $Q_s = 0.7 \cdot 10^{-3}$. After the initial mismatch, there is some vertical emittance growth only in the bunch center region on the left. On contrary, σ_z apart from the bunch center (on the right), the vertical emittance remains steady. Though the red curve on the left side almost repeats the black one, on the right side they are different. In the case of finite longitudinal motion, the emittance in the σ_z region fluctuates around its initial value and starts linearly growing after 100 turns. The bunched beam keeps interacting with the half-integer resonance for any $Q_s > 0$ even at the negligible resonance driving term around the upper edge. Particles gain amplitudes in the bunch center and leak towards the tails. Particles from other bunch areas start crossing the bunch center region where they can increase their amplitudes.

Section 4.5.1 shows how the emittance growth continues in the long term. The results are performed on the working point which is close to the linear resonance condition. Figure 4.18 illustrates what happens for different values of the synchrotron tune at the upper edge. The black line represents the frozen longitudinal motion. Besides the initial fluctuations and some initial growth, it remains constant. With

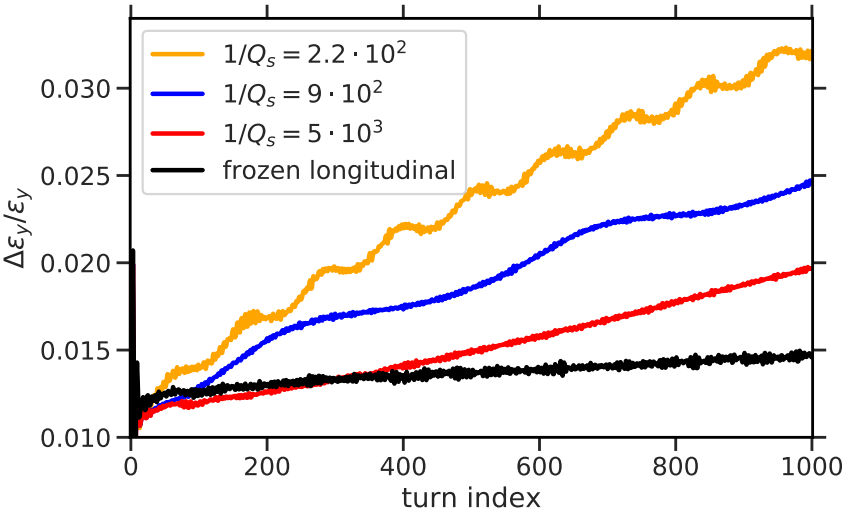

Figure 4.18: Vertical emittance growth from simulations for different values of the synchrotron tune. The working point on $Q_y = 18.7$ corresponds to the upper edge, strong gradient-error scenario.

red, blue, and orange colors we show the emittance growth for the increasing value of Q_s. The curves oscillate on the frequency around $2Q_s$ and increase with the number of turns.

4.6 Space-charge limit

The aim of this section is to identify the space-charge limit, i.e. the maximum tolerable space-charge tune shift for realistic Gaussian-like distributed bunched beams where the area of available bare tunes (not affected by the quadrupolar resonance) reduces to zero. Section 4.4 discusses the influence of space charge and gradient errors on the available area of bare tunes. These two separate influences are discussed here as degrees of freedom based on Fig. 4.19, which depicts the bare tune of the upper edge vs. the strength of space charge.

The classical conceptual discussion of the space-charge limit only relates to the linear resonance condition, see e.g. Refs. [51, 63]: Given a finite but marginal gradient error, the space-charge limit is reached when the linear resonance condi-

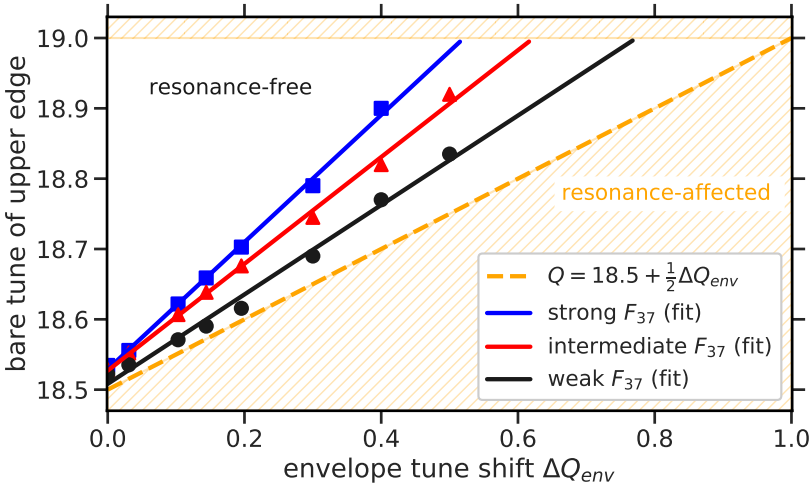

Figure 4.19: Space-charge limit. Blue squares, red triangles, and black dots are the locations of the upper edge corresponding to strong, intermediate, and weak gradient-error scenarios from simulations

tion (shown in dashed orange) reaches the next half-integer (the horizontal line at $Q_y = 19$). Thus, the maximum achievable intensity is determined by the inequality

$$\Delta Q_{\text{env}} < 1 \tag{4.12}$$

on the envelope tune shift. Next, the area below the orange dashed line becomes "forbidden". Therefore, the linear resonance condition sets the constraint on the bare tune Q which shall satisfy the inequality

$$2Q > n + \Delta Q_{\text{env}}\,, \tag{4.13}$$

where $n = 37$ in the SIS100 case.

The focus of this work is on the extension of the quadrupolar resonance from the linear resonance condition towards the stop-band edges for time scales relevant to a synchrotron. As described above, a finite gradient error moves the upper edge higher, leading to a steeper inclination of the curves in Fig. 4.19 represented by blue squares (strong gradient-error scenario), red triangles (intermediate gradient error), and black dots (weak gradient error). Note, that the points at $\Delta Q_{\text{env}} < 0.2$

correspond to the upper edge curves in Fig. 4.10. In order to compute simulation results for $\Delta Q_{\mathrm{env}} > 0.2$, the effect of Montague resonance [90] is avoided by moving to higher horizontal bare tunes. Extrapolation to larger space-charge strengths shows where the upper edge (colored solid lines) reaches the lower edge of the next higher $n+1$ half-integer stop band, i.e. slightly below the horizontal line at $Q_y = 19$. This corresponds to the scenario where adjacent quadrupolar stop bands occupy the entire tune diagram. In our example case, the blue line meets the next resonance at a lower space charge than the red line due to the stronger gradient error.

As it is shown above, a residual gradient error is not expected to result in relatively large emittance growth for coasting beams due to the saturation. Therefore, the space-charge limit is reached at $\Delta Q_{\mathrm{env}} = 1$ (see e.g. Refs. [51, 63]). However, Sec. 4.5 shows how the finite synchrotron motion always leads to significant emittance growth in the long term. Hence, the area below the blue (or red, black) lines in Fig. 4.19 remains "forbidden" in the corresponding case. In other words, working points inside the stop band are not expected to conserve the emittances of bunched beams at finite synchrotron motion and a finite gradient error. This means that accurate estimations of intensity limitations in a synchrotron necessitate simulations with bunched beams. In application to the SIS100 example, the results obtained with Fig. 4.19 are the following. According to the analytical expression in Eq. (4.12), the maximum possible intensity corresponds to $\Delta Q_{\mathrm{env}} = 1$, regardless of the gradient-error strength. On the other hand, linear extrapolation of the simulation results including a certain gradient error indicates a maximum achievable intensity (in terms of ΔQ_{env}). The scenario of strong gradient error results in a limit of only $\Delta Q_{\mathrm{env}} \simeq 0.5$, the intermediate gradient error in $\Delta Q_{\mathrm{env}} \simeq 0.6$, and the weak gradient error in $\Delta Q_{\mathrm{env}} \simeq 0.8$.

To conclude, we find that, for realistic Gaussian-distributed bunched beams, a relatively small stop-band width at zero space charge ($\simeq 10^{-3}$, see Table 2.1) can result in a significant reduction of the maximum intensity (here by a factor 2 for the strong gradient-error scenario). As a consequence, control and compensation of gradient errors are crucial for a synchrotron to maintain the highest intensities under strong space-charge conditions.

5 Half-integer stop-band minimization

So far, this work has focused on the half-integer stop-band width characterization on short and long time scales. The width of the half-integer stop band determines the flexibility of selecting the working point (Q_x, Q_y) as well as the achievable maximum peak current (in terms of space-charge tune shift) in a synchrotron. This chapter discusses how to minimize the stop-band width by correcting the magnet configuration of a synchrotron (lattice). The applied lattice corrections are validated in tracking simulations with space charge. The key results of the chapter are included in Ref. [32] and are published in Ref. [77] by the author.

5.1 Correction schemes

Let us start with the ideal scenario for SIS100 where all quadrupole magnets are superconducting with the same length. Consequently, the absence of gradient errors in the lattice yields the absence of the half-integer resonance. Throughout this work, the corresponding lattice is called the "cold lattice". While replacing the pair of superconducting quadrupoles with the warm quadrupoles (as shown in Fig. 2.7) the lattice of SIS100 features a gradient error. In this case, the lattice is called the "warm lattice".

5.1.1 Parameters for optimization

It is possible to minimize the effect of the half-integer resonance by using several parameters. First, the integral focusing strength of warm quadrupoles can be independently adjusted. Second, a pair of quadrupole corrector magnets located on either side of the perturbing warm quadrupoles is used to entirely suppress the beta-beating outside of the perturbation region [91].

The goal of the optimization is to find the best set of correctors $\vec{k}^*$ minimizing the objective function $f(\vec{k} = n(\vec{\theta}))$, where vector $\vec{\theta}$ is dimensionless, and the transformation $\vec{k} = n(\vec{\theta})$,

$$\vec{k} = \vec{k}_0 + \frac{\sqrt{Q_x^2 + Q_y^2}}{R^2} \cdot N \cdot \vec{\theta}\,, \tag{5.1}$$

normalizes $\vec{\theta}$. Here $\vec{k}_0$ corresponds to the initial settings of quadrupoles (design $k(s)$ for the main families, zero for the corrector magnets), N is a diagonal matrix $N = \{..., 1/N_k, ...\}$, N_k is the number of quadrupoles in the k-th family.

5.1.2 Objective functions

While optimizing a lattice, different objective functions can be used. Conventionally, lattice corrections are performed without intensity effects. However, as shown above, the half-integer stop-band width depends on the strengths of space charge and gradient errors. Therefore, a lattice correction featuring space charge might provide superior settings for the machine operating with space charge. In this work, we consider three different cases for SIS100 at a working point (Q_x, Q_y). The first objective function f_1 corresponds to the conventional case which is the beta-beating accumulated along the ring,

$$f_1 = \sqrt{\frac{1}{C}\oint\left(\frac{\beta(s)-\beta_0(s)}{\beta_0(s)}\right)^2 ds}, \tag{5.2}$$

where $\beta_0(s)$ is the beta-function of the cold lattice, $\beta(s)$ is the beta-function of the warm lattice. The second objective function f_2 is the beating of transverse RMS beam envelopes at non-zero space-charge strength,

$$f_2 = \sqrt{\frac{1}{C}\oint\left(\frac{\sigma(s)-\sigma_0(s)}{\sigma_0(s)}\right)^2 ds}, \tag{5.3}$$

where $\sigma(s)$ and $\sigma_0(s)$ are the transverse beam sizes (including the horizontal dispersion) for warm and cold lattices correspondingly at equal space-charge conditions. Note, that at zero space-charge conditions, $\sigma = \sqrt{\epsilon\beta}$ (in the vertical plane), thus f_2 would lead to identical optimal values to a conventional correction f_1. The last probed objective function is the modification of the second one. The SIS100 lattice consists of six identical sectors (in other words, the *superperiodicity* $S = 6$). Any gradient error breaks this symmetry. Fourier series of the envelope beating results in

$$\frac{\sigma(s)-\sigma_0(s)}{\sigma_0(s)} = \sum_p A_p \exp\left(i \cdot 2\pi \frac{\mu(s)}{Q} p\right), \tag{5.4}$$

where A_p are the complex amplitudes. The beam size of the cold lattice $\sigma_0(s)$ is represented by $p = 6j$ harmonics only, where j is integer. Therefore, to restore the

superperiodicity of SIS100 the third objective function f_3 corresponds to the sum of "non-structural" harmonics (namely, $p \neq 6\,j$) of the envelope beating,

$$f_3 = \sqrt{\frac{1}{C}\oint\left[\sum_p A_p \exp\left(i\cdot 2\pi\,\frac{\mu(s)}{Q}\,p\right)\right]^2 ds\,,\; p \neq 6\,j\,.} \tag{5.5}$$

The gradient error induced by warm quadrupoles leads to both transverse half-integer stop bands. To include horizontal and vertical degrees of freedom all three objective functions are modified,

$$f_i = \sqrt{\frac{f_{x,i}^2 + f_{y,i}^2}{2}}\,, \tag{5.6}$$

where $i = (1,\,2,\,3)$.

In general, there is only one condition in the choice of the objective function. It shall indicate how the quadrupolar resonance modifies for different settings of quadrupole magnets and correctors. The objective functions f_2 and f_3 include transverse RMS beam envelopes. They are numerically computed at nominal SIS100 parameters using full 2D envelope equations [49] with the exact lattice focusing $k(s)$ which includes all gradient errors and settings of correctors (for details see Sec. 3.2).

5.1.3 Numerical implementation and different schemes

Another consequence of changing $k(s)$ is the change of bare tunes. The constraint function $g(\vec{k})$ defined as

$$g(\vec{k}) = \sqrt{\Delta Q_x^2(\vec{k}) + \Delta Q_y^2(\vec{k})} = 0 \tag{5.7}$$

is included in the optimization to prevent the shift of bare tunes. The process described above can be mathematically generalized using the expression

$$\text{Minimize}\left[f(\vec{k} = n(\vec{\theta})),\,\vec{\theta},\,\text{constraints} = g(\vec{k})\right]. \tag{5.8}$$

The numerical implementation is performed in Python with Constrained Optimization By Linear Approximation (COBYLA) [92] which is suitable for functions with an unknown gradient. COBYLA uses only inequalities as constraints. Therefore, a simple numerical trick $g(\vec{k}) \leq 0$ is performed to force COBYLA to keep the bare tunes constant during the optimization.

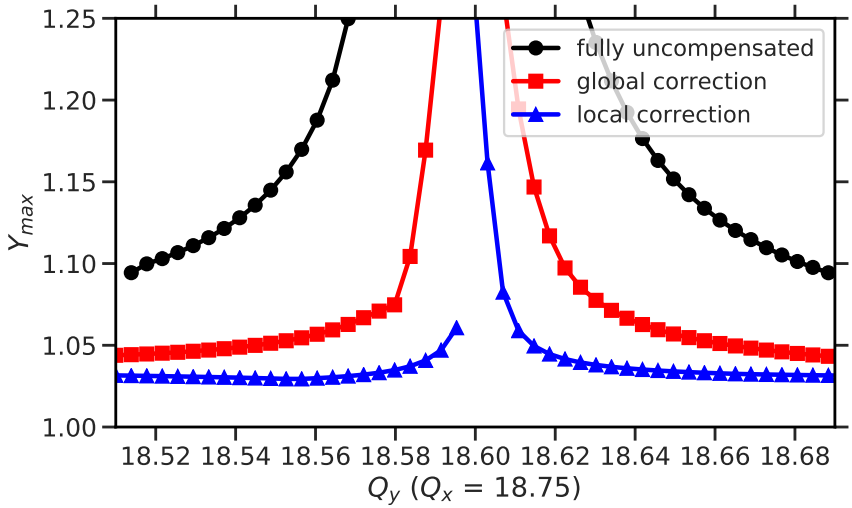

Figure 5.1: Numerical solution of 2D RMS envelope equations at nominal beam parameters vs. the vertical bare tune after compensating the SIS100 lattice with space charge. Black dots, red squares, and blue triangles are the uncompensated scenario, the global correction, and the local correction respectively (see text for details).

First, the global parameters such as the integral focusing strengths of main quadrupole families and of perturbing isolated magnets (*global correction scheme*) are used as optimization parameters. In this case, the normalization matrix is determined by

$$N_{\text{global}} = \begin{pmatrix} 1/84 & 0 & 0 & 0 \\ 0 & 1/84 & 0 & 0 \\ 0 & 0 & 1 & 0 \\ 0 & 0 & 0 & 1 \end{pmatrix}, \tag{5.9}$$

because there are 84 focusing and defocusing quadrupoles. Second, the pair of quadrupole corrector magnets around the isolated perturbation (orange triangles in Fig. 2.7) is added to the optimization to suppress the gradient error locally (*local correction scheme*). Now, the normalization matrix is a 6×6 matrix with $1/N_k = 1$ for both correctors.

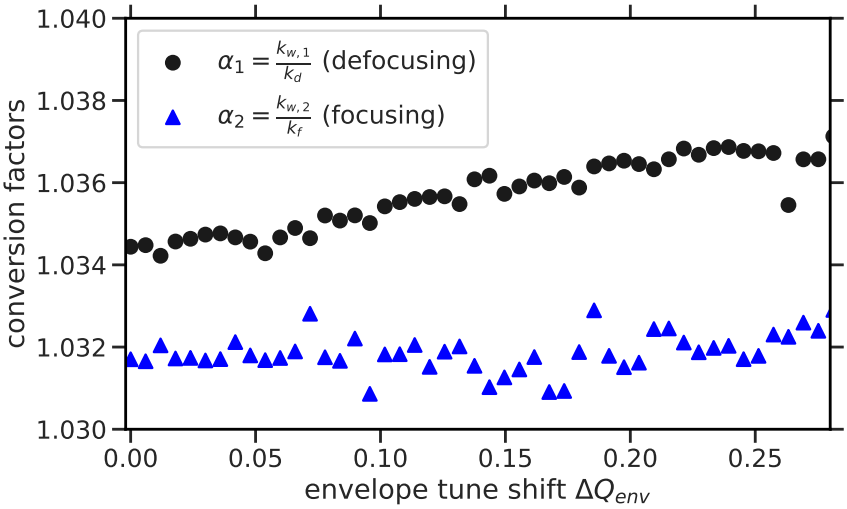

Figure 5.2: Results of numerical optimization for the local correction scheme. Optimal values of the first and the second conversion factors are displayed in black and blue colors (see text for details).

5.1.4 Optimization results

Having discussed how to construct the optimization with space charge, the following presents the results of SIS100 correction schemes.

First, Fig. 5.1 shows the results of the half-integer resonance compensation in terms of matched beam envelopes, where the optimal parameters are found for $\Delta Q_{\text{env}} = 0.2$ with the third objective function f_3. Black dots here indicate the case of the initial gradient-error scenario; red squares and blue triangles represent the response curves after the compensation with global and local schemes respectively. All curves sharply increase around the linear resonance condition at $Q_y = 18.6$, and the stop-band decreases when more correctors are included in the optimization, namely, in the case of the local correction scheme.

Next, we proceed with the results of the local correction scheme since it performs the best results. Figure 5.2 and Fig. 5.3 show how the optimal values change for increasing space charge. Black dots correspond to the conversion factor α_1 between the integral strengths of the first warm quadrupole $k_{w,1}$ and a cold defocusing quadrupole, whereas blue triangles represent the conversion factor α_2 between the integral strengths of the second warm quadrupole $k_{w,2}$ and a cold focusing

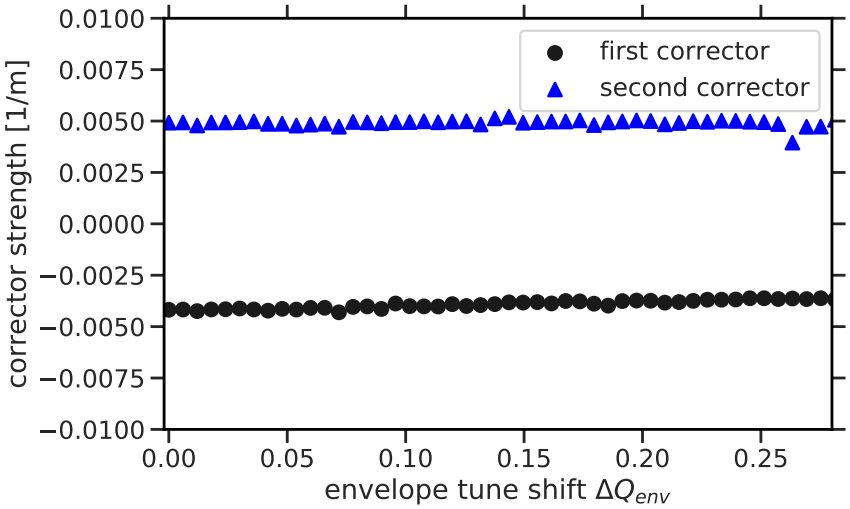

Figure 5.3: Results of numerical optimization for the local correction scheme against space charge. Optimal values of the integral strength of the first and the second correctors are displayed in black and blue colors.

quadrupole. Although black dots slightly increase for higher values of the envelope tune shift and blue triangles fluctuate around $\alpha_2 = 1.032$, these deviations of optimal parameters are negligible (demonstrated below).

Then, in Fig. 5.3 black dots and blue triangles correspond to the obtained values at both correctors adjusting to the warm-quadrupole perturbation region. In this case, optimal values are constant with the change of space charge.

Figure 5.4 shows the comparison between optimal values obtained using f_2 with and without space charge for the second adjacent corrector magnet as an example. Black dots correspond to optimal values obtained at zero space charge ($\Delta Q_{\text{env}} = 0$), whereas the red triangles are achieved at the SIS100 nominal beam parameters ($\Delta Q_{\text{env}} = 0.2$). Besides some small fluctuations, both curves repeat each other. All magnets used in the optimization show similar behavior. An important observation is that the optimal lattice configuration obtained without space charge is at the same time also the optimum configuration when including space charge for practical synchrotron applications.

It is important to emphasize that the optimization results for all three objective functions converge to the same values (with small fluctuations). The reason for this

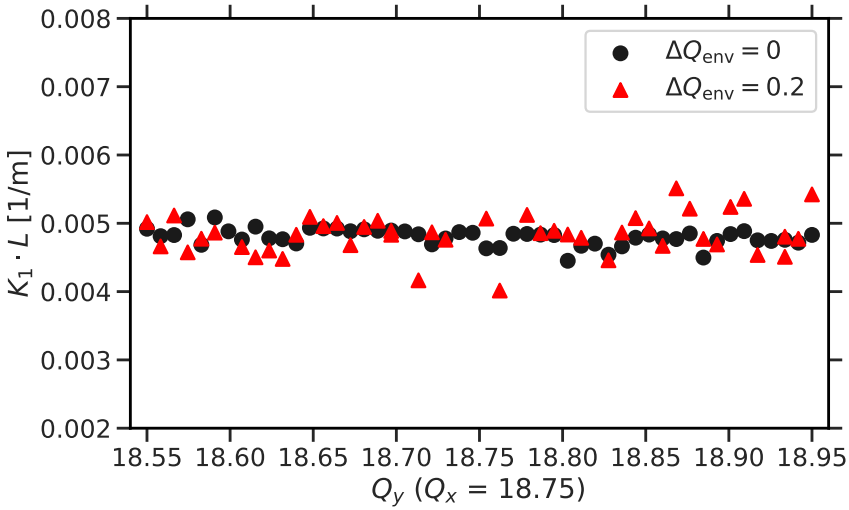

Figure 5.4: The optimal settings of the second corrector magnet, which are obtained with nominal space charge (red triangles) and without space charge (black dots) vs. the vertical bare tune.

is as follows. In the smooth focusing approximation, the beating of transverse beam envelopes is represented by the sum of resonance harmonics (see Eq. (3.19)),

$$\delta(\phi) = \frac{Q_y}{2} \cdot \sum_p \frac{F_p \cos(p\,\phi)}{Q_y^2 - Q_y\, C\, \Delta Q_{\mathrm{KV}} - (\frac{p}{2})^2}\,, \tag{5.10}$$

where the strongest contribution of the envelope beating corresponds to the harmonic $p = n \simeq 2Q$

$$\delta \propto \frac{F_n}{|2Q_y - \Delta Q_{\mathrm{env}} - n|} \tag{5.11}$$

regardless of space charge. Therefore, f_1 and f_2 provide similar results of the optimization. Moreover, the minimization of f_2 and f_3 achieves the same optimum because COBYLA suppresses only the main harmonic ($p = n$) since the others are irrelevant. The fluctuations of obtained results often appear due to the increase of

$$\frac{F_0}{2Q_y - \Delta Q_{\mathrm{env}}} \tag{5.12}$$

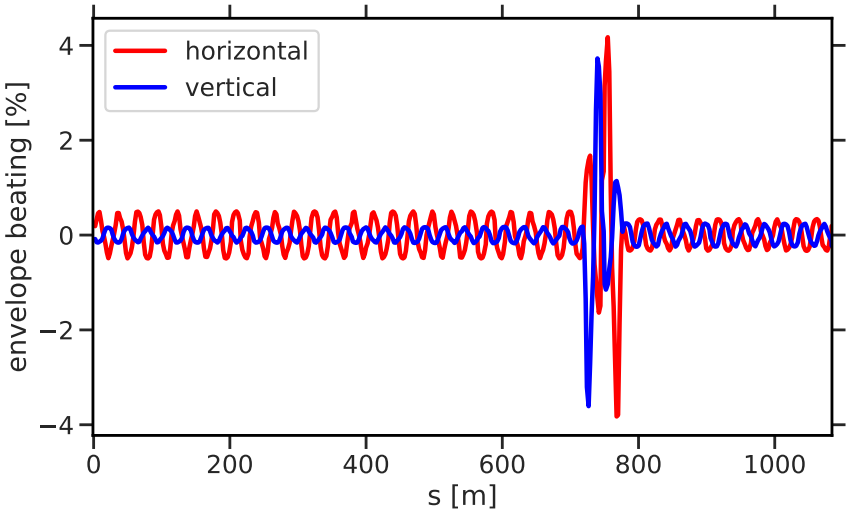

Figure 5.5: Beating of the horizontal (red) and vertical (blue) RMS beam envelopes along the SIS100 lattice with space charge (nominal SIS100 beam) after the lattice compensation with the local correction scheme.

the zero harmonic $p = 0$, which might result in significant fluctuations of optimal values in synchrotrons with relatively small bare tunes. To avoid this, F_0 should be set to zero.

5.1.5 Lattice functions after optimization

It is important to validate that the optimization procedure does not modify lattice functions in an inadequate way. We start with the envelope beating shown in Fig. 5.5, where settings of the lattice are obtained using the local correction scheme.

Red and blue curves correspond to the horizontal and vertical RMS beam envelopes obtained numerically while solving Eq (3.12). Although in the warm-quadrupole perturbation region the beating of transverse envelopes increases up to 4%, the total (integrated over the ring) beating is $\simeq 1\%$. Also, the 6-fold symmetry of the SIS100 lattice is not restored.

Next, the dispersion function modifies when the settings of the lattice are varied, which can be illustrated using Eq. (2.8). Using the solver described in Sec. 3.2, the

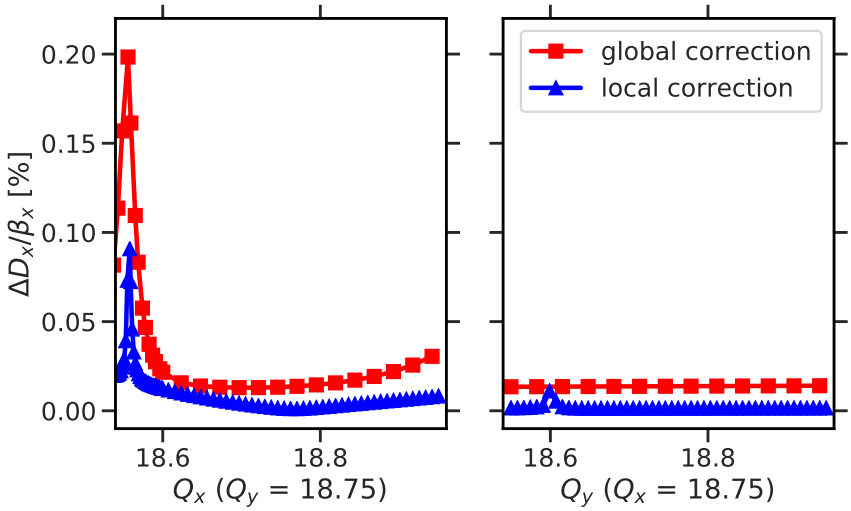

Figure 5.6: Beating of the horizontal dispersion with space charge (nominal SIS100 beam) vs the horizontal bare tune (left) and the vertical bare tune (right). Red squares and blue triangles correspond to the lattice settings obtained with the global and local correction schemes. Dispersion is normalized to the horizontal beta-function.

dispersion affected by gradient errors and space charge can be numerically computed. The value

$$\sigma_D = \sqrt{\frac{1}{C}\oint\left(\frac{D(s)-D_0(s)}{\beta_x(s)}\right)^2 ds}\,, \tag{5.13}$$

is the total dispersion beating, where $D(s)$ is the dispersion function after optimization and $D_0(s)$ is the dispersion of the cold lattice, both computed with space charge. Figure 5.6 demonstrates the change of the total dispersion beating against the horizontal and vertical bare tunes.

For both lattice settings, the dispersion beating increases around the linear resonance condition (distinctively on the left, vs the horizontal tune). However, taking into account that $\sigma_{\Delta p/p} = 0.45\cdot10^{-3}$, this effect has a negligible impact on the total transverse beam sizes (especially outside of the half-integer stop band).

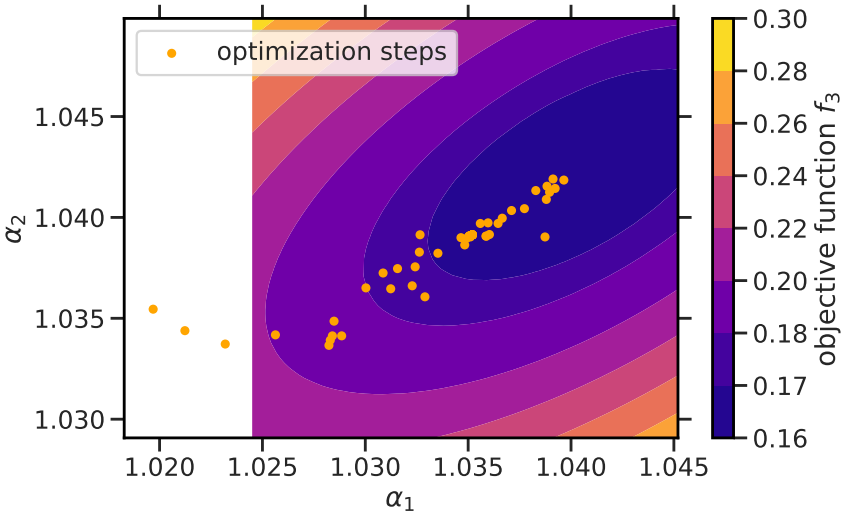

Figure 5.7: Objective function f_3 (color) with respect to the change of conversion factors α_1 and α_2 (see text for details). Orange dots show how the optimization converges in the local minimum.

5.1.6 Sensitivity and convergence studies

It is now necessary to demonstrate that the numerical implementation of correction schemes described above converges to a local (global if possible) minimum. Here we use the example case of the global correction scheme with the objective function f_3 defined in Eq. (5.5). This problem is parameterized in 2D and consequently is demonstrated in Fig. 5.7.

Colors represent different levels of the objective function, the dark blue area corresponds to the local minimum. Starting, for example, at $\alpha_1 = 1.02$ and $\alpha_2 = 1.036$, the optimization steps of COBYLA converge in the dark blue area. Therefore, the implementation is valid. Next, Fig. 5.8 shows how the total beta-beating changes if the lattice settings are varied in the vicinity of their optimal values.

With red dashed and black dotted lines we indicate the location of the optimal configuration of the cold quadrupole magnets (defocusing and focusing families respectively). Red dots and black triangles correspond to the change of the total beta-beating in the synchrotron (also the objective function f_1 defined in Eq. (5.2)).

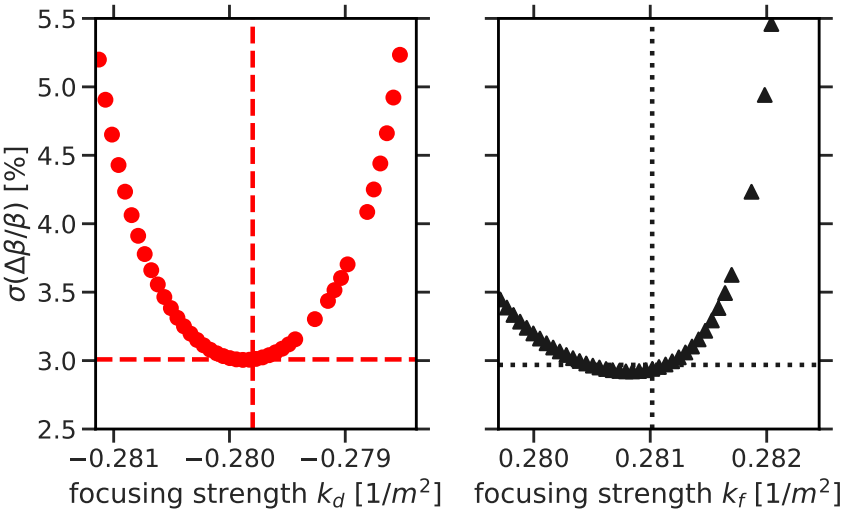

Figure 5.8: The standard deviation of the beta-beating across the SIS100 lattice for varying settings of two families of quadrupole magnets, defocusing (red dots, dashed lines for the optimal value) and focusing (black triangles, dotted lines for the optimal value).

In both cases, the curvature is pseudo-parabolic with the minimum located around the optimal values.

5.2 Verification in simulations

The following proceeds to demonstrate that the optimal parameters of the lattice (obtained above) using 2D RMS envelope equations (equivalent to a coasting KV beam) provide smaller emittance growth in particle simulations with Gaussian-like distributed beams.

The objective functions (especially f_2 and f_3) are valid for KV coasting beams. It is possible to test in simulations whether this applies to more realistic transverse beam distributions. Figure 5.9 illustrates the results of particle tracking of a coasting beam. Different colors indicate the lattice settings used in simulations, namely, black dots represent the scenario of the uncompensated SIS100 lattice, red squares and blue triangles correspond to the global and local correction scheme settings. As discussed above (in Sec. 4.3), due to the saturation of transverse emittance growth,

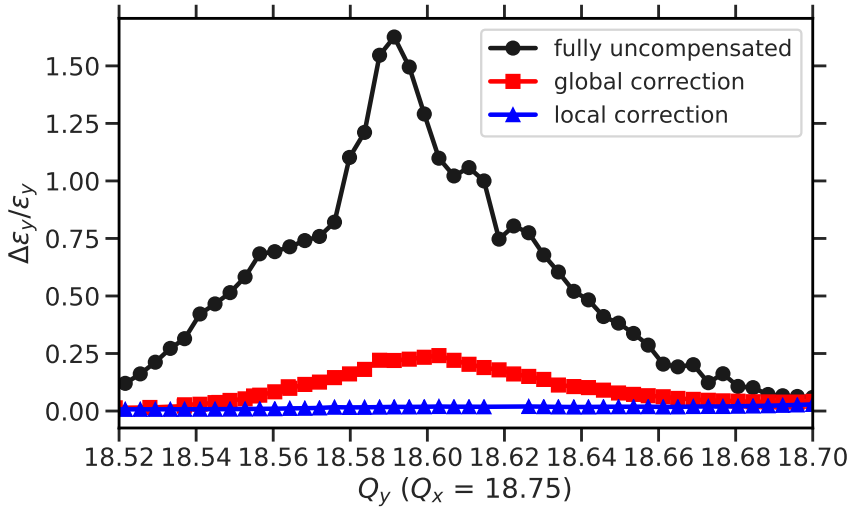

Figure 5.9: Vertical emittance growth of a Gaussian-like distributed coasting beam vs. the vertical bare tune after optimizing the SIS100 lattice (at nominal parameters). Black dots, red squares, and blue triangles correspond to SIS100 settings obtained without any compensation, with global, and local correction schemes

200 turns is enough to characterize the half-integer stop band for coasting beams. As expected, the local correction scheme provides the settings where transverse emittance growth is the smallest.

Bunched beams are of relevance for all synchrotrons. Moreover, SIS100 is planned to operate with bunched beams. Therefore, the simulations with Gaussian-like distributed bunched beams are scrutinized here. Figure 5.10 illustrates the transverse emittance growth after 200 turns (in short term).

Similarly to Fig. 5.1 we show with black dots the initial perturbation, red squares indicate the results of the *global correction scheme*, and the blue triangles represent the *local correction scheme*. The optimization provided for coasting KV beams is also valid for realistic Gaussian-like distributed bunched beams.

The optimum configuration yields a stop-band minimization in both transverse planes as demonstrated in Fig. 5.11.

The panels depict simulated emittance growth as a function of both transverse tunes for nominal bunched beam conditions during one synchrotron period. The left panel shows the simulation results without compensation and the right panel

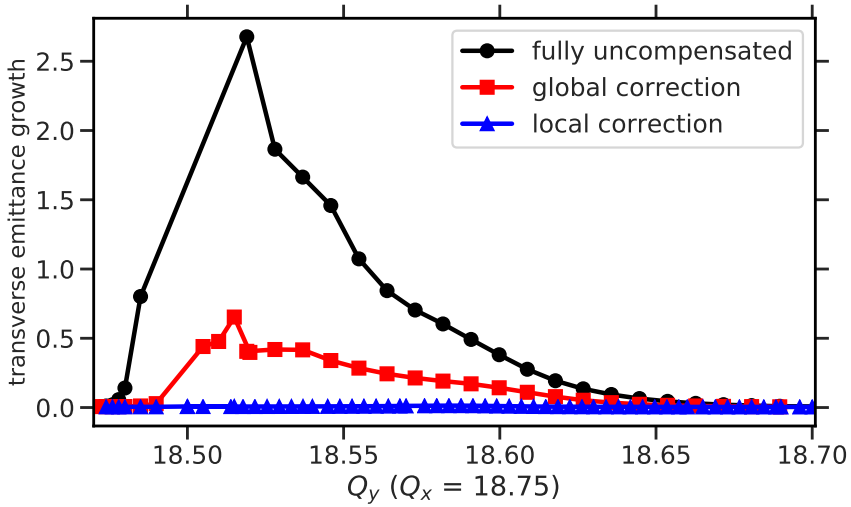

Figure 5.10: Transverse emittance growth of a Gaussian-like distributed bunched beam vs. the vertical bare tune after optimizing the SIS100 lattice.

with optimal compensation. The color scale ranges from yellow for tunes affected by the resonance to dark blue for resonance-free tunes. This graph shows that the applied correction effectively suppresses the effects of the half-integer resonance in both directions for one synchrotron period. This entails more freedom in choosing the working point or, alternatively, higher achievable bunch intensity.

As shown in Sec. 4.5 emittance growth can cease only in the case of coasting beams or at negligible values of the synchrotron tune. Therefore, we perform a set of simulations at nominal beam parameters for more than 10 synchrotron periods to test the optimal settings on long-term time scales. Figure 5.12 provides the summary for these simulations.

Starting with the black dots representing results after four synchrotron periods, we note that the half-integer resonance is still leading to emittance growth. The red squares and blue triangles correspond to increasing numbers of turns. All the response curves sharply increase below $Q_y = 18.5$, have the peak around $Q_y = 18.6$, and then drop down. The highest value in the plot corresponds to 10% of emittance growth after 13 synchrotron periods. This shows again (like in Sec. 4.5), that finite but small gradient errors with space charge lead to finite emittance growth. Despite this, the overall inflicted emittance growth inside the stopband is suppressed compared to the non-compensated scenario. For example, without the correction,

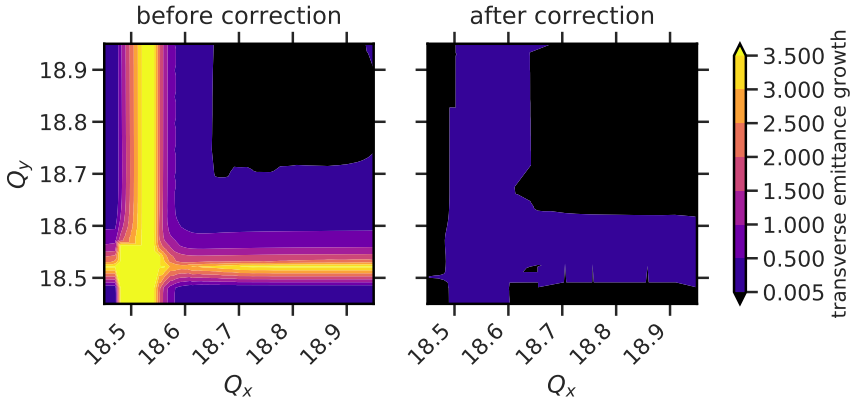

Figure 5.11: Verification of the half-integer stop-band minimization in terms of transverse emittance growth (color) of a bunched beam for nominal beam parameters, before corrections on the left, after applying the local correction scheme on the right (see text for details).

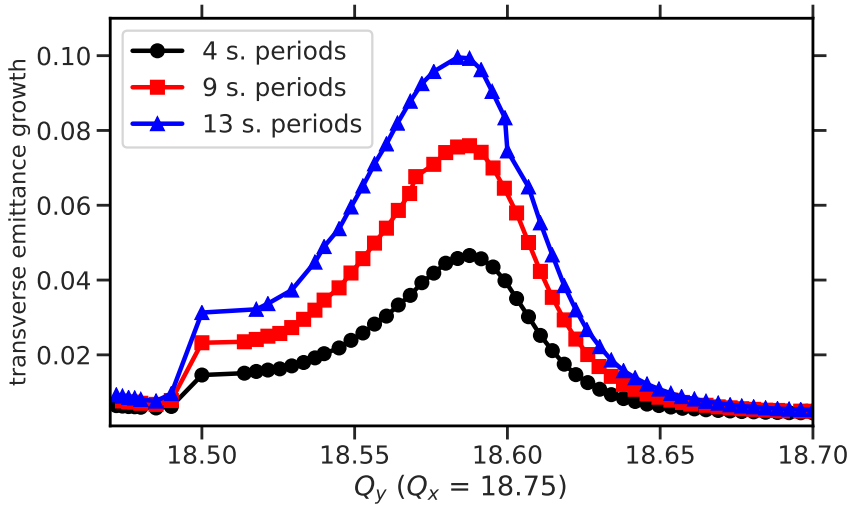

Figure 5.12: Long-term transverse emittance growth (4, 9, and 13 synchrotron periods shown as black dots, red squares, and blue triangles) for nominal SIS100 beam parameters of a bunched beam after applying the local correction scheme (see text for details).

more than 10% of emittance growth is gained during one synchrotron period at any bare tune inside the $18.5 < Q_y < 18.6$ region, whereas now, after the lattice correction, the beam has the same amount of the total emittance increase only around the linear resonance condition after 13 synchrotron periods.

This section has reviewed the three key aspects of stop-band minimization. First, the parameters for the lattice correction have been shown. Second, we have applied the optimal values in simulations and presented their performance. Finally, the validation in long-term simulations has been carried out. Though the half-integer resonance is not suppressed entirely, the overall emittance growth across the tune diagram is strongly reduced after the lattice correction.

6 Measurements: SIS18 studies

Throughout this work, all simulation results correspond to the example case of SIS100 which is currently under construction. As support for the findings above, the following chapter describes experimental studies in SIS18 at GSI. Both hadron synchrotrons have a similar design with $\gamma_r \gtrsim 1$ where space charge plays a significant role.

Figure 6.1 demonstrates the SIS18 lattice which consists of 12 identical sectors. Black squares correspond to the dipole (bending) magnets, blue circles represent focusing and defocusing quadrupole magnets. To compensate the gradient error accumulated across the ring a pair of quadrupole corrector magnets (red triangles) can be used. The horizontal bare tune $Q_x = 4.32$, and the vertical bare tune is placed above $Q_y = 3.5$ to study the 7/2 half-integer resonance.

In general, the strength of two quadrupole corrector magnets can be independently adjusted. However, throughout the experiment, both correctors are powered with the same strength albeit with the opposite sign. Such configuration is a quadrupole *corrector loop*. The design beta function is identical in both locations. Therefore, the bare tunes of SIS18 stay constant for any value of the corrector loop strength, whereas the stop-band integral at zero intensity (described in Sec. 2) F_7 changes. The energy of the $^{40}Ar^{10+}$ bunched beam used in the experiment corresponds to 8.6 MeV/u[1]. In this experiment, chromaticity is set to zero via sextupole magnets. For details, see Table 6.1 and Refs. [13, 14].

[1] Nominal injection energy in SIS18 is 11.4 MeV/u, it was reduced during the experiment via UNILAC

Table 6.1: Beam and machine parameters during the experiment in SIS18

Parameter	Value
Revolution frequency	186.04 kHz
Beam type	bunched
Intensity	$3 \cdot 10^9 \leq N \leq 1.2 \cdot 10^{10}$
Energy (injection)	8.6 MeV/u
RMS emittances	(13.5, 6.1) mm mrad

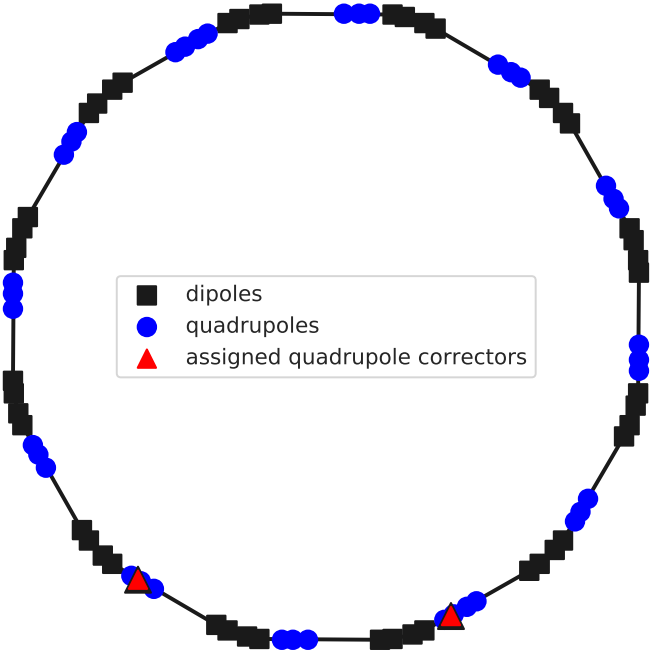

Figure 6.1: Layout of the SIS18 lattice: bending magnets (black squares), quadrupoles (blue dots), and quadrupole corrector magnets which are used in the experiment (red triangles).

6.1 Upper edge from particle losses

The following experimental setup (also referred to as the dynamic tune scan) allows to determine the upper edge of the half-integer (7/2) resonance in SIS18 for various intensities and settings of the machine.

While keeping all the parameters of the machine constant, the vertical bare tune descends toward the half-integer 3.5 during $\simeq 0.1$ s. The red curve in Fig. 6.2 corresponds to the variation of Q_y. Vertical lines (blue dashed, black dotted, and orange

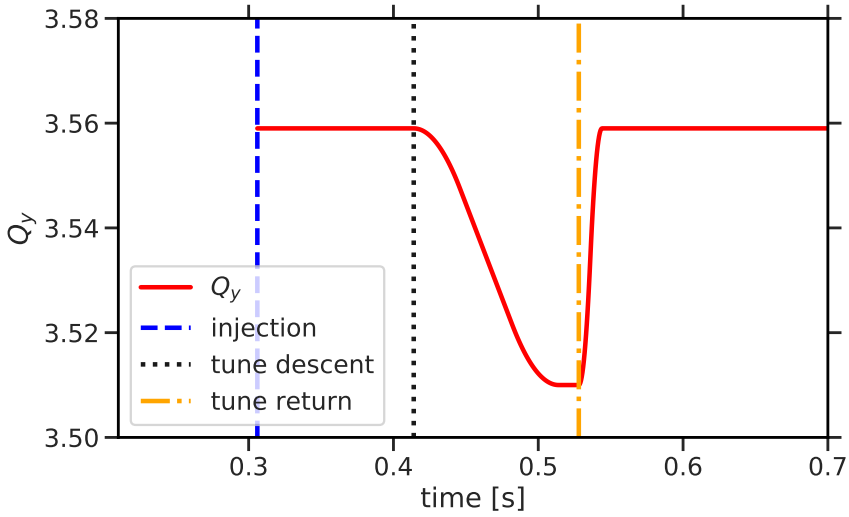

Figure 6.2: The part of the SIS18 cycle relevant for the experiment (corresponds to the dynamic tune scan). The red curve and vertical lines show the change of the vertical bare tune (set value in the machine) and timings of the SIS18 cycle.

dot-dash) indicate the timings of the SIS18 cycle[2]: the injection from UNILAC to SIS18, the start of Q_y descent, and the tune return correspondingly. When the vertical bare tune intersects the half-integer stop band, particle losses occur. This effect can be measured using a Direct-Current Current Transformer (DCCT), for example, like in Fig. 6.3. First, the number of particles (solid red) reaches the maximum after the injection (dashed blue). Second, there is some particle loss between the dashed blue and dotted black lines associated with the injection mismatch and the bunching. Third, during the tune descent, the red curve declines sharply after the bare tune reaches the upper edge of the half-integer stop band.

In order to determine the location of the upper edge, the loss rate $\frac{1}{N}\frac{dN}{dt}$ can be used, where the change of the number of particles N is normalized by the maximum amount of particles (after the injection). Negative loss rates are shown with black and red curves in Fig. 6.4 for two values of the strength of the corrector loop.

Both curves start above the half-integer stop band (on the right), stay constant until the bare tune reaches the upper edge (dashed vertical lines), and rapidly ascent

[2] Cycle of a synchrotron is the set of all beam processes from the injection to the extraction.

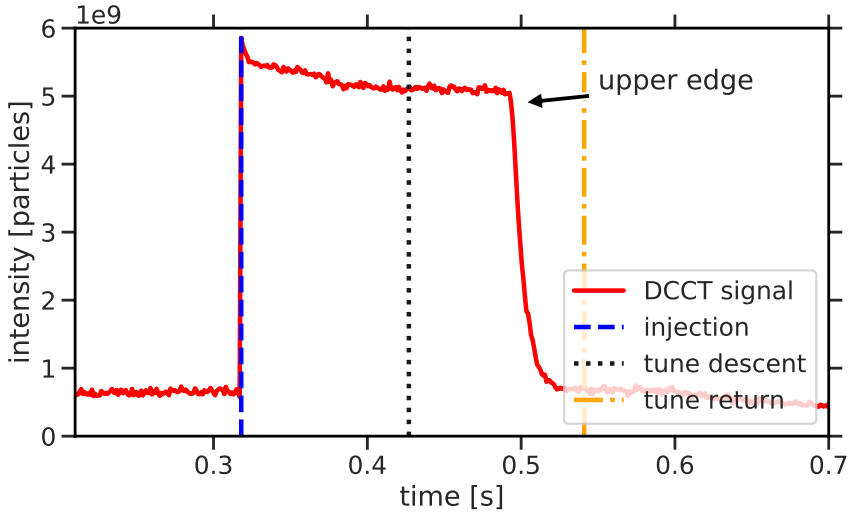

Figure 6.3: Beam intensity as the number of particles (red curve) during the SIS18 cycle, vertical lines determine the locations of beam processes of the SIS18 cycle.

afterward. The beam experiences significant particle losses inside the stop band. In the case of the red line, the upper edge is reached earlier. Therefore, this configuration (represented by the red line) corresponds to the scenario with a stronger gradient error compared to the black curve.

As indicated above, the change of the strength of the corrector loop yields the variation of the stop band while the bare tunes are constant. The scenario when the distance between the upper edge and the half-integer is minimal corresponds to the optimal configuration of the machine. Figure 6.5 summarizes this one-dimensional challenge. Black dots and red squares represent the location of the upper edge against the strength of the corrector loop for two probed intensities. Both intensities correspond to $\Delta Q^{y}_{\mathrm{KV}} \simeq 0.01$. Here, the error bars indicate only the precision of the bare tune measurements (discussed in detail in Sec. 6.3), no systematic error associated with the timings of the SIS18 cycle is included. To find the optimal value of the strength of the corrector loop the interpolation by the upper branch of the hyperbola,

$$\mathrm{fit}(c_1, c_2, \kappa^*) = \sqrt{c_1 + c_2 \cdot (\kappa - \kappa^*)^2}\,, \tag{6.1}$$

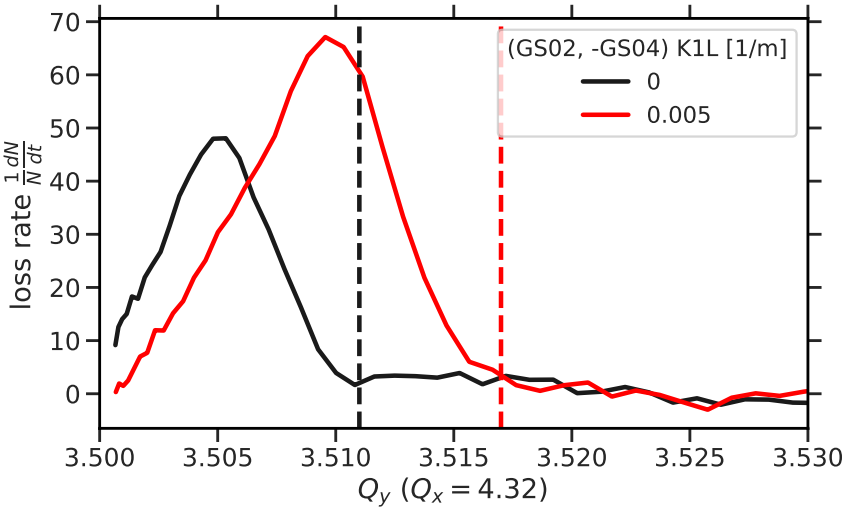

Figure 6.4: Example of how to get the upper edge from the dynamic tune scan. Black and red solid lines correspond to the change of the loss-rate function for two values of the corrector-loop strength. Dashed lines indicate the locations of the upper edges.

is performed (black and red curves, the very right points are excluded), where c_1 and c_2 are free parameters, κ is the corrector-loop strength with the optimal value κ^*. Both curves have similar behavior with the minimum approximately at -0.005 m^{-1}. The upper edge is systematically higher in the case of $N = 1.1 \cdot 10^{10}$. Although the upper edge linearly increases with space charge (as shown in Sec. 4.4), the situation demonstrated here can also be explained by the following. In this setup, the intensity is reduced via the change of the chopper[3] time window, and the initial transverse beam sizes are larger in the red case. Any change of the vertical bare tune toward the half-integer leads to the increase of the vertical beam size (local beta-function increase discussed in Sec. 2). Therefore, halo particles start leaving the vacuum chamber at higher tunes.

[3] A special device which removes halo particles of the beam

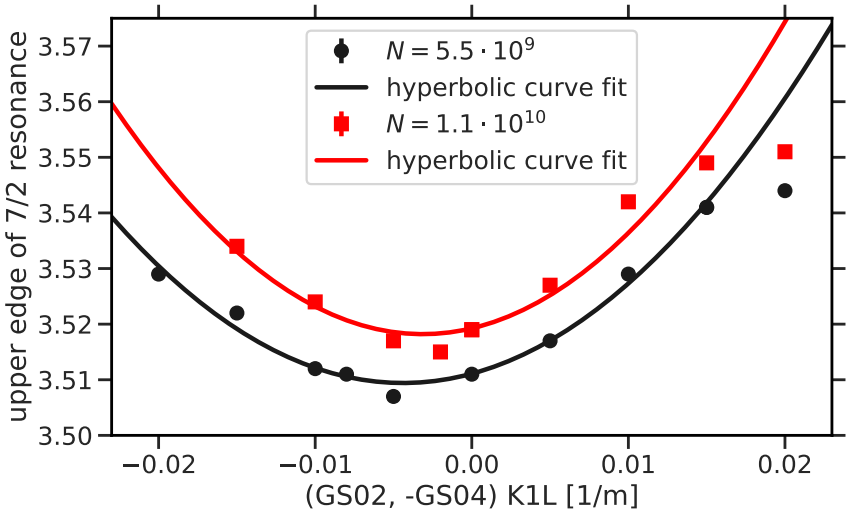

Figure 6.5: Results of the half-integer stop-band minimization in SIS18. Black dots and red squares indicate the locations of the upper edge of the 7/2 resonance in SIS18 for various values of the corrector-loop strength. Solid lines correspond to the fit by a hyperbolic function (see text for details).

6.2 Half-integer stop band and beam size measurements

In order to separate the effects leading to the particle losses, the second experimental setup (a static tune scan) is used. In this setup, the change of Q_y (shown in Fig. 6.6 with the red curve) lasts $\simeq 0.016$ s. Next, it stays at a lower point on a so-called "tune plateau" for $\simeq 0.1$ s (here, the probed tune $Q_y = 3.51$). Finally, Q_y returns to the initial location. Unlike in the case of the dynamic tune scan, the stop-band characterization via beam size measurements requires several SIS18 cycles for probing different values of the vertical bare tune. This is done because the ion beam has to be substituted by a new one after the tune plateau. Otherwise, space-charge conditions change for different probed Q_y (due to particle losses and increase in beam sizes).

First, in this setup, the growth of the vertical beam size at a probed Q_y is measured. Second, to characterize the half-integer stop band (similarly to the technique in Sec. 4.3) $\Delta\sigma/\sigma$ in the vicinity of $Q_y = 3.5$ are compared. Such measurements are usually performed in hadron machines using Ionization Profile Monitors (IPM) [93].

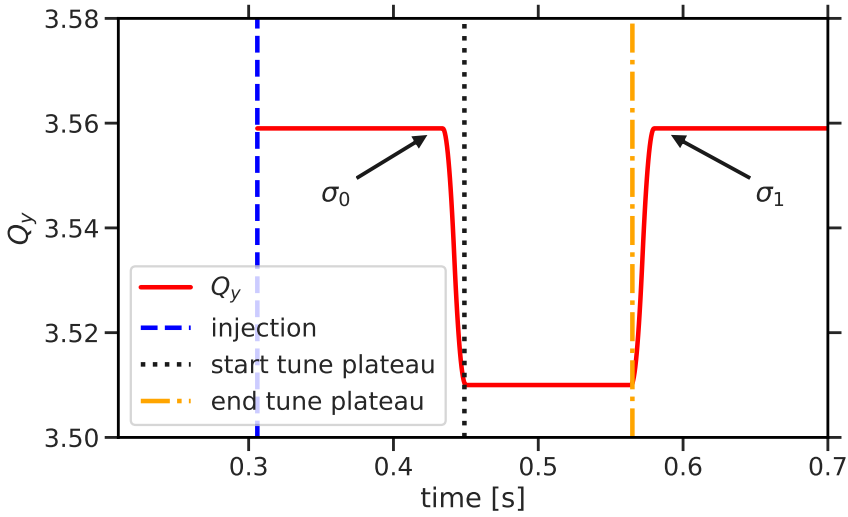

Figure 6.6: The part of the SIS18 cycle relevant for the experiment (corresponds to the static tune scan). Red curve and vertical lines are the change of the vertical bare tune (set value in the machine) and the timings of beam processes. Arrows indicate where the values of the vertical beam size σ_0 and σ_1 are recorded.

This device consists of a micro-channel plate and a wire array (64 wires in this setup) behind the plate. When a beam passes through the IPM it ionizes the residual gas inside the vacuum chamber. Due to a transverse electric field, the ionized gas moves towards the micro-channel plate. Next, residual gas ions hit the plate which emits electrons in the direction of the wire array. The accumulated charge on wires corresponds to the readout signal.

The example of the beam size measurements during the static tune scan is illustrated in Fig. 6.7. Black dots and red squares represent wire signals before and after the tune plateau correspondingly. Transverse beam profiles are assumed to be Gaussian-like. Therefore, the vertical beam size can be computed via the fit with the function,

$$\text{signal} = \frac{A \cdot N}{k_\sigma} \exp\left[-\frac{(k-k_0)^2}{k_\sigma^2}\right] + C\,, \tag{6.2}$$

where k_σ is the vertical beam width (counted in the number of wires), N is the number of particles in the ion beam, parameters A, k_0, and C are the amplitude,

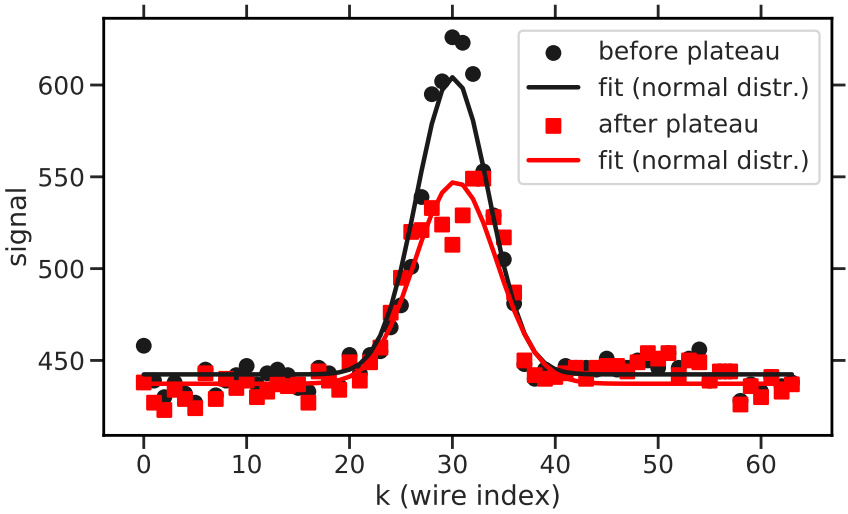

Figure 6.7: Vertical beam profiles as wire signals of the IPM (black dots and red squares) before and after the tune plateau respectively (see text for details) of the static tune scan. Solid curves show the fit by the normal distribution function.

the mean value, and the constant shift respectively. The total amplitude of the signal is proportional to the number of particles in the beam. Such manipulation allows to take into account the change of the peak current associated with beam losses. The distance between wires in the array is $2 \cdot 10^{-3}$ m. Therefore, the vertical beam size is simply $\sigma_y = k_\sigma \cdot 2 \cdot 10^{-3}$ m. The sensitivity of the micro-channel plate behind the central wires ($k \simeq 30$) is deficient at relatively small intensities of the ion beam [94]. As a result, after the losses on the tune plateau, signals on the central wires ($k = 29, 30, 31$) are expected to be imprecise (three central red squares). Consequently, they are excluded from the analysis.

We define vertical beam-size growth as

$$\Delta\sigma/\sigma = (\sigma_0 - \sigma_1)/\sigma_0\,, \tag{6.3}$$

as the value accumulated during the tune plateau, where σ_0 is measured before the tune descent, and σ_1 after the tune ascent. Alternatively, σ_0 and σ_1 can be measured at the start and at the end of the tune plateau[4]. We define beam-size growth

[4] The transverse beam profile measurement lasts around 0.01 s.

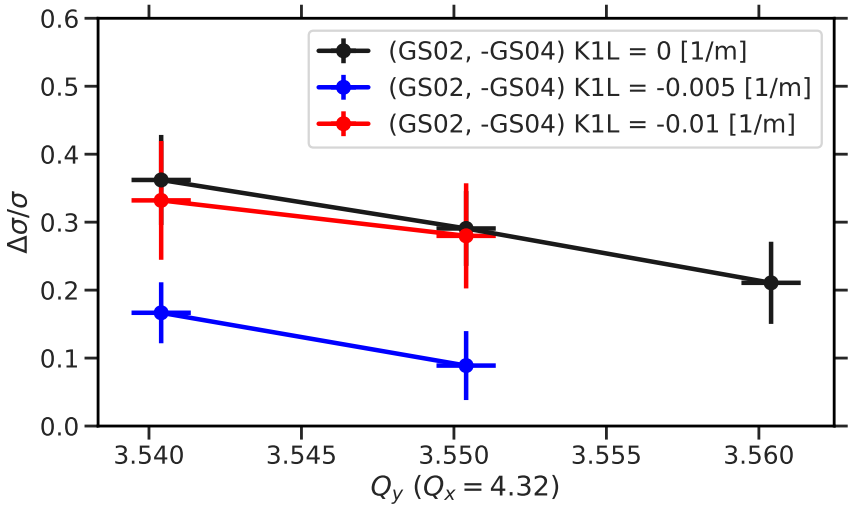

Figure 6.8: Results of beam size measurements, $\Delta Q_{\mathrm{KV}}^{y} = 0.011$. Black, red, and blue dots show the change of the vertical beam size for three different values of the corrector-loop strength against the vertical bare tune.

in this way to exclude the influence of lattice functions (local values of the beta-function, for example) because σ_0 and σ_1 are measured at the same vertical tune and lattice functions. Ideally, turn-by-turn IPM measurements throughout the tune plateau can mimic the emittance-growth technique defined in Sec. 4.3. However, this setup is not available in SIS18.

First, we demonstrate in Fig. 6.8 that the optimum value of the corrector-loop strength found in Sec. 6.1 entails a smaller half-integer stop-band width and, consequently, smaller transverse-beam-size growth. For equivalent conditions at injection (the number of particles and transverse beam sizes yielding $\Delta Q_{\mathrm{KV}}^{y} = 0.011$), the strength of the corrector loop is changed from zero to negative values. As shown above, $\kappa^* \simeq -0.005$, which results here in the reduction of vertical beam size growth with a factor of two approximately.

Next, Fig. 6.9 demonstrates the response of the vertical beam size growth to the vertical bare tune Q_y for various values of space charge (due to the intensity variation in UNILAC).

Black dots, red upward triangles, blue squares, and orange downward triangles correspond to the values of vertical-beam-size growth $\Delta\sigma/\sigma$ obtained with increasing space charge. Similar to the technique described in Sec. 4.3, a threshold deter-

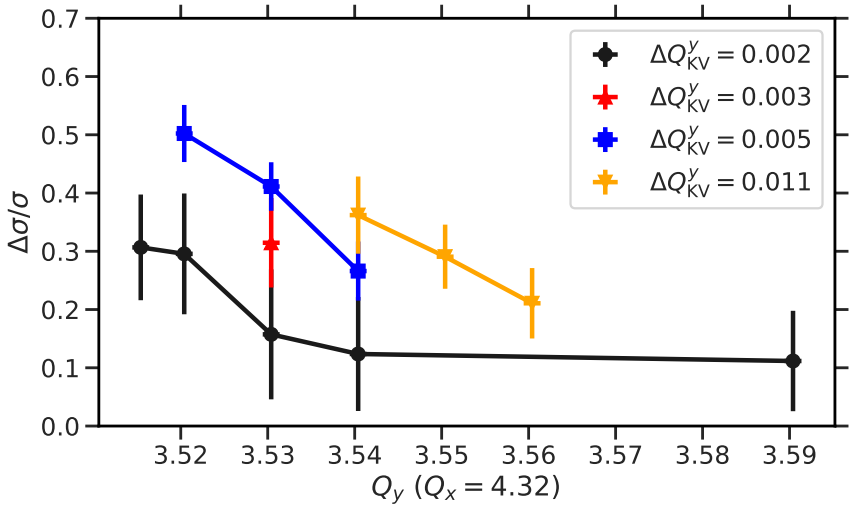

Figure 6.9: Results of beam size measurements, the strength of the corrector loop is zero. Black dots, red upward triangles, blue squares, and orange upward triangles show the change of the vertical beam size for increasing space charge against the vertical bare tune.

mines the location of the upper edge. However, more data points for different Q_y (for all probed intensities) are required to acquire a desirable resolution.

6.3 Calibration of betatron tunes

Gradient errors randomly distributed across the SIS18 lattice results in a betatron tune shift (F_0, see Sec. 2.3). Therefore, the actual values of the vertical bare tunes in the machine alter from the values set by the control system ($Q_{x,\mathrm{set}}$, $Q_{y,\mathrm{set}}$). In order to avoid a systematic error in the stop-band characterization, bare tunes are calibrated.

6.3.1 Beam Position Monitor

To measure the transverse offset of a beam at the location s_0 in a synchrotron, a Beam Position Monitor (BPM) can be used. This device consists of two pairs of

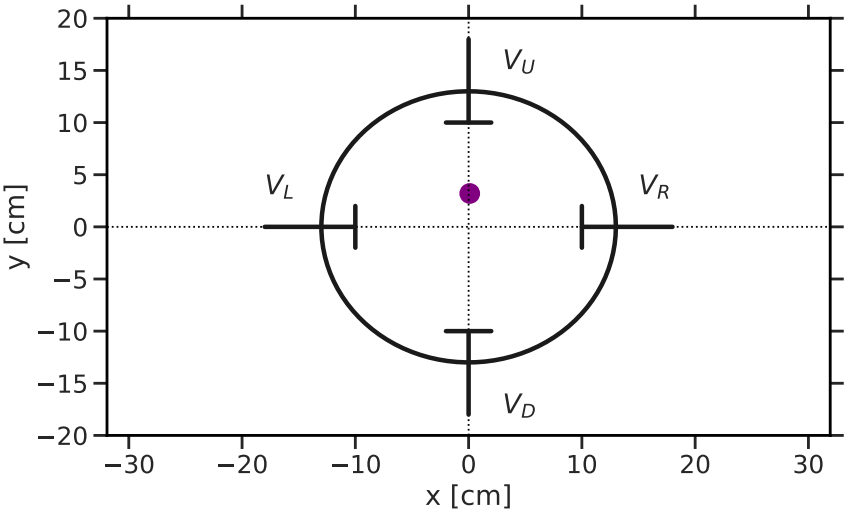

Figure 6.10: Schematic example of a Beam Position Monitor. The beam with a transverse offset is the purple circle.

parallel plates. When a beam passes through the BPM, image charges are induced on each plate and consequently integrated as readout signals V_L, V_R, V_U, V_D.

Let us consider a beam with a relatively large vertical offset as shown in Fig. 6.10. Then, $V_U - V_D > 0$, and $V_R \simeq V_L$. Thus, the horizontal offset,

$$\langle x \rangle = M_x \frac{V_R - V_L}{V_R + V_L}, \tag{6.4}$$

and the vertical beam offset,

$$\langle y \rangle = M_y \frac{V_U - V_D}{V_U + V_D}, \tag{6.5}$$

are reconstructed using a linear approximation, where M_x and M_y are calibration constants. Here, $\langle \cdot \rangle$ is the averaging over a beam distribution, which indicates that a BPM in this setup records a dipolar signal.

In SIS18, 12 BPMs [95] are used for closed-orbit control and correction. Also, horizontal and vertical bare tunes Q_x and Q_y can be measured using BPMs. First, an external excitation in the vertical plane provides coherent dipolar oscillations

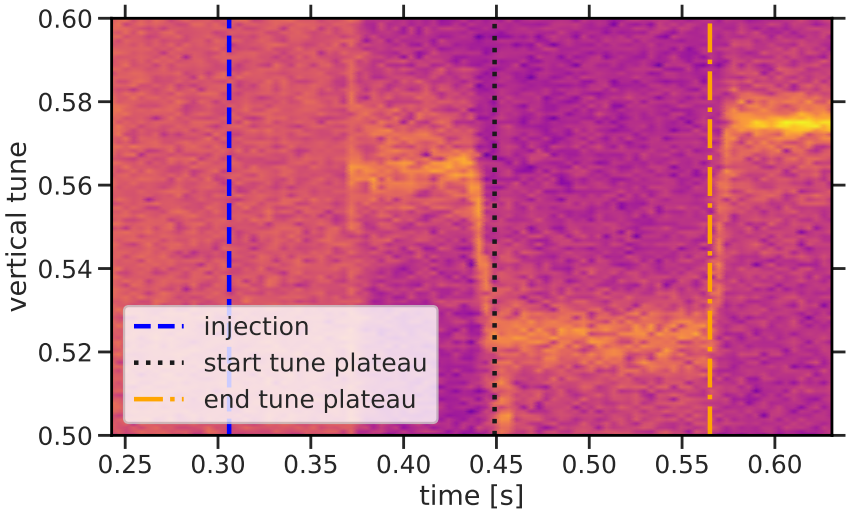

Figure 6.11: Example of vertical bare tune measurements using a BPM. Vertical lines indicate the timings of the SIS18 cycle. The yellow color shows the location of the vertical bare tune in SIS18 throughout the experiment.

of the beam. Then, a BPM records the vertical beam offset each turn which is approximately

$$\langle y \rangle(k) = A_0 \cos(2\pi Q_y k + \phi_0), \tag{6.6}$$

where k is the turn index, constants A_0, ϕ_0 depend on the excitation strength and the location of the BPM. This approximation is valid when the motion in the transverse plane is decoupled, and the intensity is relatively small to avoid decoherence effects [96]. Also, A_0 should be large enough to increase the signal-to-noise ratio, albeit it should be relatively small to prevent nonlinearities.

The maximum of Fourier spectrum of such a signal corresponds to the fractional part of the vertical bare tune. The spectrum can be computed using Fast Fourier Transform (FFT). The precision of the tune measurements scales with the number of turns K in the recording as $2/K$ [97]. As a result, the change of the vertical bare tune throughout the synchrotron cycle (for example, shown in Fig. 6.6) can be monitored using BPMs.

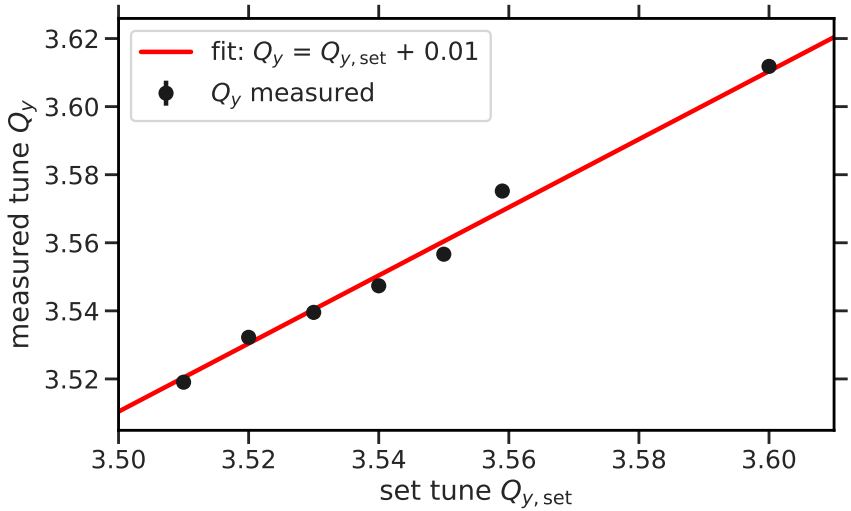

Figure 6.12: Results of the vertical betatron tune calibration in SIS18. Black points are measured using SIS18 BPMs, and a linear fit (red line) is used to find the offset between the set value and the actual vertical bare tune in the machine (see text for details).

6.3.2 Measurements of betatron tunes

Figure 6.11 depicts the change of Q_y during the static tune scan for the probed vertical tune $Q_y = 3.51$. First, the injected beam (at 0.3 s, the blue dashed line) is coasting. In this regime of turn-by-turn recording, BPMs operate only with bunched beams. Therefore, the signal appears only after the bunching. Also, as mentioned above, only the fractional part of the tune can be reconstructed.

Figure 6.12 displays the measurement results for all probed values of Q_y. Measured points are shown with black dots. The linear interpolation (the red solid line) defines a simple calibration procedure,

$$Q_y = Q_{y,\mathrm{set}} + 0.01\,, \tag{6.7}$$

in the SIS18 synchrotron.

Next, it is important to validate that the shift of the horizontal and vertical bare tunes $\Delta Q(\kappa) = -\frac{F_0}{2}$ does not break the procedure of finding the optimal value of the corrector-loop strength κ. This tune shift amounts to

$$\Delta Q(\kappa) \propto \kappa\,(\beta(s_1)\cos(2\pi\mu(s_1)\cdot 0) - \beta(s_2)\cos(2\pi\mu(s_2)\cdot 0))\,, \tag{6.8}$$

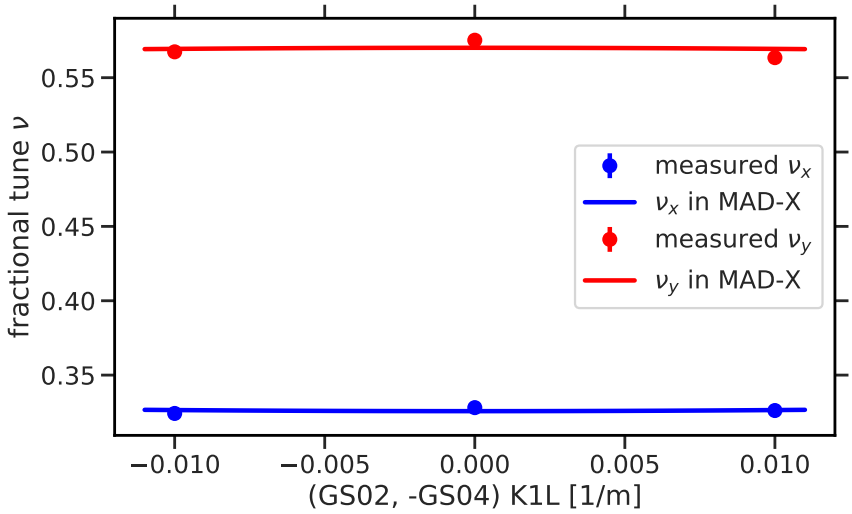

Figure 6.13: Change of horizontal (blue) and vertical (red) bare tunes for three different strengths of the corrector loop. Solid lines are computed in MAD-X.

where s_1 and s_2 are the locations of quadrupole corrector magnets in the SIS18 lattice. In the model, these magnets have equivalent beta-functions, whereas due to randomly distributed gradient errors in the SIS18, $\beta(s_1) \simeq \beta(s_2)$.

Figure 6.13 demonstrates the change of the bare tunes $\Delta Q_{x,y}(\kappa)$ with the change of the corrector-loop strength. Blue and red points in Fig. 6.13 are measured horizontal and vertical bare tunes in the SIS18 synchrotron when solid lines correspond to the change of bare tunes in the numerical model.

Applying $\kappa = \pm 0.01$ shifts the vertical bare tune Q_y (red dots) *downwards* on the level of $\lesssim 0.01$. On contrary, the location of the upper edge moves *upwards* at the same and increasing values of $|\kappa|$ according to Fig. 6.5. The shift of the upper edge of the vertical stop band amounts to $\gtrsim 0.015$, and $\Delta Q(\kappa)$ becomes relevant at $|\kappa| > 0.011$ increasing the error of the fitting by the function expressed in Eq. (6.1). However, at moderate values of $|\kappa|$ the fit is acceptable. Therefore, we recommend to accurately calibrate either the corrector-loop setup (including the ratio of $\beta(s_1)/\beta(s_2)$) or the location of the upper edge using the BPM measurements.

6.4 Results of the experiment

In this chapter, we demonstrate how to characterize the half-integer stop band using experimental data. Two approaches (dynamic and static tune scan) are proposed and applied. Although the static tune scan allows to accurately characterize the half-integer stop band, the dynamic one is more suitable for lattice optimization. First, the dynamic tune scan requires only one cycle, and hence it is more time-efficient. Second, the optimal settings of a synchrotron insignificantly deviate with space charge (discussed in detail in Chapter 5). Nevertheless, for the accurate estimation of the space charge limit, only the static tune scan can be used.

The SIS18 lattice is optimized using the corrector loop setup. Although the distance between the upper edge and the half-integer decreases only on ≤ 0.01 (between the optimum and zero) at space charge corresponding to $\Delta Q^{y}_{\mathrm{KV}} \simeq 0.01$, this correction can play a vital role at the FAIR intensities (discussed in Sec 4.6). Therefore, a dedicated experiment is required to estimate the space-charge limit in SIS18 using the static tune scan.

Conclusions and Outlook

This study characterizes the half-integer stop band for coasting and bunched beams in hadron synchrotrons. The quantitative framework for the characterization is based on 2D and 3D simulation models with self-consistent space charge and is tested in a dedicated experiment in SIS18. Throughout this work, heavy-ion synchrotrons SIS18 and SIS100 at GSI and FAIR complexes serve as example cases, but the findings can be applied to other hadron synchrotrons. In this study, the relevant stop-band widths are compared for varying gradient errors and space-charge strengths.

As one of the main findings, the stop-band characterization provides insights for choosing working points free of half-integer resonance impact. Coasting beam simulations establish the connection to existing analytical studies, for example, Refs. [47, 49]. While the lower and upper edges of the stop band for KV coasting beams are known to run parallel to the linear resonance condition, the stop-band width for Gaussian-distributed coasting beams is found to widen with increasing space charge. In this case, the upper edge of the half-integer stop-band width linearly increases with space charge and gradient errors with a stronger slope than the linear resonance condition determined in Ref. [49], which depends only on space charge.

For bunched beams, simulations over several synchrotron periods in Sec. 4.5 confirm that the stop-band characterization remains valid on longer time scales, relevant for realistic synchrotron operation. Periodic synchrotron motion is shown to result in continuous emittance growth.

In SIS100, choosing a working point outside the identified stop band ensures that the bunched beam is subject to an emittance growth below the chosen threshold during the injection plateau (here 80% over one second). Further, the influence of the synchrotron tune is investigated, with smaller Q_s reducing the total emittance growth for a given instant of time. As a key application, we determine the intensity limit given by the half-integer stop band. We show that the correction of the half-integer resonance increases the intensity limit. The improvement is verified in long-term simulations. We demonstrate how, using experimental data, the stop-band characterization can be implemented to optimize the lattice and estimate the space-charge limit.

The simulation study for Gaussian bunches over long-term time scales (several synchrotron oscillation periods) resulted in several new insights of practical relevance to existing and future synchrotrons. First, unlike in the case of coasting

beams, the resonance-free area between the bare half-integer tune and the lower stop-band edge vanishes. Second, even a relatively small gradient error (resulting in a zero-space-charge stop-band width of just $\simeq 10^{-3}$) can considerably reduce the maximally achievable bunch intensity (in the SIS100 example by a factor $\simeq 2$). We note that this effect, whilst absent in classical discussions of the space-charge limit, must be taken into account under realistic synchrotron operation conditions. Third, the reduction of the half-integer stop band via lattice correction, computed without space charge, is found to also be optimal under finite space charge conditions. Therefore, conventional lattice correction tools are well suited to increase the gradient-error-induced space-charge limit of a synchrotron.

Future work can address the following aspects. While for simplified beam distributions, the upper stop-band edge is known to run parallel to the linear resonance condition for increasing space charge, we found a steeper and more limiting slope for realistic distributions. The nature of the emittance-growth mechanism at the upper edge is, therefore, an intriguing question to be explored further. At this point, also the impact of chromatic detuning should be scrutinized as a secondary effect on the extension of the upper stop-band edge. Additionally, a natural progression of the present study is to accurately determine the space-charge limit in SIS18 due to the half-integer resonance using experimental data.

Lists

List of Acronyms

LHC Large Hadron Collider

CERN Organisation Européenne pour la Recherche Nucléaire

RF Radio Frequency

FAIR Facility for Antiproton and Ion Research

GSI Gesellschaft für Schwerionenforschung

NUSTAR Nuclear Structure Astrophysics and Reactions

CBM Compressed Baryonic Matter

PANDA Anti-Proton ANnihilation at DArmstadt

APPA Atomic, Plasma Physics and Application

UNILAC UNIversal Linear Accelerator

PIC Particle In Cell

RMS Root Mean Square

MAD-X Methodical Accelerator Design

KV Kapchinsky-Vladimirsky

COBYLA Constrained Optimization By Linear Approximation

DCCT Direct-Current Current Transformer

IPM Ionization Profile Monitor

BPM Beam Position Monitor

FFT Fast Fourier Transform

List of Symbols

β_r	Particle velocity normalized to the speed of light
γ_r	Lorentz factor $\frac{1}{\sqrt{1-\beta_r^2}}$
x, y, z	Cartesian coordinates
t	Time
s	Path length, $s = \beta_r\, t$
$\Delta p/p$	Momentum offset
B_0	Guide magnetic field
C	Synchrotron circumference
Q_x, Q_y	Betatron (bare) tunes
$w(s)$	Envelope at zero space charge
$\beta(s)$	Beta function
$\alpha(s)$	Alpha function
$\gamma(s)$	Gamma function
$\mu(s)$	Betatron phase advance
$D(s)$	Dispersion function
ϵ_x, ϵ_y, ϵ_z	Horizontal, vertical, and longitudinal emittances
ξ_x, ξ_y	Normalized chromaticities
V	RF voltage
Q_s	Synchrotron tune
η	Slip factor
h	Harmonic number
F_n	$\frac{n}{2}$ half-integer stop-band integral at zero intensity
σ_x, σ_y	RMS Transverse beam sizes
σ_z	RMS bunch length
$\sigma_{\Delta p/p}$	RMS momentum spread
Y	normalized vertical envelope $\frac{\sigma_y}{\sqrt{\epsilon_y\, \beta_y}}$
λ	Charge density
ϵ_0	Vacuum permittivity
K_{sc}	Space charge perveance
I	Peak current
m_0	Particle mass
ΔQ_{KV}	Space-charge KV tune shift
ΔQ_{env}	Space-charge envelope tune shift
$\Delta Q_{\mathrm{Gauss}}$	Space-charge tune spread in a Gaussian-like beam
$\frac{1}{\epsilon}\frac{\mathrm{d}\epsilon}{\mathrm{d}n}$	Emittance-growth rate
a_{ϵ_x}, a_{ϵ_y}, a_{ϵ_z}	Scaling factors of emittances
f_1, f_2, f_3	Objective functions

List of Figures

List of Tables

Bibliography

[1] M. L. Oliphant, J. S. Gooden, and G. S. Hide. “The acceleration of charged particles to very high energies”. In: *Proceedings of the Physical Society* 59.4 (July 1947), pp. 666–677. doi: 10.1088/0959-5309/59/4/314 (cit. on p. 1).

[2] V. I. Veksler. “A new method of acceleration of relativistic particles”. In: *J. Phys.* 9 (1945), pp. 153–158 (cit. on p. 1).

[3] E. M. McMillan. “The Synchrotron — A Proposed High Energy Particle Accelerator”. In: *Phys. Rev.* 68 (5-6 Sept. 1945), pp. 143–144. doi: 10.1103/PhysRev.68.143 (cit. on p. 1).

[4] J. E. Augustin et al. “Discovery of a Narrow Resonance in e^+e^- Annihilation”. In: *Phys. Rev. Lett.* 33 (23 Dec. 1974), pp. 1406–1408. doi: 10.1103/PhysRevLett.33.1406 (cit. on p. 1).

[5] J. J. Aubert et al. “Experimental Observation of a Heavy Particle J”. In: *Phys. Rev. Lett.* 33 (23 Dec. 1974), pp. 1404–1406. doi: 10.1103/PhysRevLett.33.1404 (cit. on p. 1).

[6] G. Pancheri and C. Rubbia. “Events of very high energy density at the CERN SppS collider”. In: *Nuclear Physics A* 418 (1984), pp. 117–138. doi: 10.1016/0375-9474(84)90546-3 (cit. on p. 1).

[7] B. Cork, L. Kerth, W. A. Wenzel, J. W. Cronin, and R. L. Cool. “Decay Asymmetry of Σ^+ and Λ^0 Hyperons”. In: *Phys. Rev.* 120 (3 Nov. 1960), pp. 1000–1004. doi: 10.1103/PhysRev.120.1000 (cit. on p. 1).

[8] G. Danby, J.-M. Gaillard, K. Goulianos, L. M. Lederman, N. Mistry, M. Schwartz, and J. Steinberger. “Observation of High-Energy Neutrino Reactions and the Existence of Two Kinds of Neutrinos”. In: *Phys. Rev. Lett.* 9 (1 July 1962), pp. 36–44. doi: 10.1103/PhysRevLett.9.36 (cit. on p. 1).

[9] M. Benedikt, P. Collier, V. Mertens, J. Poole, and K. Schindl. *LHC Design Report*. CERN Yellow Reports: Monographs. Geneva: CERN, 2004. doi: 10.5170/CERN-2004-003-V-3 (cit. on p. 1).

[10] G. Aad et al. “A Particle Consistent with the Higgs Boson Observed with the ATLAS Detector at the Large Hadron Collider”. In: *Science* 338.6114 (Dec. 2012), pp. 1576–1582. doi: 10.1126/science.1232005 (cit. on p. 1).

[11] D. Abbaneo et al. “A New Boson with a Mass of 125 GeV Observed with the CMS Experiment at the Large Hadron Collider”. In: *Science* 338.6114 (Dec. 2012), pp. 1569–1575. doi: 10.1126/science.1230816 (cit. on p. 1).

[12] A. W. Chao and W. Chou. “Editorial Preface”. In: *Reviews of Accelerator Science and Technology* 04.01 (Jan. 2011), pp. v–vi. doi: 10.1142/s1793626811000628 (cit. on p. 1).

[13] K. Blasche, B. Franczak, B. Langenbeck, G. Moritz, and C. Riedel. “The heavy ion synchrotron SIS-a progress report”. In: *Proceedings of International Conference on Particle Accelerators*. 1993, 3736–3738 vol.5. doi: 10.1109/PAC.1993.309772 (cit. on pp. 1, 5, 77).

[14] P. Spiller et al. “Status of the FAIR Project”. In: *Proc. 9th International Particle Accelerator Conference* (Vancouver, BC, Canada). June 2018, pp. 63–68. doi: doi:10.18429/JACoW-IPAC2018-MOZGBF2 (cit. on pp. 1, 5, 77).

[15] P. Spiller et al. “The FAIR Heavy Ion Synchrotron SIS100”. In: *Journal of Instrumentation* 15.12 (Dec. 2020), T12013–T12013. doi: 10.1088/1748-0221/15/12/t12013 (cit. on pp. 1, 5).

[16] *GSI Helmholtzzentrum für Schwerionenforschung*. https://www.gsi.de/start/aktuelles. Accessed: 31/08/2022 (cit. on p. 2).

[17] N. Christofilos. *Focusing system for ions and electrons*. U.S. Patent US2736799A, Feb. 28, 1956 (cit. on p. 1).

[18] J. P. Blewett. “Radial Focusing in the Linear Accelerator”. In: *Phys. Rev.* 88 (5 Dec. 1952), pp. 1197–1199. doi: 10.1103/PhysRev.88.1197 (cit. on p. 1).

[19] E. D. Courant, M. S. Livingston, and H. S. Snyder. “The Strong-Focusing Synchroton — A New High Energy Accelerator”. In: *Phys. Rev.* 88 (5 Dec. 1952), pp. 1190–1196. doi: 10.1103/PhysRev.88.1190 (cit. on pp. 1, 10).

[20] J. B. Adams. “The Cern Proton Synchrotron”. In: *Nature* 185.4713 (Feb. 1960), pp. 568–572. doi: 10.1038/185568a0 (cit. on p. 3).

[21] J.-P. Burnet et al. *Fifty years of the CERN Proton Synchrotron: Volume 1*. CERN Yellow Reports: Monographs. Geneva: CERN, 2011. doi: 10.5170/CERN-2011-004 (cit. on p. 3).

[22] R. A. Beth and C. Lasky. “The Brookhaven Alternating Gradient Synchrotron”. In: *Science* 128.3336 (1958), pp. 1393–1401. doi: 10.1126/science.128.3336.1393 (cit. on p. 3).

[23] G. Lüders. *On the influence of irregularities of magnetic field on betatron oscillations in an alternating-gradient synchrotron*. CERN Yellow Reports: Monographs. Translated from the original German paper published in Nuovo Cimento Suppl. 2 (1955) pp. 1075-1146. Geneva: CERN, 1956. doi: 10.5170/CERN-1956-008 (cit. on p. 4).

[24] A. Schoch. *Theory of linear and non-linear perturbations of betatron oscillations in alternating-gradient synchrotrons*. CERN Yellow Reports: Monographs. Geneva: CERN, 1958. doi: 10.5170/CERN-1957-021 (cit. on p. 4).

[25] H. Wiedemann. *Particle Accelerator Physics*. Springer International Publishing, 2015. doi: 10.1007/978-3-319-18317-6 (cit. on pp. 4, 9, 20).

[26] E. Métral et al. "Beam Instabilities in Hadron Synchrotrons". In: *IEEE Transactions on Nuclear Science* 63.2 (2016), pp. 1001–1050. doi: 10.1109/TNS.2015.2513752 (cit. on p. 4).

[27] K. Y. Ng. *Physics of Intensity Dependent Beam Instabilities*. World Scientific, 2005. doi: 10.1142/5835 (cit. on p. 4).

[28] A. W. Chao. *Physics of collective beam instabilities in high-energy accelerators*. Wiley, 1993 (cit. on p. 4).

[29] R. A. Kishek, M. Reiser, P. O'Shea, M. Venturini, and W. W. Zhang. "Errors, Resonances, and Corrections in the Space-Charge Beam of the University of Maryland Electron Ring (UMER)". In: *The Physics of High Brightness Beams*. World Scientific, Dec. 2000. doi: 10.1142/9789812792181_0018 (cit. on p. 4).

[30] I. Hofmann. *Space Charge Physics for Particle Accelerators*. Springer International Publishing, 2017. doi: 10.1007/978-3-319-62157-9 (cit. on pp. 4, 25, 35).

[31] W. Fischer et al. "Vacuum pressure rise with intense ion beams in RHIC". In: *Proceedings of the European Particle Accelerator Conference EPAC*. Jan. 2002 (cit. on p. 4).

[32] A. Oeftiger, O. Boine-Frankenheim, V. Chetvertkova, V. Kornilov, D. Rabusov, and S. Sorge. "Simulation study of the space charge limit in heavy-ion synchrotrons". In: *Phys. Rev. Accel. Beams* 25 (5 May 2022), p. 054402. doi: 10.1103/PhysRevAccelBeams.25.054402 (cit. on pp. 4, 6, 20, 36, 61).

[33] P. Spiller and G. Franchetti. "The FAIR accelerator project at GSI". In: *Nuclear Instruments and Methods in Physics Research Section A: Accelerators, Spectrometers, Detectors and Associated Equipment* 561.2 (2006). Proceedings of the Workshop on High Intensity Beam Dynamics, pp. 305–309. doi: 10.1016/j.nima.2006.01.043 (cit. on p. 4).

[34] *Facility for Antiproton and Ion Research in Europe GmbH*. https://fair-center.eu/overview/research. Accessed: 21/08/2022 (cit. on p. 5).

[35] A. Herlert. "NUSTAR – The teenage years". In: *Hyperfine Interactions* 238.1 (Feb. 2017). doi: 10.1007/s10751-017-1411-0 (cit. on p. 5).

[36] P. Senger. "Probing dense QCD matter in the laboratory—The CBM experiment at FAIR". In: *Physica Scripta* 95.7 (May 2020), p. 074003. doi: 10.1088/1402-4896/ab8c14 (cit. on p. 5).

[37] P. Senger. "Astrophysics in the Laboratory — The CBM Experiment at FAIR". In: *Particles* 3.2 (Apr. 2020), pp. 320–335. doi: 10.3390/particles3020024 (cit. on p. 5).

[38] A. Belias. "FAIR status and the PANDA experiment". In: *Journal of Instrumentation* 15.10 (Oct. 2020), pp. C10001–C10001. doi: 10.1088/1748-0221/15/10/c10001 (cit. on p. 5).

[39] T. Stöhlker et al. "SPARC: The Stored Particle Atomic Research Collaboration At FAIR". In: *AIP Conference Proceedings*. AIP, 2011. doi: 10.1063/1.3586073 (cit. on p. 5).

[40] T. Stöhlker et al. "APPA at FAIR: From fundamental to applied research". In: *Nuclear Instruments and Methods in Physics Research Section B: Beam Interactions with Materials and Atoms* 365 (Dec. 2015), pp. 680–685. doi: 10.1016/j.nimb.2015.07.077 (cit. on p. 5).

[41] O. Bohne. "Status Report on the UNILAC". In: *IEEE Transactions on Nuclear Science* 24.3 (1977), pp. 1070–1075. doi: 10.1109/TNS.1977.4328853 (cit. on p. 5).

[42] W. Barth, W. Bayer, L. Dahl, L. Groening, S. Richter, and S. Yaramyshev. "Upgrade program of the high current heavy ion UNILAC as an injector for FAIR". In: *Nuclear Instruments and Methods in Physics Research Section A: Accelerators, Spectrometers, Detectors and Associated Equipment* 577.1 (2007). Proceedings of the 16th International Symposium on Heavy Ion Inertial Fusion, pp. 211–214. doi: 10.1016/j.nima.2007.02.054 (cit. on p. 5).

[43] O. Boine-Frankenheim. "The FAIR Accelerators: Highlights and Challenges". In: *Conf. Proc. C* 100523 (2010). Ed. by A. Noda, C. Petit-Jean-Genaz, V. R. W. Schaa, T. Shirai, and A. Shirakawa, WEYRA01 (cit. on p. 5).

[44] E. Courant and H. Snyder. "Theory of the alternating-gradient synchrotron". In: *Annals of Physics* 3.1 (1958), pp. 1–48. doi: 10.1016/0003-4916(58)90012-5 (cit. on pp. 6, 10, 20).

[45] I. M. Kapchinsky and V. V. Vladimirsky. “Limitations Of Proton Beam Current In A Strong Focusing Linear Accelerator Associated With The Beam Space Charge”. In: *2nd International Conference on High-Energy Accelerators*. 1959, pp. 274–287 (cit. on pp. 6, 27, 29).

[46] D. C. Morin Jr. “Transverse space charge effects in particle accelerators”. Ph.D. Thesis. University of Wisconsin, Aug. 1962 (cit. on p. 6).

[47] P. Lapostolle. “Oscillations in a synchrotron under space charge conditions”. In: *4th International Conference on High-Energy Accelerators*. Vol. 2. 1964, pp. 1235–1239 (cit. on pp. 6, 46, 93).

[48] S. Lloyd. “Effect of gradient errors in the presence of space charge forces”. In: *3rd International Conference on High-Energy Accelerators*. 1963, pp. 1232–1234 (cit. on p. 6).

[49] F. J. Sacherer. “Transverse space charge effects in circular accelerators”. Presented 30 Oct 1968. Ph.D. Thesis. University of California, Berkeley, Oct. 1968. doi: 10.2172/877342 (cit. on pp. 6, 25, 28, 30, 31, 35, 45, 46, 63, 93).

[50] F. J. Sacherer. “RMS Envelope Equations with Space Charge”. In: *IEEE Transactions on Nuclear Science* 18.3 (1971), pp. 1105–1107. doi: 10.1109/TNS.1971.4326293 (cit. on pp. 6, 35).

[51] R. Baartman. “Betatron resonances with space charge”. In: *AIP Conf. Proc.* 448.1 (1998). Ed. by A. U. Luccio and W. T. Weng, pp. 56–72. doi: 10.1063/1.56781 (cit. on pp. 6, 29, 38, 57, 59).

[52] R. Cappi, R. Garoby, S. Hancock, M. Martini, and J. Riunaud. “Measurement and reduction of transverse emittance blow-up induced by space charge effects”. In: *Proceedings of International Conference on Particle Accelerators*. 1993, 3570–3572 vol.5. doi: 10.1109/PAC.1993.309720 (cit. on p. 7).

[53] D. Neuffer, D. Fitzgerald, T. Hardek, R. Hutson, R. Macek, M. Plum, H. Thiessen, and T.-S. Wang. “Observation of space-charge effects in the Los Alamos Proton Storage Ring”. In: *Conference Record of the 1991 IEEE Particle Accelerator Conference*. IEEE. doi: 10.1109/pac.1991.164813 (cit. on p. 7).

[54] C. M. Warsop, D. J. Adams, B. Jones, B. G. Pine, H. V. Smith, and R. E. Williamson. “Simulation and Measurement of Half Integer Resonance in Coasting Beams on the ISIS Ring”. In: *Conf. Proc. C* 110904 (2011). Ed. by C. Petit-Jean-Genaz, pp. 637–639 (cit. on p. 7).

[55] T. Uesugi, S. Machida, and Y. Mori. “Experimental study of a half-integer resonance with space-charge effects in a synchrotron”. In: *Phys. Rev. ST Accel. Beams* 5 (4 Apr. 2002), p. 044201. doi: 10.1103/PhysRevSTAB.5.044201 (cit. on p. 7).

[56] G. Franchetti et al. “Experiment on space charge driven nonlinear resonance crossing in an ion synchrotron”. In: *Phys. Rev. ST Accel. Beams* 13 (11 Nov. 2010), p. 114203. doi: 10.1103/PhysRevSTAB.13.114203 (cit. on p. 7).

[57] I. Hofmann and K. Beckert. “Resonance crossing in the presence of space charge”. In: *IEEE Trans. Nucl. Sci.* 32 (1985). Ed. by A. Strathdee, pp. 2264–2266. doi: 10.1109/TNS.1985.4333880 (cit. on p. 7).

[58] M. D’yachkov, R. Baartman, and F. Jones. “Multiturn simulation of coherent betatron resonance with space charge”. In: *PACS2001. Proceedings of the 2001 Particle Accelerator Conference (Cat. No.01CH37268)*. Vol. 1. 2001, 267–269 vol.1. doi: 10.1109/PAC.2001.987489 (cit. on p. 7).

[59] S. Machida. “Space-charge effects in low-energy proton synchrotrons”. In: *Nuclear Instruments and Methods in Physics Research Section A: Accelerators, Spectrometers, Detectors and Associated Equipment* 309.1 (1991), pp. 43–59. doi: 10.1016/0168-9002(91)90091-4 (cit. on p. 7).

[60] S. Machida. “Space-charge-induced resonances in a synchrotron”. In: *Nuclear Instruments and Methods in Physics Research Section A: Accelerators, Spectrometers, Detectors and Associated Equipment* 384.2-3 (1997), pp. 316–321. doi: 10.1016/S0168-9002(96)00884-4 (cit. on p. 7).

[61] C. Warsop, D. Adams, B. Jones, and B. Pine. “Simple Models for Beam Loss Near the Half Integer Resonance with Space Charge”. In: *57th ICFA Advanced Beam Dynamics Workshop on High-Intensity and High-Brightness Hadron Beams*. 2016, MOPR030. doi: 10.18429/JACoW-HB2016-MOPR030 (cit. on p. 7).

[62] S. Cousineau, S. Y. Lee, J. A. Holmes, V. Danilov, and A. Fedotov. “Space charge induced resonance excitation in high intensity rings”. In: *Phys. Rev. ST Accel. Beams* 6 (3 Mar. 2003), p. 034205. doi: 10.1103/PhysRevSTAB.6.034205 (cit. on pp. 7, 35).

[63] A. V. Fedotov and I. Hofmann. “Half-integer resonance crossing in high-intensity rings”. In: *Phys. Rev. ST Accel. Beams* 5 (2 Feb. 2002), p. 024202. doi: 10.1103/PhysRevSTAB.5.024202 (cit. on pp. 7, 45, 57, 59).

[64] H.-C. Chao and S. Y. Lee. “Simulations of beam envelope dynamics in circular accelerators”. In: *Phys. Rev. ST Accel. Beams* 18 (2 Feb. 2015), p. 024202. doi: 10.1103/PhysRevSTAB.18.024202 (cit. on p. 7).

[65] J. Qiang. “Three-dimensional envelope instability in periodic focusing channels”. In: *Phys. Rev. Accel. Beams* 21 (3 Mar. 2018), p. 034201. doi: 10.1103/PhysRevAccelBeams.21.034201 (cit. on p. 7).

[66] I. Hofmann, A. Oeftiger, and O. Boine-Frankenheim. “Self-consistent long-term dynamics of space charge driven resonances in 2D and 3D”. In: *Phys. Rev. Accel. Beams* 24 (2 Feb. 2021), p. 024201. doi: 10.1103/PhysRevAccelBeams.24.024201 (cit. on p. 7).

[67] S. Y. Lee. *Accelerator Physics*. World Scientific, Mar. 2011. doi: 10.1142/8335 (cit. on pp. 9, 13, 17, 37).

[68] D. A. Edwards and M. J. Syphers. *An Introduction to the Physics of High Energy Accelerators*. Wiley, Jan. 1993. doi: 10.1002/9783527617272 (cit. on p. 9).

[69] K. Wille. *Physik der Teilchenbeschleuniger und Synchrotronstrahlungsquellen*. Vieweg+Teubner Verlag, 1996. doi: 10.1007/978-3-663-11039-2 (cit. on p. 9).

[70] H. Bruck. *Accélérateurs circulaires de particules: introduction à la théorie*. Presses Universitaires, Paris, 1966 (cit. on p. 9).

[71] H. Okamoto and S. Machida. “Particle beam resonances driven by dispersion and space charge”. In: *Nuclear Instruments and Methods in Physics Research Section A: Accelerators, Spectrometers, Detectors and Associated Equipment* 482.1 (2002), pp. 65–78. doi: 10.1016/S0168-9002(01)01685-0 (cit. on p. 22).

[72] O. D. Kellogg. *Foundations of potential theory*. Vol. 31. Courier Corporation, 1953 (cit. on p. 27).

[73] *High-level programming language Python*. https://www.python.org/. Accessed: 01/09/2022 (cit. on p. 31).

[74] O. Boine-Frankenheim and W. Stem. “Space charge compensation with pulsed electron lenses for intense ion beams in synchrotrons”. In: *Nuclear Instruments and Methods in Physics Research Section A: Accelerators, Spectrometers, Detectors and Associated Equipment* 896 (2018), pp. 122–128. doi: 10.1016/j.nima.2018.04.014 (cit. on p. 31).

[75] A. Khan, O. Boine-Frankenheim, F. Hug, and C. Stoll. “Beam matching with space charge in energy recovery linacs”. In: *Nuclear Instruments and Methods in Physics Research Section A: Accelerators, Spectrometers, Detectors and Associated Equipment* 948 (2019), p. 162822. doi: 10.1016/j.nima.2019.162822 (cit. on p. 31).

[76] Y. S. Yuan, O. Boine-Frankenheim, G. Franchetti, and I. Hofmann. “Dispersion-Induced Beam Instability in Circular Accelerators”. In: *Phys. Rev. Lett.* 118 (15 Apr. 2017), p. 154801. doi: 10.1103/PhysRevLett.118.154801 (cit. on p. 31).

[77] D. Rabusov, A. Oeftiger, and O. Boine-Frankenheim. “Characterization and minimization of the half-integer stop band with space charge in a hadron synchrotron”. In: *Nuclear Instruments and Methods in Physics Research Section A: Accelerators, Spectrometers, Detectors and Associated Equipment* 1040 (2022), p. 167290. doi: 10.1016/j.nima.2022.167290 (cit. on pp. 35, 61).

[78] *Virgo computer claster at GSI*. https://hpc.gsi.de/virgo/preface.html. Accessed: 01/09/2022 (cit. on p. 35).

[79] M. Schwinzerl, R. De Maria, K. Paraschou, H. Bartosik, G. Iadarola, and A. Oeftiger. “Optimising and Extending a Single-particle Tracking Library for High Parallel Performance”. In: *Proceedings of the 12th International Particle Accelerator Conference*. CERN-ACC-NOTE-2021-0023. 2021, THPAB190. doi: 10.18429/JACoW-IPAC2021-THPAB190 (cit. on p. 36).

[80] *Methodical accelerator design*. https://mad.web.cern.ch/mad/. Accessed: 29/06/2022 (cit. on pp. 36, 42).

[81] *Overview of elegant and SDDS*. https://ops.aps.anl.gov/elegant.html. Accessed: 05/09/2022 (cit. on p. 36).

[82] *Strategic Accelerator Design*. https://acc-physics.kek.jp/SAD/. Accessed: 05/09/2022 (cit. on p. 36).

[83] A. Oeftiger. *An Overview of PyHEADTAIL*. Tech. rep. CERN-ACC-NOTE-2019-0013. Geneva: CERN, Apr. 2019 (cit. on p. 36).

[84] R. Hockney and J. Eastwood. *Computer Simulation Using Particles*. CRC Press, Mar. 2021. doi: 10.1201/9780367806934 (cit. on p. 36).

[85] *PyORBIT-Collaboration*. https://github.com/PyORBIT-Collaboration. Accessed: 05/09/2022 (cit. on p. 36).

[86] *TraceWin*. https://dacm-logiciels.fr/tracewin. Accessed: 05/09/2022 (cit. on p. 36).

[87] J. Qiang, M. A. Furman, and R. D. Ryne. “A parallel particle-in-cell model for beam-beam interaction in high energy ring colliders”. In: *Journal of Computational Physics* 198.1 (July 2004), pp. 278–294. doi: 10.1016/j.jcp.2004.01.008 (cit. on p. 38).

[88] M. Bassetti and G. A. Erskine. *Closed expression for the electrical field of a two-dimensional Gaussian charge*. Tech. rep. Geneva: CERN, 1980 (cit. on p. 38).

[89] J. Laskar. “The chaotic motion of the solar system: A numerical estimate of the size of the chaotic zones”. In: *Icarus* 88.2 (1990), pp. 266–291. doi: 10.1016/0019-1035(90)90084-M (cit. on p. 41).

[90] B. W. S. L. Montague. *Fourth-order coupling resonance excited by space-charge forces in a synchrotron*. Tech. rep. CERN-1968-038. Geneva: CERN, 1968. doi: 10.5170/CERN-1968-038 (cit. on p. 59).

[91] D. Ondreka. *(private communication)*. 2020 (cit. on p. 61).

[92] M. J. D. Powell. "A Direct Search Optimization Method That Models the Objective and Constraint Functions by Linear Interpolation". In: *Advances in Optimization and Numerical Analysis*. Springer Netherlands, 1994, pp. 51–67. doi: 10.1007/978-94-015-8330-5_4 (cit. on p. 63).

[93] P. Forck, A. Bank, T. Giacomini, and A. Peters. "Profile Monitors based on residual gas interaction". In: *7th European Workshop on Beam Diagnostics and Instrumentation for Particle Accelerators, DIPAC 2005* (Jan. 2005), pp. 223–227 (cit. on p. 82).

[94] T. Giacomini. *(private communication)*. 2021 (cit. on p. 84).

[95] R. Singh. "Tune Measurement at GSI SIS-18: Methods and Applications". en. Ph.D. Thesis. Darmstadt: Technische Universität, 2014 (cit. on p. 87).

[96] I. Karpov, V. Kornilov, and O. Boine-Frankenheim. "Early transverse decoherence of bunches with space charge". In: *Phys. Rev. Accel. Beams* 19 (12 Dec. 2016), p. 124201. doi: 10.1103/PhysRevAccelBeams.19.124201 (cit. on p. 88).

[97] R. Bartolini, A. Bazzani, M. Giovannozzi, W. Scandale, and E. Todesco. "Tune evaluation in simulations and experiments". In: *Part. Accel.* 52 (1996), 147–177. 29 p (cit. on p. 88).

Acknowledgements

First, I would like to express my sincere gratitude to Prof. Dr. Oliver Boine-Frankenheim for offering me the opportunity to contribute to research. Second, I would like to thank Prof. Dr. Shaukat Khan for agreeing to be my second referent and for the valuable discussions during our HGS-HIRe meetings. Third, I would like to express my deep appreciation to Dr. Adrian Oeftiger for supervising me at GSI. It would not be possible to complete this work without his assistance and constructive feedback. During the last few years, I have had numerous fruitful discussions with him that have greatly advanced my skills and inspired me.

I am grateful to Dr. Adrian Oeftiger, Dr. David Ondreka, and Dr. Holger Liebermann for their help with the preparation for the SIS18 experiment as well as for valuable discussions. I wish to thank Dr. Rahul Singh and Tino Giacomini for their support in BPM and IPM measurements in SIS18. Also, this experiment could not be possible without the assistance of Conrad Caliari, Dr. Thilo Egenolf, and Vadim Gubaidulin.

I am indebted to Vadim Gubaidulin, Dr. Dhevan Gangadharan, Dr. Uwe Niedermayer, Dr. Stefan Sorge, Aleksandr Tusnin, Ella Barakhovskaia, and Andrei Rabusov who voluntarily proofread this manuscript and provided valuable feedback and helpful comments.

I am thankful to my TEMF and GSI colleges for the nice working environment. Dr. Sabrina Appel and Dr. Adrian Oeftiger encouraged me to use GSI high-performance computing (Kronos cluster and then Virgo cluster), and I greatly benefited from this. I would like to thank Dr. Wolfgang Müller and Dragos Munteanu for their help with technical and organizational questions.

My stay in Darmstadt was filled with deep, joyful, and supportive friendships. I would like to thank the “Schnelle Ionen” sports club, football and volleyball teams in particular for the competitive and cheerful atmosphere. The support of my friends across the world via the Internet helped me to survive during the COVID lockdowns.

It would not have been possible for me to embark on this journey without the support of my family. My elder brother, Andrei Rabusov, inspired me to become a researcher, while the wisdom of my mother, Margarita Rabusova, helped me to always be on the right path in my life.

Publication List

Journal Articles

- **Dmitrii Rabusov**, Adrian Oeftiger, and Oliver Boine-Frankenheim, *Characterization and minimization of the half-integer stop band with space charge in a hadron synchrotron*, Nuclear Instruments and Methods in Physics Research Section A: Accelerators, Spectrometers, Detectors and Associated Equipment, vol. 1040, p. 167290 (2022).

- Adrian Oeftiger, Oliver Boine-Frankenheim, Vera Chetvertkova, Vladimir Kornilov, **Dmitrii Rabusov**, Stefan Sorge, *Simulation Study of the Space Charge Limit in Heavy-ion Synchrotrons*, Phys. Rev. Accel. Beams, vol. 25, p. 054402 (2022).

Conference Contributions

- *Automated optimization of synchrotrons for high-intensity beams*, Oral presentation at Workshop “Advances in Electromagnetic Research - KWT 2019”, Riezlern, Austria (2019)